Universität Hamburg
DER FORSCHUNG | DER LEHRE | DER BILDUNG

An Ultrashort Pulsed Light Source in the VUV

—

Tunable in the Vicinity of 133 nm

Dissertation

zur Erlangung des Doktorgrades
an der Fakultät für Mathematik, Informatik und Naturwissenschaften
Fachbereich Physik
der Universität Hamburg

vorgelegt von

Nora Klara Anna Schmitt

Hamburg

2024

Gutachter der Dissertation:	Prof. Dr. Markus Drescher Prof. Dr. Henning Moritz
Zusammensetzung der Prüfungskommission:	Prof. Dr. Markus Drescher Prof. Dr. Henning Moritz Prof. Dr. Daniela Pfannkuche Prof. Dr. Markus Ilchen Prof. Dr. Tais Gorkhover
Vorsitzende der Prüfungskommission:	Prof. Dr. Daniela Pfannkuche
Datum der Disputation:	16.12.2024
Vorsitzender des Fach-Promotionsausschusses Physik:	Prof. Dr. Wolfgang J. Parak
Leiter des Fachbereichs Physik:	Prof. Dr. Markus Drescher
Dekan der Fakultät für Mathematik, Informatik und Naturwissenschaften:	Prof. Dr.-Ing. Norbert Ritter

Abstract

Powerful ultrashort laser pulses in the vacuum ultraviolet (VUV) spectral range are of great interest for investigating ultrafast dynamics in atomic and molecular systems, such as in pump-probe studies of photoionization and photodissociation. To freely select arbitrary electronic transitions, achieving wavelength tunability is highly desirable but challenging to attain.

In this thesis, an ultrashort pulsed light source with a central wavelength of 133 nm is realized, employing a step-wise manipulation scheme of ultrashort laser pulses generated by a titanium-sapphire laser system. The second harmonic, centered around 400 nm, serves as the fundamental for third-harmonic generation (THG) in a pulsed gas cell. By utilizing xenon as the nonlinear medium, VUV pulse energies of up to 1.5 µJ are achieved, with a THG conversion efficiency of 1.7×10^{-3}.

A significant advancement toward a wavelength-tunable source is attained through a proof of concept for tunability in the VUV range. The technique is based on the variation of the fundamental wavelength in the Fourier plane of a 4f geometry, which is also used for pulse compression. By shifting the wavelength of the UV radiation over a range of 10 nm, a wavelength shift of 2.8 nm is observed in the resulting VUV light.

Zusammenfassung

Leistungsstarke ultrakurze Laserpulse im vakuumultravioletten Spektralbereich (VUV) sind von großer Bedeutung für die Untersuchung ultraschneller Prozesse in atomaren und molekularen Systemen, beispielsweise bei Pump-Probe Untersuchungen von Photoionisation und Photodissoziation. Um beliebige elektronische Übergänge frei wählen zu können, ist eine Durchstimmbarkeit der Wellenlänge wünschenswert, was allerdings schwierig umzusetzen ist.

In dieser Arbeit wird eine ultrakurz gepulste Lichtquelle mit einer zentralen Wellenlänge von 133 nm realisiert. Dazu wird ein schrittweises Manipulationsschema verwendet, welches auf ultrakurzen Laserpulsen basiert, die von einem Titan:Saphir-Lasersystem erzeugt werden. Die zweite Harmonische mit einer Zentralwellenlänge von 400 nm dient als Fundamentale für Frequenzverdreifachung in einer gepulsten Gaszelle. Unter Verwendung von Xenon als nichtlineares Medium werden Pulsenergien im VUV von bis zu $1,5$ µJ erreicht. Die Konversionseffizienz der Frequenzverdreifachung beträgt dabei $1,7 \times 10^{-3}$.

Ein wesentlicher Fortschritt auf dem Weg zu einer durchstimmbaren Quelle wird durch erfolgreiche Wellenlängenverschiebung im VUV erreicht. Die Methode basiert auf der Anpassung der fundamentalen Wellenlänge in der Fourierebene einer 4f-Geometrie, welche darüber hinaus auch zur Pulskompression verwendet wird. Bei einer Verschiebung der Wellenlänge der fundamentalen UV-Strahlung um 10 nm wird eine Wellenlängenverschiebung des resultierenden VUV-Lichts um $2,8$ nm beobachtet.

Declaration on Oath

Eidesstattliche Versicherung

Hiermit versichere ich an Eides statt, die vorliegende Dissertationsschrift selbst verfasst und keine anderen als die angegebenen Hilfsmittel und Quellen benutzt zu haben. Sofern im Zuge der Erstellung der vorliegenden Dissertationsschrift generative Künstliche Intelligenz (gKI) basierte elektronische Hilfsmittel verwendet wurden, versichere ich, dass meine eigene Leistung im Vordergrund stand und dass eine vollständige Dokumentation aller verwendeten Hilfsmittel gemäß der Guten wissenschaftlichen Praxis vorliegt. Ich trage die Verantwortung für eventuell durch die gKI generierte fehlerhafte oder verzerrte Inhalte, fehlerhafte Referenzen, Verstöße gegen das Datenschutz- und Urheberrecht oder Plagiate.

Hamburg, den 23.10.2024

Nora Schmitt

KI basierte elektronische Hilfsmittel (OpenAI, GPT-3.5 und GPT-4o) wurden zur Grammatik- und Rechtschreibprüfung sowie Paraphrasierung verwendet, ohne dabei neue Inhalte zu generieren.

Contents

1. Introduction

The vacuum ultraviolet (VUV) spectral region, covering wavelengths between 100 and 200 nm, holds exceptional significance in spectroscopy, as nearly all materials and chemical compounds exhibit strong electronic absorption resonances within this range. Consequently, VUV photons are particularly valuable for investigating electronically excited atoms and molecules, enabling photoionization and photodissociation through single-photon processes. To perform time-resolved measurements that explore the dynamics of excited systems, the generation of ultrashort pulses is essential.

To access the VUV, various types of sources are available, each offering distinct advantages for specific applications. Excimer lasers, for instance, are commonly employed in the production of microelectronic devices, semiconductor-based integrated circuits, and micromachining due to their ability to deliver high pulse energies. However, they are constrained by long pulses and low repetition rates [1].
Another approach that enables short pulses in the VUV is frequency conversion of short laser pulses through nonlinear optical processes. For frequency conversion in solid nonlinear media, conventional nonlinear crystals like beta barium borate (BBO) or lithium triborate (LBO) are unsuitable due to their strong absorption. An exception is potassium beryllium fluoroborate (KBBF), which can reach down to approximately 150 nm [2]. For wavelengths down to 177 nm, a pulse duration of 55 fs is attainable [3]. While this is relatively short, it is not short enough to resolve the dynamics of the majority of relevant photochemical processes. Furthermore, KBBF crystals are challenging to grow and not readily available [4]. An additional solid-state based method is frequency conversion utilizing dielectric nanomembranes [5] or surfaces [6, 7], although they are limited in peak power due to the material damage threshold.
In gas, frequency conversion can be achieved via four-wave mixing [8] or harmonic generation [9–11], enabling the production of short pulses down to the attosecond range [12]. In hollow core capillary fibers (HCFs), in addition to four-wave mixing [13] and (cascaded) harmonic generation [14], the creation of resonant dispersive waves (RDWs) [15] is a viable method.

Beyond laboratory tabletop sources, synchrotrons [16] and free electron lasers (FELs) [17] offer continuously tunable radiation with extremely high brightness. However, they are limited in terms of pulse duration, coherence properties [18] and accessibility.

The most widely used source for time-resolved VUV spectroscopy is harmonic generation in gas, with a prominent example being the fifth harmonic of a titanium-sapphire (Ti:Sa) laser, centered around 160 nm. In an argon gas cell, high-energy pulses with 1.1 µJ pulse energy and less than 20 fs pulse duration have been generated [19]. These pulses have been utilized to study the dynamics of atomic and molecular systems [20–24]. However, the number of accessible transitions is limited by the fixed photon energy of 7.75 eV.

In this thesis, an alternative VUV generation scheme is explored to expand the accessible range of photon energies. The second harmonic of a Ti:Sa laser system serves as the fundamental to generate pulses centered around 133 nm through frequency-tripling in a gas cell. This approach promises high conversion efficiencies, as third-harmonic generation (THG) is primarily governed by the bound-electron third-order susceptibility. Additionally, shorter driving wavelengths have been shown to enhance harmonic generation in the multiphoton regime [25]. Sapaev et al. predict a conversion efficiency of 1.5×10^{-3} in argon [26]. Another benefit of a 400 nm fundamental wavelength is the relatively large separation of 6.2 eV between the generated harmonics, which simplifies spectral selection.

There is only a limited number of experimental works utilizing the same generation scheme based on THG of 400 nm radiation in gas for ultrashort pulses. Trabs et al. report a conversion efficiency in the order of 10^{-4} in argon [27, 28], though the beam profile suggests that six-wave mixing, rather than THG, may be the underlying process in their work. Zhou et al. estimate their VUV pulse energy to be a remarkable value of 6.4 µJ, resulting in a conversion efficiency of 1.4×10^{-3} in an argon gas jet [29]. Notably, Svoboda et al. have demonstrated the generation of ultrashort circularly polarized VUV pulses in a xenon gas jet through low-order harmonic generation driven by 400 nm pulses [30].

To precisely address and freely select arbitrary electronic transitions, thereby gaining a deeper insight into the dynamics of excited atomic and molecular systems, a powerful and tunable ultrashort pulsed light source for spectroscopy in the VUV is needed. In this thesis, a significant step toward this objective is taken by demonstrating tunability in the VUV through adjustment of the fundamental wavelength in the Fourier plane of a 4f geometry that is additionally used for pulse compression.

To elucidate the fundamental principles underlying the experiments, Chapter 2 introduces the theoretical background of ultrashort laser pulses and their nonlinear interactions with matter. Chapter 3 provides a detailed description of the individual components comprising the experimental setup, while Chapter 4 focuses on numerical simulations of the manipulation of ultrashort laser pulses at various stages of the setup. Subsequently, Chapter 5 analyzes the ultraviolet (UV) pulses centered around 400 nm, which serve as the fundamental for THG, and Chapter 6 examines the characteristics of the generated VUV pulses. Chapter 7 concludes with a summary of findings, few ideas for future optimization of the setup, and an outlook on possible systems to study in time-resolved experiments using the generated VUV radiation.

2. Theoretical background

In order to establish a theoretical foundation of the underlying physical mechanisms in this work, the following chapter will focus on the description of ultrashort laser pulses in time, frequency and space and their nonlinear interactions with matter. Second-order effects such as second-harmonic generation (SHG) and third-order effects such as self-phase modulation (SPM) and THG are discussed, since they enable the creation of new frequencies from 800 nm in the near-infrared (NIR) down to the VUV spectral region.
Subsequently, the transport of light in a gas filled hollow core capillary fiber will be elucidated, laying the groundwork for numerical simulations of the propagation in Chapter 4.
Additionally, different autocorrelation techniques will be considered and a powerful tool for pulse characterization will be introduced - the fringe-resolved interferometric autocorrelation (FRIAC). This method combines quantities related to both field and intensity autocorrelation, providing an estimate of pulse duration as well as details about the phase of the pulse.

2.1. Ultrashort laser pulses

Laser pulses can be described as electromagnetic wave packets and therefore be fully characterized by their time and space dependent electric field $\boldsymbol{\mathcal{E}}(\mathbf{r},t)$ or magnetic field $\boldsymbol{\mathcal{H}}(\mathbf{r},t)$ that are coupled by Maxwell's equations. These quantities are three-dimensional real valued vector fields depending on space $\mathbf{r}$ and time t. The discussion in this chapter follows [31] and [32].

For convenience, the utilization of the complex representation of the electric field $\mathbf{E}(\mathbf{r},t)$ is common practice. In the following, the spatial and polarization dependence are omitted for better readability, reducing the relation between the real and complex electric field to

$$\mathcal{E}(t) = \Re\left(E(t)\right) = \frac{1}{2}E(t) + c.c., \tag{2.1}$$

where *c.c.* denotes the complex conjugate. Depending on the specific effect described, a representation in frequency domain $\tilde{E}(\omega)$ - linked to time domain by Fourier transform - is sometimes preferable, defined as

$$\tilde{E}(\omega) = \int_{-\infty}^{\infty} E(t) e^{-i\omega t} dt, \qquad E(t) = \frac{1}{2\pi} \int_{-\infty}^{\infty} \tilde{E}(\omega) e^{i\omega t} d\omega. \tag{2.2}$$

2.1.1. Spectral phase and dispersion

The field is commonly expressed by the product of an amplitude $A(t)$, also referred to as envelope term, and a phase term $e^{i\Phi(t)}$. Together with the carrier frequency ω_0 representing the central frequency of the pulse, this results in

$$E(t) = A(t) \cdot e^{i\Phi(t)} = A(t) \cdot e^{i(\phi(t) - \omega_0 t)}, \tag{2.3}$$

where $\phi(t)$ denotes the temporal phase of the pulse. Along the same lines, the spectral amplitude $\tilde{A}(\omega)$ and spectral phase $\varphi(\omega)$ are defined by

$$\tilde{E}(\omega) = \tilde{A}(\omega) \cdot e^{i\varphi(\omega)}. \tag{2.4}$$

To evaluate the phases, $\varphi(\omega)$ and $\phi(t)$ are commonly expanded into Taylor series around the central frequency ω_0 or the reference time t_0. In the frequency domain, this yields

$$\begin{aligned} \varphi(\omega) &= \sum_{n=0}^{\infty} \frac{1}{n!} \frac{\partial^n \varphi(\omega)}{\partial \omega^n}\bigg|_{\omega=\omega_0} (\omega - \omega_0)^n \\ &= \varphi_0 + \varphi_1(\omega - \omega_0) + \frac{\varphi_2}{2}(\omega - \omega_0)^2 + \frac{\varphi_3}{6}(\omega - \omega_0)^3 + \frac{\varphi_4}{24}(\omega - \omega_0)^4 + ..., \end{aligned} \tag{2.5}$$

where φ_0 is the absolute phase between carrier and envelope of the electric field of the pulse, φ_1 is the group delay, φ_2 is the group delay dispersion (GDD), and φ_3 and φ_4 are the third-order dispersion (TOD) and fourth-order dispersion (FOD), respectively.

The impact of the carrier-envelope phase (CEP) φ_0 becomes pronounced mainly for few-cycle pulses, since in this situation the observed electric field is notably influenced by the relative phase between carrier wave and envelope. The group delay represents the arrival time of the pulse with respect to the reference time t_0. The GDD is correlated with a linear chirp, i.e. frequency dependent arrival time of different spectral components. Moreover, a chirp leads to temporal broadening of the pulse. Analogous to the GDD, the TOD is related to a cubic dependence of the phase and results in an asymmetric pulse shape with satellite pulses in time at the trailing or leading edge of the pulse depending on its sign. Leading and trailing wings in time are an indication for FOD components in the spectral phase. An illustration of the impact of all these terms on a short pulse can be found in Figure 2.1. While the Taylor expansion could of course be further continued, the terms up to the fourth order are sufficient to describe the effects discussed in this work.

For completeness, a similar Taylor expansion of the phase may be done in the time domain, written as

$$\begin{aligned}\phi(t) &= \sum_{n=0}^{\infty} \frac{1}{n!} \frac{\partial^n \phi(t)}{\partial t^n}\bigg|_{t=t_0} (t-t_0)^n \\ &= \phi_0 + \phi_1(t-t_0) + \frac{\phi_2}{2}(t-t_0)^2 + \frac{\phi_3}{6}(t-t_0)^3 + \frac{\phi_4}{24}(t-t_0)^4 + ...,\end{aligned} \tag{2.6}$$

where the quantities ϕ_0 - ϕ_4 correspond to analogous terms φ_0 - φ_4 in the Fourier domain (see Equation (2.5)) - for instance the first order term ϕ_1 corresponds to an overall shift in frequency and so forth.

Time-bandwidth product

Obtaining the shortest possible pulse with temporal width $\Delta\tau$ for a given spectral width $\Delta\nu = \Delta\omega/2\pi$ and a given amplitude $\tilde{A}(\omega)$ requires the phase to be flat and all higher-order (≥ 2) phase terms to vanish. When these conditions are fulfilled, a pulse is referred to as transform-limited (see Figure 2.1 (a)-(c)).

To quantify the deviation of a specific pulse shape from the theoretical minimum given by the uncertainty principle, the time-bandwidth product (TBP) is of interest. The TBP is defined as

$$\Delta\nu\Delta\tau = \text{TBP} \geq \text{K}. \tag{2.7}$$

The theoretical minimum K varies with pulse shape and definition of the width. For a Gaussian pulse and full width at half maximum (FWHM) of the intensity, the minimum is $\text{K} = 0.441$, whereas for a sech^2 shaped pulse the limit is given by $\text{K} = 0.315$.

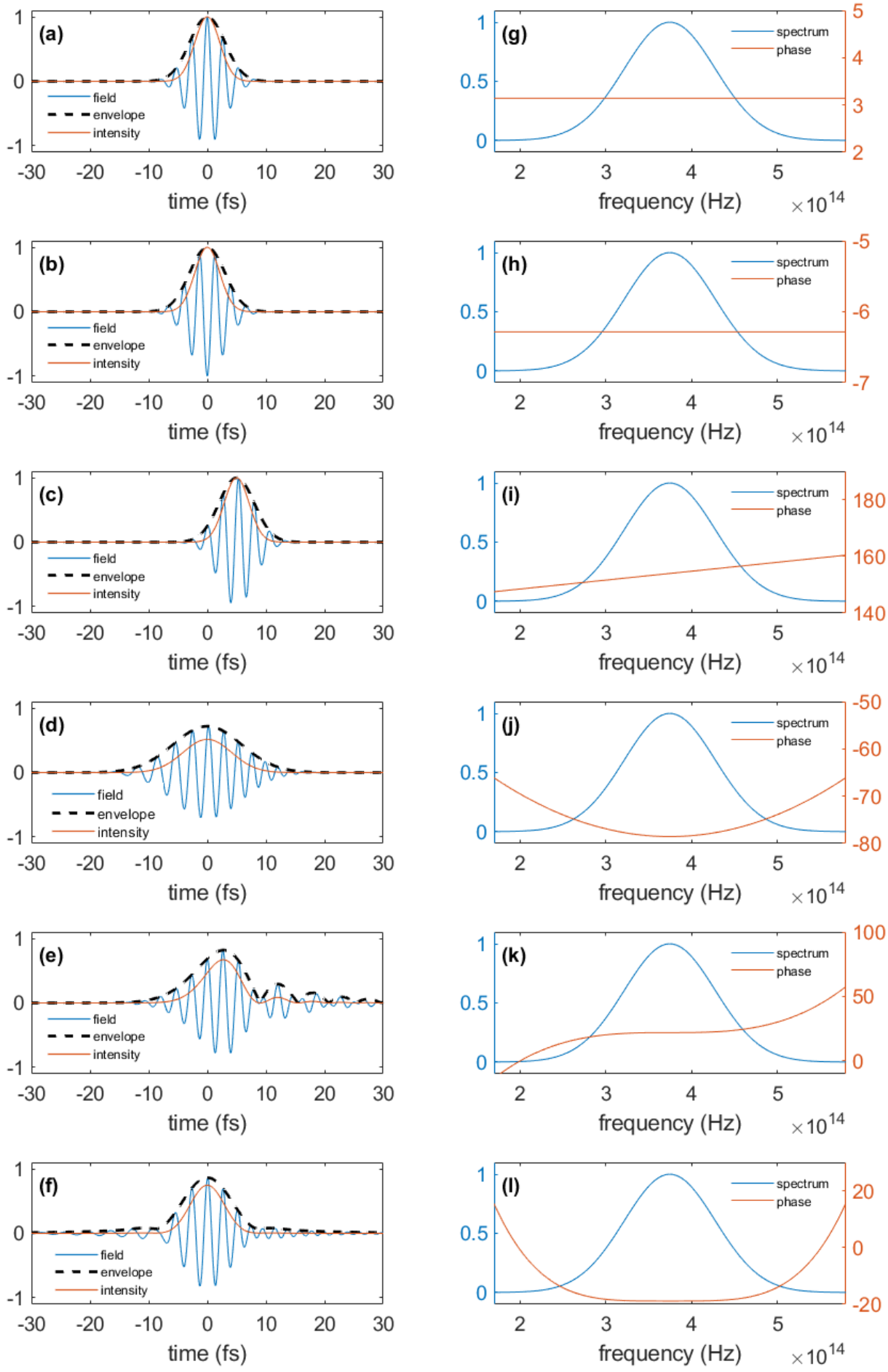
(a)
field
envelope
intensity
time (fs)
(g)
spectrum
phase
frequency (Hz)
×10^14
(b)
(h)
(c)
(i)
(d)
(j)
(e)
(k)
(f)
(l)

Figure 2.1.: The impact of the spectral phase. (a-f): Oscillating electric field, electric field envelope and intensity of short pulses centered at 800 nm as a function of time (normalized to unity). (g-l): Corresponding spectra (normalized) and phases (in radians) in frequency space. The the central frequency is given by $\nu_0 = \omega_0/2\pi = 3.75 \times 10^{14}$ Hz.

(a/g) Transform-limited Gaussian with $\varphi = 0$ and intensity FWHM of 5 fs. The phase is flat.

(b/h) Pulse from (a) with an additional CEP of π, still transform-limited - only the relative phase between carrier and envelope is shifted. The phase is flat with an offset.

(c/i) Pulse from (a) with an additional group delay of 5 fs, also still transform-limited - the pulse is only shifted in time. The phase is linear with respect to the frequency ν.

(d/j) Pulse from (a) with an additional GDD of 15 fs^2, not transform-limited any more - the pulse is longer and exhibits a linear chirp. The phase is quadratic with respect to ν.

(e/k) Pulse from (a) with an additional TOD of 100 fs^3, the pulse is longer and the shape is asymmetric. The phase is proportional to $(\nu - \nu_0)^3$.

(f/l) Pulse from (a) with an additional FOD of 300 fs^4, the pulse is longer with symmetric wings to both sides. The phase is proportional to $(\nu - \nu_0)^4$.

The spectra remain unchanged for all cases.

2.1.2. Gaussian beam propagation

Beyond the temporal and spectral characteristics, also the spatial propagation of laser beams is of interest for this work. In many instances it may be adequately described by the model of a simple Gaussian beam that we will discuss here. In one part of the setup, the light is confined by an HCF - the propagation characteristics of this fiber are a bit more complex and will be explained later in this chapter.

The electric field $E(r,z)$ of a Gaussian beam is a solution to the paraxial Helmholtz equation. Since radial symmetry is assumed, a cylindrical coordinate system is chosen. For simplicity, the temporal dependence is omitted - but it may always be added by multiplication with a Gaussian pulse in time. The equation for the electric field reads

$$E(r,z) = E_0 \, \frac{w_0}{w(z)} \, e^{\frac{-r^2}{w(z)^2}} \, e^{-i\left(kz + k\frac{r^2}{2R(z)} - \psi(z)\right)}, \tag{2.8}$$

where r is the radial coordinate, z is the axial distance from the beam waist, $E_0 = E(0,0)$ is the electric field amplitude at the origin, w_0 is the waist radius at $z = 0$ (where the intensity drops to $1/e^2$ of the maximum), $w(z)$ is the beam waist for a given z-position, $R(z)$ is the radius of curvature of the wavefronts, k is the wave number and $\psi(z)$ is the Gouy phase.

Some of these terms are commonly expressed using the Rayleigh range z_R, the central wavelength λ_0 and refractive index of the medium n. The Rayleigh range defines the distance z in propagation direction where the area of the cross section of the beam has doubled. The expressions for the Rayleigh range, beam waist, Gouy phase, and radius of curvature are given by

$$\begin{aligned} z_R &= \frac{\pi w_0^2 n}{\lambda_0}, & w(z) &= w_0 \sqrt{1 + \left(\frac{z}{z_R}\right)^2}, \\ \psi(z) &= \arctan\left(\frac{z}{z_R}\right), & R(z) &= z\left(1 + \left(\frac{z_R}{z}\right)^2\right). \end{aligned} \tag{2.9}$$

For the corresponding intensity distribution $I(r,z)$, the relation simplifies to

$$I(r,z) = \frac{|E(r,z)|^2}{2\eta} = I_0 \, \left(\frac{w_0}{w(z)}\right)^2 \, e^{\frac{-2r^2}{w(z)^2}}, \tag{2.10}$$

where $\eta = \sqrt{\mu/\epsilon}$ is the wave impedance of the medium, defined by the magnetic permeability μ and electric permittivity ϵ. $I_0 = |E_0|^2/2\eta$ denotes the intensity in the center of the beam at the waist. In Figure 2.2, the intensity distribution of an exemplary beam is depicted together with the corresponding Rayleigh range and beam waist.

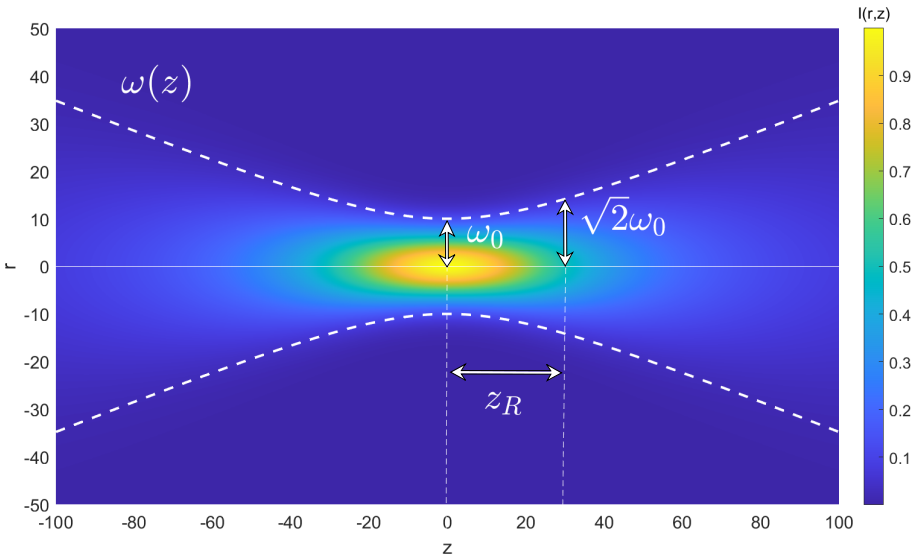

Figure 2.2.: Normalized intensity distribution of a Gaussian beam with Rayleigh range $z_R = 30$ and beam waist $w_0 = 10$. The z-dependent waist is indicated by dashed white lines.

Beam quality factor M^2

In the description above, the beam is assumed to exhibit a perfect Gaussian shape. To describe deviations from this assumption, the parameter M^2 is commonly used [33]. It is also known as the beam quality factor and represents the degree of variation from an ideal Gaussian beam. For a single mode perfect Gaussian, M^2 is exactly one.

To determine M^2, the $D4\sigma$ width W is measured at multiple positions z, some close to the beam waist and others further away than the Rayleigh range. σ denotes the standard deviation of the intensity distribution. For an ideal Gaussian beam, the $D4\sigma$ width and $1/e^2$ diameter measurements ($= 2w$) yield the same result but the $D4\sigma$ definition is more robust with respect to noise, since it relies on integrated quantities rather than single values at specific points. The widths and positions can be fitted to

$$W^2(z) = W_0^2 + M^4 \left(\frac{\lambda}{\pi W_0}\right)^2 (z - z_0)^2, \tag{2.11}$$

where λ denotes the wavelength and W_0 the beam width at the central position z_0.

2.2. Nonlinear interactions with matter

A general approach to the description of the interaction of an electromagnetic field with matter is using Maxwell's macroscopic equations in their differential form. This chapter follows [34] for most of the argumentation. A similar discussion can be found in various textbooks, e.g. [35]. Maxwell's equation read

$$\begin{aligned} \nabla \cdot \boldsymbol{\mathcal{D}} &= \rho, & \nabla \cdot \boldsymbol{\mathcal{B}} &= 0, \\ \nabla \times \boldsymbol{\mathcal{E}} &= -\frac{\partial}{\partial t}\boldsymbol{\mathcal{B}}, & \nabla \times \boldsymbol{\mathcal{H}} &= \boldsymbol{\mathcal{J}} + \frac{\partial}{\partial t}\boldsymbol{\mathcal{D}}, \end{aligned} \tag{2.12}$$

where $\boldsymbol{\mathcal{D}}$ denotes the electric displacement field, ρ the electric charge density, $\boldsymbol{\mathcal{B}}$ the magnetic flux density (sometimes referred to as magnetic induction or also as magnetic field), $\boldsymbol{\mathcal{E}}$ the electric and $\boldsymbol{\mathcal{H}}$ the magnetic field and $\boldsymbol{\mathcal{J}}$ the electric current density. The relations between $\boldsymbol{\mathcal{D}}$, $\boldsymbol{\mathcal{E}}$, $\boldsymbol{\mathcal{B}}$ and $\boldsymbol{\mathcal{H}}$ are given by

$$\boldsymbol{\mathcal{D}} = \epsilon_0 \boldsymbol{\mathcal{E}} + \boldsymbol{\mathcal{P}}, \tag{2.13}$$

$$\boldsymbol{\mathcal{H}} = \frac{1}{\mu_0}\boldsymbol{\mathcal{B}} - \boldsymbol{\mathcal{M}}, \tag{2.14}$$

where ϵ_0 is the vacuum permittivity, $\boldsymbol{\mathcal{P}}$ the polarization density of the material, μ_0 the vacuum permeability and $\boldsymbol{\mathcal{M}}$ the magnetization.

In the special case of linear, homogeneous, isotropic, dielectric media with instantaneous response to changes in the electric field, $\boldsymbol{\mathcal{P}}$ shows a linear dependence on the electric field, written as

$$\boldsymbol{\mathcal{P}} = \epsilon_0 \chi \boldsymbol{\mathcal{E}}, \tag{2.15}$$

where the constant of proportionality is called electric susceptibility χ. In general, $\chi = \chi(\omega)$ and $\boldsymbol{\mathcal{E}} = \boldsymbol{\mathcal{E}}(\omega)$ change with the frequency of the light ω, leading to a frequency dependent polarization $\boldsymbol{\mathcal{P}}(\omega)$. Combining Equations (2.13) and (2.15) and defining the permittivity $\epsilon = \epsilon_0(1+\chi)$ leads to the commonly used relation for linear media, which reads

$$\boldsymbol{\mathcal{D}} = \epsilon_0(1+\chi)\boldsymbol{\mathcal{E}} = \epsilon \boldsymbol{\mathcal{E}}. \tag{2.16}$$

In a more general scenario of a nonlinear dielectric medium, $\boldsymbol{\mathcal{P}} = \boldsymbol{\mathcal{P}}(\boldsymbol{\mathcal{E}})$ can be expressed as a nonlinear function of $\boldsymbol{\mathcal{E}}$. Since there are no free currents or charges, we set $\rho = 0$ as well as $\boldsymbol{\mathcal{J}} = 0$. Additionally we assume a non-magnetic medium, thus $\boldsymbol{\mathcal{M}} = 0$.

Taking the curl of $\nabla \times \boldsymbol{\mathcal{E}}$, using the vector identity $\nabla \times (\nabla \times \boldsymbol{\mathcal{E}}) = \nabla(\nabla \cdot \boldsymbol{\mathcal{E}}) - \nabla^2 \boldsymbol{\mathcal{E}}$ and combining this with Maxwell's equations (Equation (2.12)), one obtains the wave equation

$$\nabla^2 \boldsymbol{\mathcal{E}} - \mu_0 \epsilon_0 \frac{\partial^2}{\partial t^2} \boldsymbol{\mathcal{E}} = \mu_0 \frac{\partial^2}{\partial t^2} \boldsymbol{\mathcal{P}}. \tag{2.17}$$

Assuming a well-behaved polarization $\boldsymbol{\mathcal{P}}(\boldsymbol{\mathcal{E}})$, we express it in a Taylor series (Einstein summation convention)

$$\mathcal{P}_i = \epsilon_0 (\chi^{(1)}_{ij} \mathcal{E}_j + \chi^{(2)}_{ijk} \mathcal{E}_j \mathcal{E}_k + \chi^{(3)}_{ijkl} \mathcal{E}_j \mathcal{E}_k \mathcal{E}_l + ...). \tag{2.18}$$

The susceptibilities $\boldsymbol{\chi}^{(x)}$ are in general tensors of the order $(x+1)$, but their number of independent components strongly depends on the material's symmetries - usually most of the components vanish. For example the linear susceptibility $\boldsymbol{\chi}^{(1)}$ corresponds to the simple χ in Equation (2.15) for the condition of isotropic media. Only for anisotropic media, when birefringence comes into play, the multi-dimensional nature of $\boldsymbol{\chi}^{(1)}$ is of interest. All linear effects that do not depend on the intensity of the light are described by the first term of the Taylor series. The linear index of refraction is given by

$$n = \sqrt{1 + \chi^{(1)}}. \tag{2.19}$$

In general, interaction of light with matter is dominated by the linear term, as the susceptibilities $\boldsymbol{\chi}^{(x)}$ are becoming smaller with larger x. Only for high values of the electric field, which are in the order of magnitude of the inner-molecular or inner-atomic fields, the nonlinear components cannot be neglected any more.

Separating the linear and nonlinear part of the polarization $\boldsymbol{\mathcal{P}} = \epsilon_0 \chi \boldsymbol{\mathcal{E}} + \boldsymbol{\mathcal{P}}_{\boldsymbol{\mathcal{NL}}}$ and using the vacuum speed of light $c_0 = 1/\sqrt{\mu_0 \epsilon_0}$, Equation (2.17) yields

$$\nabla^2 \boldsymbol{\mathcal{E}} - \frac{n^2}{c_0^2} \frac{\partial^2}{\partial t^2} \boldsymbol{\mathcal{E}} = \mu_0 \frac{\partial^2}{\partial t^2} \boldsymbol{\mathcal{P}}_{\boldsymbol{\mathcal{NL}}}, \tag{2.20}$$

where only $\boldsymbol{\chi}^{(x)}$ with $x \geq 2$ are influencing the source term on the right side of the differential equation.

2.2.1. Second-order nonlinear processes

Second-order nonlinear interactions - such as SHG - can only occur in non-centrosymmetric media, since the second order susceptibility $\boldsymbol{\chi}^{(2)}$ vanishes in case of inversion symmetry. As gases, liquids, amorphous solids and even many crystals display inversion symmetry, the choice of materials for second-order processes is rather limited. Crystals lacking inversion symmetry, such as BBO, LBO, and potassium titanyl phosphate (KTP), are typically used for $\boldsymbol{\chi}^{(2)}$ nonlinear frequency conversion. Moreover, the breaking of symmetry caused by an interface is sometimes exploited to drive second-order processes at surfaces [36].

Omitting the vector nature of the fields for better readability, the nonlinear polarization for second-order processes can simply be written as

$$\mathcal{P}^{(2)} = \epsilon_0 \chi^{(2)} \mathcal{E}^2. \tag{2.21}$$

Considering an electric field with two frequency components ω_1 and ω_2 and amplitudes E_1 and E_2, which is defined by

$$\mathcal{E} = \frac{1}{2}(E_1 e^{-i\omega_1 t} + E_2 e^{-i\omega_2 t}) + c.c., \tag{2.22}$$

the nonlinear polarization reads

$$\begin{aligned}
\mathcal{P}^{(2)} =& \frac{\epsilon_0 \chi^{(2)}}{4} \left(E_1 e^{-i\omega_1 t} + E_2 e^{-i\omega_2 t} + E_1^* e^{i\omega_1 t} + E_2^* e^{i\omega_2 t}\right)^2 \\
=& \frac{\epsilon_0 \chi^{(2)}}{4} (2E_1 E_1^* + 2E_2 E_2^* \\
&+ E_1^2 e^{-i2\omega_1 t} + E_2^2 e^{-i2\omega_2 t} + E_1^{*2} e^{i2\omega_1 t} + E_2^{*2} e^{i2\omega_2 t} \\
&+ 2E_1 E_2 e^{-i(\omega_1+\omega_2)t} + 2E_1^* E_2^* e^{i(\omega_1+\omega_2)t} \\
&+ 2E_1 E_2^* e^{-i(\omega_1-\omega_2)t} + 2E_1^* E_2 e^{i(\omega_1-\omega_2)t}).
\end{aligned} \tag{2.23}$$

The non-oscillating terms in the first line of Equation (2.23) lead to a process known as optical rectification, creating a static electric field. The other terms give rise to frequency conversion. They are oscillating with new frequency components that are sums of the frequency components of the original electric field. The terms oscillating with $2\omega_1$ and $2\omega_2$ in the second line correspond to SHG, the terms oscillating with $(\omega_1 + \omega_2)$ in the third line describe sum frequency generation (SFG) and the terms oscillating with $(\omega_1 - \omega_2)$ result in difference frequency generation (DFG).

In a particle picture, SHG, SFG and DFG are three-photon processes, where the interaction between the photons is mediated by virtual states in the nonlinear medium. An illustration of the processes with corresponding energy-levels is shown in Figure 2.3. Since energy is conserved, one photon with ω_1 and one photon with ω_2 is needed to create one photon with $(\omega_1 + \omega_2)$ in case of SFG. In this picture, SHG is a special case of SFG with $(\omega_1 = \omega_2)$. For DFG, two photons are created from one photon at the first frequency of the original field ω_1 - one at the difference frequency $\omega_1 - \omega_2$ and one at the second frequency of the original field ω_2.

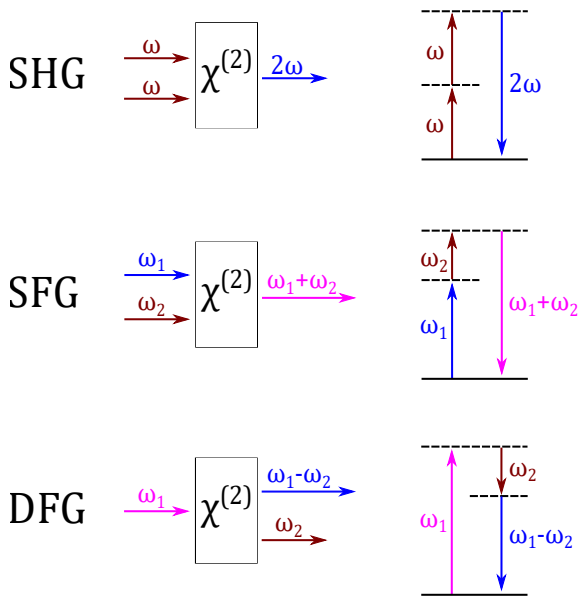

Figure 2.3.: Illustration of the second-order nonlinear processes SHG, SFG and DFG on the left and energy-level scheme on the right. Adapted from [34].

Phase-matching conditions

The description above neglects the vector nature of the electric fields. To drive any of those processes efficiently, the phase-matching condition $\Delta\mathbf{k} = 0$ for the wave vectors $\mathbf{k}$ needs to be satisfied. In the particle picture, this corresponds to momentum conservation. For SFG and SHG ($\omega_3 = \omega_1 + \omega_2$) one obtains the following condition:

$$0 = \Delta\mathbf{k} = \mathbf{k}_1 + \mathbf{k}_2 - \mathbf{k}_3. \tag{2.24}$$

In a collinear geometry, the relation reduces to

$$0 = k_1 + k_2 - k_3 = \frac{1}{c_0}\left(n(\omega_1)\omega_1 + n(\omega_2)\omega_2 - n(\omega_3)\omega_3\right). \tag{2.25}$$

In general, the linear refractive index n depends on the frequencies of the light. In the special case of SHG, where $\omega = \omega_1 = \omega_2$ and $\omega_3 = 2\omega$, one obtains

$$0 = 2n(\omega)\omega - n(2\omega)2\omega \qquad \Rightarrow \qquad n(\omega) = n(2\omega). \tag{2.26}$$

Since the refractive index usually increases monotonically with the frequency, this relation cannot be satisfied for most materials. A common method to achieve a scenario, where Equation (2.26) can be fulfilled, is through the use of birefringent crystals, where n depends on the polarization of the light. Fortunately, birefringence occurs naturally in the non-inversion symmetric crystals, which are commonly used for second-order nonlinear frequency conversion.

To obtain phase-matching in birefringent crystals, there are two possibilities. For type I phase-matching, two photons with ordinary polarization are converted to one photon with extraordinary polarization. For type II phase-matching, two photons with orthogonal polarization are converted to one photon with ordinary polarization.

In this thesis, a thin BBO is used for SHG with type I phase-matching to convert the short laser pulses centered around 800 nm in the NIR to 400 nm in the UV.

2.2.2. Third-order nonlinear processes

Third-order nonlinear processes do not require the absence of inversion symmetry and therefore can be observed in various media when the electric field strength of the light field is strong enough. Similar to the second-order nonlinear polarization, the third-order polarization can be written as

$$\mathcal{P}^{(3)} = \epsilon_0 \chi^{(3)} \mathcal{E}^3. \tag{2.27}$$

For a general case, where the input field $\mathcal{E}$ is composed of different frequencies, the expression for $\mathcal{P}$ becomes rather long and complicated, describing all kinds of 4-wave-mixing processes. Thus, we will focus on a simple monochromatic input field, given by $\mathcal{E} = \frac{1}{2}(Ee^{-i\omega t} + c.c.)$. The third-order polarization in this case reads

$$\begin{aligned} \mathcal{P}^{(3)} =& \frac{\epsilon_0 \chi^{(3)}}{6} \left(Ee^{-i\omega t} + E^* e^{i\omega t}\right)^3 \\ =& \frac{\epsilon_0 \chi^{(3)}}{6} (E^3 e^{-i3\omega t} + E^{*3} e^{i3\omega t} \\ &+ 3\left|E\right|^2 Ee^{-i\omega t} + 3\left|E\right|^2 E^* e^{i\omega t}). \end{aligned} \tag{2.28}$$

Third-harmonic generation

The first part in Equation (2.28) describes a nonlinear response at 3ω. This corresponds to THG that is a four-photon process in the particle picture, where three photons with the fundamental frequency ω are converted to one photon with the frequency 3ω. A schematic depiction of THG can be found in Figure 2.4. In this work, the third-harmonic of short 400 nm pulses is generated via THG in gas, which creates photons at 133 nm in the VUV spectral range.

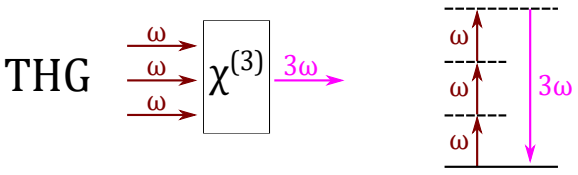

Figure 2.4.: Illustration of third-harmonic generation on the left and energy-level scheme on the right. Adapted from [34].

Optical Kerr effect

The second part in Equation (2.28) gives rise to a nonlinear polarization at the frequency of the incident light, which depends on the absolute value squared of the electric field amplitude and thus on the intensity I of the light field, since $I \propto |E|^2$.

As a consequence, this effect may be described as an intensity dependent refractive index

$$n = n_0 + n_2 I, \tag{2.29}$$

where n_0 denotes the linear refractive index and $n_2 = 3\chi^{(3)}/4n_0^2\epsilon_0 c$ the nonlinear refractive index. This phenomenon is referred to as optical Kerr effect.

A spatial process that is caused by an intensity dependent refractive index is **self-focusing**. When a high-intensity beam of light that is more intense in the center of the beam profile (e.g. Gaussian) travels through a medium where $n_2 > 0$, the material acts like a converging lens, since the refractive index in the center of the beam is higher than in the surrounding area.

Another mechanism caused by the optical Kerr effect - but now in the temporal domain - is **self-steepening**. When a laser pulse travels through a nonlinear medium, the intensity is highest at the peak, which increases the refractive index and causes the peak to travel slightly slower than the rest of the pulse. This leads to a steepening of its trailing edge.

An additional process, which is caused by the intensity dependent refractive index, is **self-phase modulation (SPM)**. Here, the frequency domain is affected. When a short light pulse travels through a medium, it induces a variation of the refractive index in time, resulting in a phase shift that leads to the creation of new frequency components. We consider the exemplary case of a simple Gaussian pulse with the temporal intensity distribution

$$I(t) = I_0 \, e^{-4\ln(2)\left(\frac{t}{\tau}\right)^2}, \tag{2.30}$$

where I_0 is the peak intensity and τ the FWHM pulse duration. Together with Equation (2.29), the time dependent refractive index is given by

$$n(t) = n_0 + n_2 \, I_0 \, e^{-4\ln(2)\left(\frac{t}{\tau}\right)^2}. \tag{2.31}$$

The instantaneous phase of the pulse $\Phi(t)$ (see Equation (2.3)) can be written as

$$\Phi(t) = \omega_0 t - kz = \omega_0 t - \frac{2\pi}{\lambda_0} n(t) z, \tag{2.32}$$

with the central frequency ω_0, wave number k, propagation distance z and central wavelength λ_0. Since the instantaneous frequency ω is given by the temporal derivative of the phase, one obtains

$$\omega(t) = \frac{d}{dt}\Phi(t) = \omega_0 - \frac{2\pi}{\lambda_0} z \frac{d}{dt} n(t) = \omega_0 + \frac{16\ln(2)\pi z n_2 I_0}{\lambda_0 \tau^2}\, t\, e^{-4\ln(2)\left(\frac{t}{\tau}\right)^2}. \tag{2.33}$$

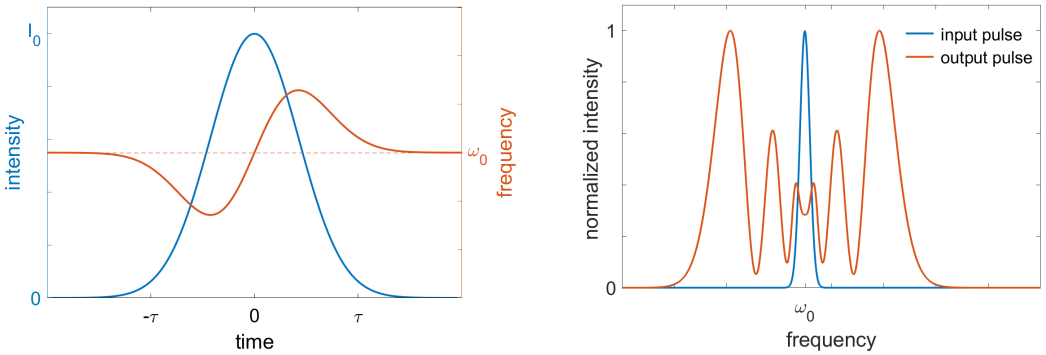

Figure 2.5.: Effect of SPM on a Gaussian pulse in time in a waveguide. Left: temporal intensity profile of the pulse (blue) together with the instantaneous frequency (red). Right: spectrum of an initially Fourier-limited Gaussian pulse before and after traveling through a fiber where SPM occurs.

A qualitative depiction of the instantaneous frequency for a Gaussian pulse in a waveguide is given in Figure 2.5 on the left. In case of an initially transform-limited pulse or a pulse with a positive chirp, SPM leads to spectral broadening, which is depicted in Figure 2.5 on the right. The data was retrieved by a numerical simulation that is described in Chapter 4.1.1.

Spectral broadening induced by SPM is commonly used in hollow core fiber compressors to achieve the necessary spectral bandwidth to further compress already short laser pulses. In this work, SPM in a stretched hollow core fiber filled with noble gas (helium) is used to create a broad spectrum around 400 nm.

2.3. Propagation of light in a capillary waveguide

Hollow core capillary waveguides are widely used in nonlinear and ultrafast optics for various applications, e.g. four-wave mixing [37], high-harmonic generation [38], nonlinear spectral broadening [39], and soliton generation [15]. As mentioned above, a stretched HCF is used in this work to spectrally broaden ultrashort laser pulses through SPM.

2.3.1. Fiber modes

To understand the guiding mechanism, we consider a cylindrical waveguide with a hollow core of radius a surrounded by dielectric material - in our case fused silica - with complex refractive index n. Opposed to standard optical fibers, the refractive index of the core (usually filled with a noble gas) is smaller than that of the cladding, leading to a weaker guiding mechanism and more propagation losses, since total internal reflection is not possible. The subsequent argumentation follows [40] and [39].

If the radius a is much larger than the wavelength λ of the propagating light, one can safely assume the free space propagation constant $k = 2\pi/\lambda$ to fulfill

$$ka = \frac{2\pi a}{\lambda} \gg |n| u_{nm}, \tag{2.34}$$

where u_{nm} is the m-th zero of the Bessel function J_{n-1}. In our case, the wavelength is 400 nm and the inner radius 250 µm, which satisfies the condition in Equation (2.34).

Solving the wave equation in cylindrical coordinates and neglecting terms with powers of λ/a larger than one, one finds three different kinds of supported modes: transverse electric (TE) circular modes, transverse magnetic (TM) circular modes, and hybrid modes (EH or HE), which can be analyzed as a superposition of TE and TM components. When the TE components dominate, the convention is to name the mode hybrid electromagnetic (EH) and when the TM components dominate, they are usually referred to as hybrid electromagnetic (HE). In [40], all possible modes are discussed in detail.

For a ratio of outer and inner refractive index $\nu = n_{cladding}/n_{core}$ of more than 2.02, the mode with lowest attenuation is TE_{01}. For $\nu < 2.02$, which is the case for most combinations of glass and gas, EH_{11} - a hybrid mode - leads to the lowest attenuation constant. Consequently, this mode is preferred when propagating light in hollow core capillary fibers.

The radial intensity profiles of hybrid modes EH_{nm} are given by

$$I_{nm}(r) = I_0 J_{n-1}^2 \left(\frac{u_{n,m} r}{a} \right), \tag{2.35}$$

where the wave oscillates like $e^{\gamma z - \omega t}$, where γ is the (complex) propagation constant, z the propagation distance, ω the frequency and t the time.

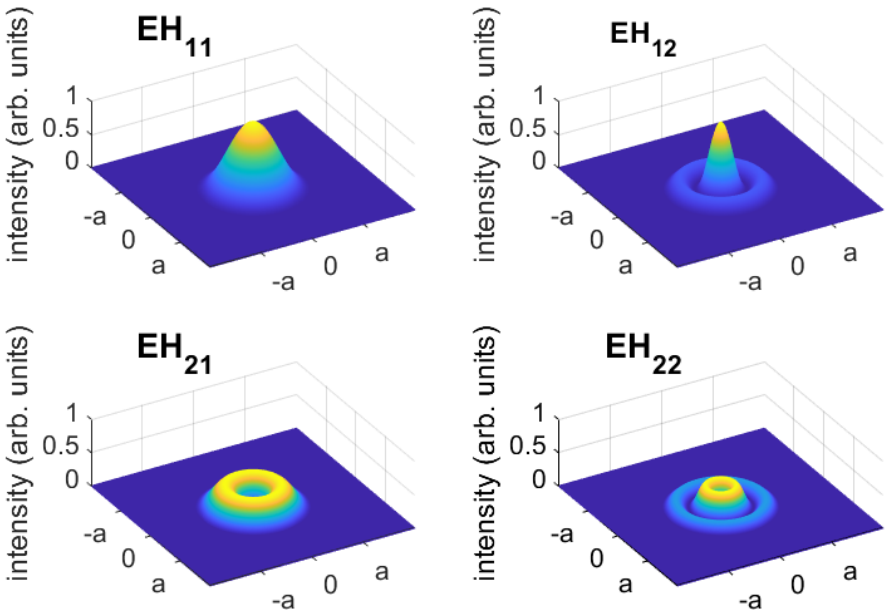

Figure 2.6.: Intensity profile of the hybrid modes EH_{nm} for n and m up to two inside the waveguide, where $r < a$. For $r = a$, they go to zero, where they remain for $r > a$.

In Figure 2.6, the shape of the intensity profile of the first few modes is shown. For $n > 1$, the distribution exhibits a minimum at the center of the waveguide.

The real part (α, attenuation constant) and imaginary part (β, phase constant) of the propagation constant $\gamma = \alpha + i\beta$ can be expressed as

$$\alpha_{nm} = \left(\frac{u_{nm}}{2\pi}\right)^2 \frac{\lambda^2}{a^3} \frac{(\nu^2+1)}{2\sqrt{\nu^2-1}}, \tag{2.36}$$

$$\beta_{nm} = \frac{2\pi}{\lambda}\left(1 - \frac{1}{2}\left[\frac{u_{nm}\lambda}{2\pi a}\right]^2\right). \tag{2.37}$$

Since the attenuation constant is proportional to λ^2/a^3, transmission is improved for large inner diameters. Higher-order modes experience loss proportional to u_{nm}^2.

Incoupling of Gaussian beams

When coupling a Gaussian beam into a capillary fiber, the optimal overlap with the fundamental hybrid mode and thus the highest coupling efficiency to this mode occurs when the ratio between the beam waist w_0 and the fiber inner radius a is approximately 0.64 [41]. In Figure 2.7 on the left, the coupling efficiency of a Gaussian beam with radius w_0 to the first five hybrid modes EH_{1m} with m ranging from one to five is shown. EH_{nm} with $n > 1$ are not considered, since there is a minimum in the center that leads to poor overlap for any distribution with a central maximum.

Additionally, the intensity profile of the fundamental hybrid mode is depicted in Figure 2.7 on the right, together with the Gaussian that results in the best coupling efficiency.

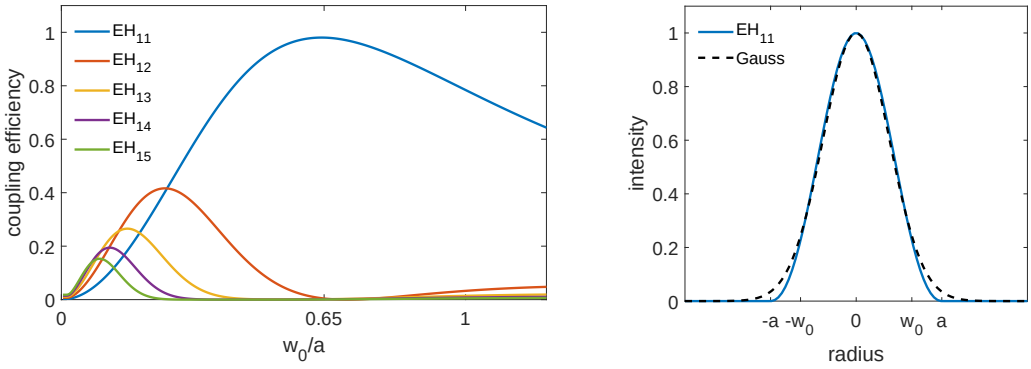

Figure 2.7.: Left: Coupling efficiency of a Gaussian beam with radius w_0 to the first five hybrid modes for a fiber with inner radius a. Right: Intensity profile of the fundamental hybrid mode together with the Gaussian that leads to the best coupling efficiency.

Bending loss

Another important variable for guiding loss in capillary fibers is the bending radius. Opposed to standard optical fibers that have a high refractive index core and a lower refractive index cladding, bending loss is a severe issue for hollow core fibers. The overall attenuation is given by the sum of the attenuation constant for a straight waveguide (Equation (2.36)) and the attenuation constant α_R depending on the radius of curvature R. The constant α_R is not only proportional to $1/R^2$, but also to a^3/λ^2 [40], yielding

$$\alpha_R \propto \frac{a^3}{R^2 \lambda^2 u_{nm}^2}. \tag{2.38}$$

Comparing Equations (2.36) and (2.38) yields: The lower the attenuation constant α_{nm} is, the higher the loss due to bending becomes. Therefore, the only way to achieve high transmission in hollow core waveguides is a large bending radius. Rigid capillaries have widely been used for this purpose, but there are limitations in length. To gain access to longer nonlinear interaction regions, stretched capillary fibers with large bending radii are a viable option [42].

When a flexible fiber with thin walls is fixed to holders at both sides, it forms a catenary that is determined by the gravitational force per unit length W and by the horizontal stretching force T. The ratio between the forces $b = T/W$ is defining the exact shape of the fiber, which can be described by the function

$$y = b \cosh\left(\frac{z}{b}\right), \tag{2.39}$$

where y is the vertical and z the horizontal coordinate. The smallest radius of curva-

ture is present in the center, where it is exactly given by b. Since hollow capillaries with thin walls are extremely light, only weak stretching forces are necessary to achieve bending radii of several thousands of meters that have a negligible effect on the attenuation [42]. In this work, a commercial setup to mount stretched fibers produced by $few-cycle^{TM}$ was used together with a five meter long fused silica capillary.

2.3.2. Propagation effects in gas filled fibers

When short laser pulses propagate in a gas filled capillary, various effects - wanted or unwanted - take place. In this thesis, the spectral broadening due to SPM is exploited, but of course there are more mechanisms to be considered. The dispersion and attenuation of the waveguide are given by Equations (2.37) and (2.36). In comparison, the dispersion and absorption of the noble gas are rather small, but they still need to be taken into account. Additionally, self-steepening and self-focusing should be considered and for high-intensity pulses, ionization is another effect that may influence the shape of the output pulse. In order to achieve controlled spectral broadening in a hollow waveguide with minimal losses, one tries to avoid self-focusing by keeping the peak power of the pulse below a certain threshold. Additionally, the peak intensity should be kept below the threshold for photoionization. [43]
In Chapter 4, numerical simulations of the propagation of light in a gas filled capillary are described in detail together with the underlying propagation equations.

2.4. Optical autocorrelation

Autocorrelation techniques enable the measurement of short signals, such as ultrashort laser pulses, without the necessity of fast detectors. Moreover, they can also provide spectral information about the pulse. An overview of autocorrelation methods and further tools for pulse characterization can be found in [44]. Section 2.4.3 focusses on the fringe-resolved interferometric autocorrelation (FRIAC) that is employed to measure the pulse duration of the generated UV pulses in Chapter 5.2.

2.4.1. Field autocorrelation

The field autocorrelation is obtained by coherent superposition of two collinear replica of the same pulse with delay τ. The resulting intensity depends on the sum of the fields $E(t)$ and $E(t-\tau)$, written as

$$I_{field}(\tau) \propto \int_{-\infty}^{\infty} |E(t) + E(t-\tau)|^2 dt, \tag{2.40}$$

where E is the complex representation of the electric field and $I \propto |E|^2$ the related intensity. Equation (2.40) can be expanded in three terms, resulting in

$$I_{field}(\tau) \propto \int_{-\infty}^{\infty} |E(t)|^2 + |E(t-\tau)|^2 + 2\,\Re(E(t)E^*(t-\tau))dt, \tag{2.41}$$

where the first two terms contain information about the pulse energy and do not depend on the delay τ after the integration. Thus, they lead to a constant offset of the trace. The third term is determined by the field autocorrelation. The Fourier transform of the field autocorrelation yields the spectrum of the pulse, but there is no information about the temporal characteristics that could be obtained. In Figure 2.8 on the left, I_{field} of a transform-limited Gaussian pulse is shown. Oscillations at the pulse frequency are present, distributed symmetrically above and below a constant offset.

2.4.2. Intensity autocorrelation

To measure the intensity autocorrelation (IAC), a second-order nonlinear process, such as SHG, is exploited. One obtains a signal proportional to $(E(t) + E(t-\tau))^2$ but filters out only the components that depend on the cross-product $E(t)E(t-\tau)$, which leads to

$$I_{IAC}(\tau) \propto \int_{-\infty}^{\infty} |E(t)E(t-\tau)|^2 dt \propto \int_{-\infty}^{\infty} I(t)I(t-\tau)dt. \tag{2.42}$$

The width of the IAC is correlated with the temporal width of the intensity. For a Gaussian pulse, the autocorrelation width is $\sqrt{2}$ times longer than the pulse duration. I_{IAC} of the same pulse as for the field autocorrelation is depicted in Figure 2.8 in the center. Opposed to the field autocorrelation, there are no oscillating components.

2.4.3. Fringe-resolved interferometric autocorrelation

The fringe-resolved interferometric autocorrelation (FRIAC) is an experimental method that combines quantities related to the pulse duration as well as the spectrum in a single measurement. Similar to the field autocorrelation, it also relies on coherent superposition of two collinear replica of the same pulse - but in this case, they drive a nonlinear process. For a second-order process, the resulting intensity reads

$$I_{FRIAC}(\tau) \propto \int_{-\infty}^{\infty} |(E(t) + E(t-\tau))^2|^2 dt. \tag{2.43}$$

Equation (2.43) may be further expanded in four terms with different characteristics [45], namely

$$
\begin{aligned}
I_{FRIAC}(\tau) \propto & \int_{-\infty}^{\infty} |E^2(t) + 2E(t)E(t-\tau) + E^2(t-\tau)|^2 dt \\
= & \int_{-\infty}^{\infty} (|E(t)|^2)^2 + (|E(t-\tau)|^2)^2 dt && (2.44) \\
& + \int_{-\infty}^{\infty} 4\,\Re\left\{(E(t)E^*(t-\tau))\right\}(|E(t)|^2 + |E(t-\tau)|^2) dt && (2.45) \\
& + \int_{-\infty}^{\infty} 2\,\Re\left\{(E(t)E^*(t-\tau))^2\right\} dt && (2.46) \\
& + \int_{-\infty}^{\infty} 4\,|E(t)|^2\,|E(t-\tau)|^2 dt. && (2.47)
\end{aligned}
$$

The first term of I_{FRIAC} (Equation (2.44)) is determined by the intensity $I \propto |E|^2$ of the two replica of the pulse and leads to a constant offset of the overall signal. The second term (Equation (2.45)) contains the field autocorrelation that oscillates at the frequency of the pulse and is scaled by the sum of the intensities $|E(t)|^2 + |E(t-\tau)|^2$ of the two replica. Spectral information can be acquired from this term. The third term (Equation (2.46)) is given by the field autocorrelation of the second-harmonic of the pulses that oscillates at double the frequency of Equation (2.45). The fourth term (Equation (2.47)) is proportional to the IAC, allowing for an evaluation of the pulse duration.

In Figure 2.8 on the right, I_{FRIAC} of the same pulse as for the other two cases is shown. The oscillations around a constant offset exhibit a ratio of one to eight between the peak and the baseline. Additional to the trace, the non-oscillating part of the signal, which is the intensity autocorrelation together with a constant offset, is depicted. Numerically, this part can be extracted from an experimental trace by low-pass filtering the data such that all oscillating parts vanish [46].

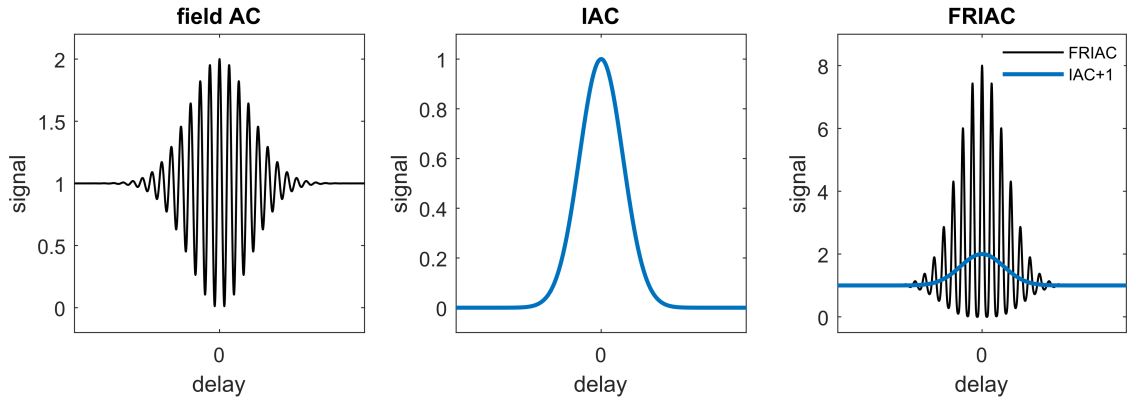

Figure 2.8.: Different autocorrelation signals of the same transform-limited Gaussian pulse. Left: Field autocorrelation. Center: Intensity autocorrelation. Right: FRIAC trace together with the intensity autocorrelation plus constant offset.

Pulses that are not transform-limited typically show deviations from the ideal shape in their FRIAC traces. Figure 2.9 depicts calculated traces of an initially transform-limited Gaussian pulse (10 fs FWHM) with additional GDD, TOD and FOD. Since the effect of higher-order dispersion is rather similar for all orders, it is not straightforward to identify the individual contributions in an experimental trace.

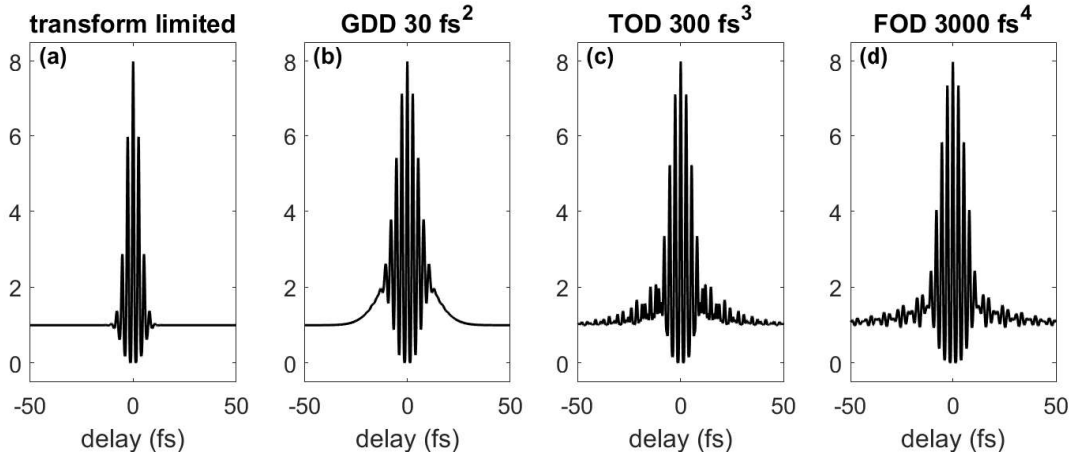

Figure 2.9.: FRIAC traces of a transform-limited Gaussian pulse centered at 400 nm with 10 fs FWHM pulse length (a) and of the same pulse with additional dispersion of 30 fs^2 GDD (b), 300 fs^3 TOD (c) and 3000 fs^4 FOD (d).

Higher-order processes

Besides second-order processes, also higher-order processes may be exploited to perform FRIAC measurements. The resulting intensity for a process of the order n is given by

$$I_{FRIAC}(\tau) \propto \int_{-\infty}^{\infty} |(E(t) + E(t-\tau))^n|^2 dt. \tag{2.48}$$

Equation (2.43) is a special case, where the exponent n is two. For the sake of readability, the individual components for third- and fourth-order processes will not be expanded here but an overall intuition for the behavior of the traces is shown in Figure 2.10. On the left (a-c), the traces for the same transform-limited Gaussian pulse are depicted for second-, third-, and fourth-order processes. On the right (d-f), the corresponding spectra (obtained by Fourier transform) are given. The frequencies present are integer multiples of the fundamental frequency of the pulse - the number of frequency peaks is determined by the order of the process. For increasing orders, the oscillations around the constant offset show a rapidly changing ratio between the peak and the baseline. For $n = 3$, the ratio is already 1:32, for $n = 4$, the ratio is 1:128. The general rule for the ratio depending on n is $1{:}2^{(2n-1)}$.

Analogous to the second-order FRIAC traces, also for higher-order processes, a low-pass filtered signal can be numerically extracted from the oscillating experimental trace to determine the pulse duration, assuming a pure process of the order n and a Gaussian pulse shape. While the autocorrelation width is 1.41 times the pulse duration for $n = 2$ (see Section 2.4.2), this factor decreases for higher orders. For $n = 3$, the autocorrelation width is 1.22 times the pulse duration, and for $n = 4$, the autocorrelation width is only 1.07 times the pulse duration.

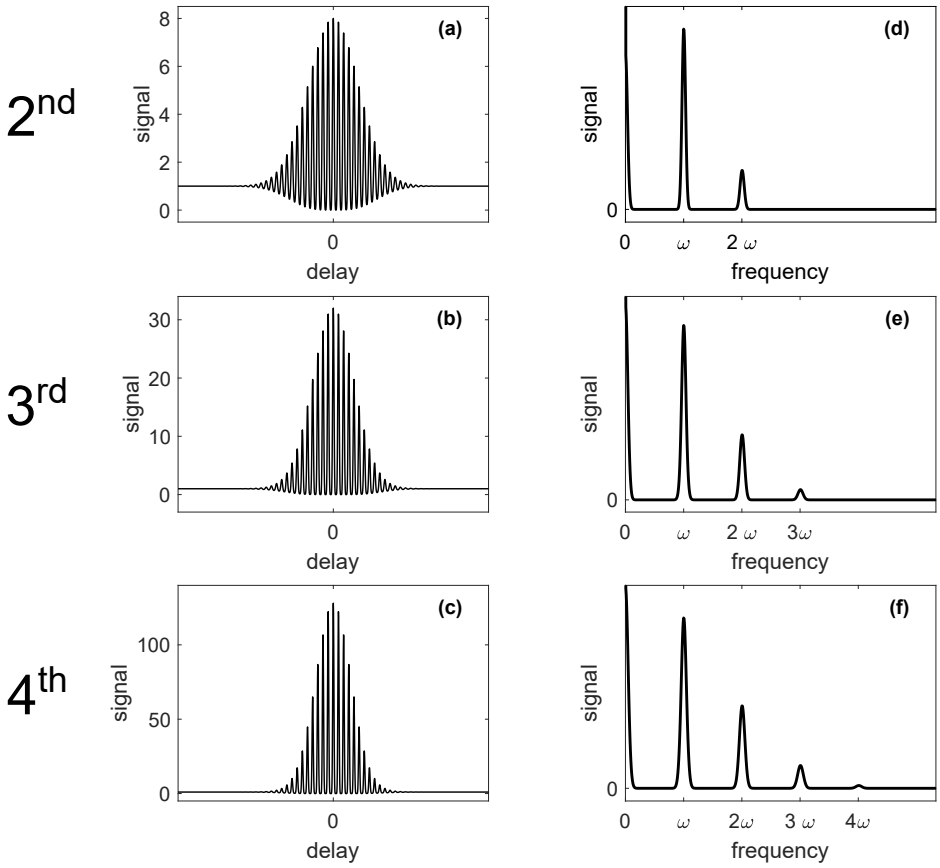

Figure 2.10.: FRIAC traces (a-c) and corresponding spectra (d-f) for processes of second, third and fourth order. The fundamental frequency of the pulse is denoted by ω. The spectra are obtained by Fourier transform of the traces and plotted on a linear scale.

3. Experimental setup

To reach the VUV spectral region, a step-wise manipulation scheme of ultrashort laser pulses generated by a Ti:Sa laser system in the NIR (800 nm) is performed. Initially, the pulses undergo frequency-doubling via SHG in a BBO crystal, thereafter they are coupled into a gas-filled HCF. Here, spectral broadening due to SPM occurs. Subsequently, the pulses are temporally compressed in a 4f geometry that also allows for spectral filtering. Finally, to reach the VUV range, the third harmonic of the short UV pulses is generated by focusing the beam into a gas cell. Two different gas cell designs have been implemented: one featuring a straightforward static configuration, while the other employs a more advanced pulsed mechanism.

3.1. Femtosecond laser system

The femtosecond laser system (Pulsar, Amplitude Technologies) used in this thesis consists of commercially available parts, which are combined in a chirped pulse amplification (CPA) scheme, delivering short NIR pulses at a repetition rate of 100 Hz. A schematic overview is shown in Figure 3.1.

A passive mode-locked Ti:Sa oscillator (Synergy Pro, Femtolasers) delivers sub-10 fs pulses at a repetition rate of 75 MHz with a central wavelength of 770 nm and a bandwidth of 85 nm. Those pulses exhibit a rather low pulse energy around 4 nJ.
To enable amplification, the pulses are first stretched in an aberration-free Öffner-triplet single-grating configuration. Subsequently, they proceed into a two-stage amplification setup comprising a regenerative amplifier followed by a multipass amplifier. Since higher pulse energies are achievable at reduced repetition rates, a combination of Pockels cells and polarizers is used to lower the repetition rate in the regenerative cavity to 1 kHz. The Ti:Sa crystal within the regenerative amplifier is pumped by a diode-pumped Nd:YLF laser (DM30-527, Photonics Industries (until March 2023) / Terra 527-50-M, Continuum (since March 2023)). Inside the cavity, an acousto-optic programmable gain filter (Mazzler, Fastlight) decreases gain-narrowing. The pulses delivered by the regenerative amplifier possess an energy of up to 0.7 mJ.

After the regenerative amplifier, the system is divided into two branches. The Pockels cells and polarizers act as pulse pickers, assigning every 10th pulse to the 100 Hz branch. The remaining 900 Hz share the same regenerative amplifier but are routed to a separate multipass amplifier. In this work, only the 100 Hz branch is used and discussed.

In the multipass amplification stage, each pulse passes through a Ti:Sa crystal five times, which is again pumped by a diode-pumped solid-state laser (SpitLight DPSS 250, Innolas). Subsequently, the pulses undergo re-compression by a double-grating compressor. Additionally, the spectral phase of the output is adapted, utilizing an acousto-optic programmable dispersive filter (Dazzler, Fastlight) before the regenerative amplifier. Individual manipulation of dispersion terms up to the fourth order allows for flattening the spectral phase. At the compressor output, the energy reaches up to 19 mJ, with a pulse duration of 30 fs FWHM and a spectral bandwidth of 45 nm. The pulse duration and spectral phase are measured via spectral phase interferometry for direct electric-field reconstruction (SPIDER) [47] using a commercial device (APE). The $1/e^2$ waist w_0 of the collimated beam behind the compressor is 10.5 mm, determined by a knife-edge scan.

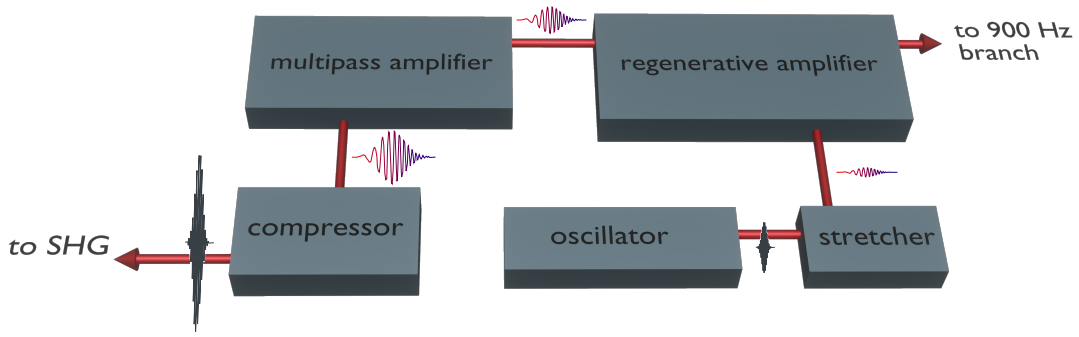

Figure 3.1.: Architecture of the femtosecond laser system together with a depiction of the amplification steps. Note that this is only an illustration of the CPA process and not to scale by any means.

3.2. SHG and transport to the fiber

The subsequent manipulation steps - SHG in a BBO crystal and coupling into the HCF - are performed within a vacuum environment ($< 10^{-1}$ mbar) to minimize dispersion and nonlinear effects arising from propagation through air. An overview of the beam path is depicted in Figure 3.2.

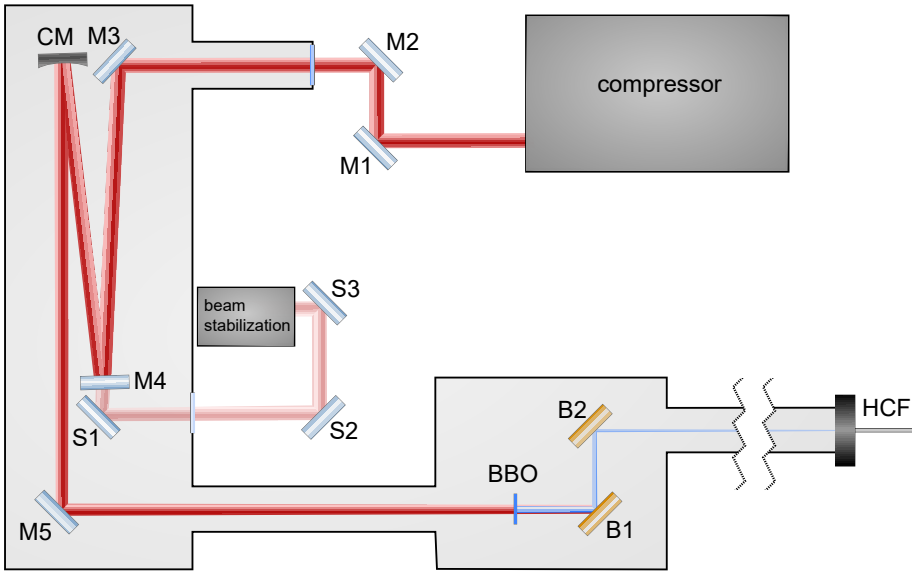

Figure 3.2.: Geometry of the setup between laser system and hollow core fiber including SHG in a BBO crystal to convert the pulses from 800 nm to 400 nm.

Behind the compressor, the beam is sent into the first vacuum chamber, where it is directed onto a curved mirror (CM) positioned to minimize the incident angle, thus reducing astigmatism. CM couples the beam directly into the fiber utilizing a relatively long focal length of 5 m. Beam stabilization is facilitated by a commercial system (Aligna, TEM), which manipulates two mirror holders with two axes each. While the first mirror is positioned inside the compressor box and not visible in Figure 3.2, the second mirror is the last one before the vacuum chamber (M2). The stabilization system's near and far field detectors are supplied with input from the leakage of M4, which is transported by the mirrors S1-3. Additionally, M5 is equipped with piezo actuators (Picomotor, New Focus) that enable manual control over the focus position at the fiber entrance. M1-5 and S1-3 are dielectric mirrors optimized for 800 nm, whereas CM is made of protected silver.
For the next manipulation step, the beam is sent to a connected vacuum chamber, where the slightly convergent 800 nm light passes through a thin BBO (diameter: 22 mm, thickness: 0.28 mm). Here, SHG with type I phase-matching is exploited to create 400 nm pulses. The peak power density of the NIR on the BBO is between 3 and 4×10^{11} W/cm^2. In the UV, pulse energies of up to 7 mJ can be achieved, resulting in a conversion efficiency of more than 35 %. Behind the BBO, the remaining fundamental is filtered out by the dielectric mirrors B1-2 (045-0400, Eksma Optics) before continuing the propagation to the fiber.

3.3. Stretched hollow core fiber

The HCF is 5 m long and chosen to have a rather large inner diameter of 500 µm to limit the peak intensity and thus hinder unwanted effects such as self-focusing or ionization when high-energy pulses are propagating in the fiber. The outer diameter of the capillary is 1/32" ≈ 0.8 mm. The fiber setup utilizes a commercially available system ($few-cycle^{TM}$) that comes with an adjustable holder (two axes translation and two axis tilt) for the entrance side and a holder equipped with a rotation handle to straighten the fiber along with adjustment options for the tilt (two axes) at the exit side. Both ends of the glass capillary are protected by a ceramic piece. At the entrance side, the piece may be chosen in such a way that it offers reduced material damage by enlarging the surface area in form of a conical shape. The setup is operated in a pressure gradient mode, where the gas inlet is located at the exit side and the entrance side is positioned in a vacuum environment, leading to a steady flow in the capillary. The pressure gradient reduces ionization and other high-intensity effects, since the lowest pressure occurs at the input, where the pulse is shortest. Furthermore, helium was chosen as the nonlinear medium for SPM, as it exhibits a high ionization energy of 24.69 eV [48].

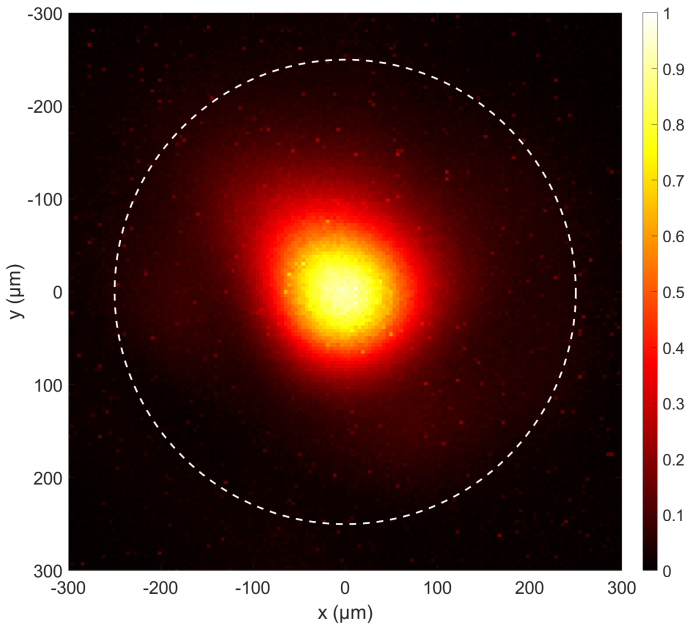

Figure 3.3.: Beam profile at the fiber entrance together with the dimension of the fiber core (dashed white).

The beam is coupled into the fundamental mode of the fiber to reduce propagation loss. The waist of the focus at the fiber input was chosen to be close to the theoretical optimum of $w_0/a \approx 0.64$ (see Figure 2.7). For a radius of $a = 250$ µm, the desired Gaussian beam waist is $w_0 \approx 160$ µm. Figure 3.3 shows the beam profile at the fiber entrance. The beam waist is slightly more narrow than the theoretical optimum (≈ 150 µm).

The HCF output spectrum strongly depends on the energy and spectral phase of the input (see Chapter 4). Via the acousto-optic programmable dispersive filter in the laser system, the spectral phase of the 400 nm pulse cannot directly be addressed, only the fundamental 800 nm pulse may be manipulated, leading to a strong correlation between spectral phase and energy of the 400 nm pulse. Consequently, the spectral phase is usually optimized for maximum energy and not used to manipulate the shape of the output spectrum.

Figure 3.4 depicts the beam path behind the fiber. The divergent beam is collimated by a curved mirror (CM), which has a focal length of 4 m. Subsequently, the beam is transported to a 4f setup to temporally compress the pulses. CM and M1 are made of UV-enhanced aluminum, whereas M2 is a dielectric mirror optimized for the spectral range between 380 nm and 420 nm (042-0400-i0, Eksma Optics) to enhance the overall transmission. The entire arrangement is inside vacuum chambers and tubes to minimize the exposure of the broadband UV radiation to ambient air and humidity. This is of special importance close to the fiber output, where the beam diameter is still small. The chambers may be filled to a pressure of 2 bar to realize the pressure gradient inside the hollow core fiber. Since the beam expands after exiting the fiber, the influence of the propagation in gas behind the fiber exit on the output spectrum is negligible. To enable fine alignment while the system is in operation, CM can be manipulated from outside using feedthroughs. Before the beam reaches the 4f setup, which operates in ambient air, it passes through a thin fused silica window (W).

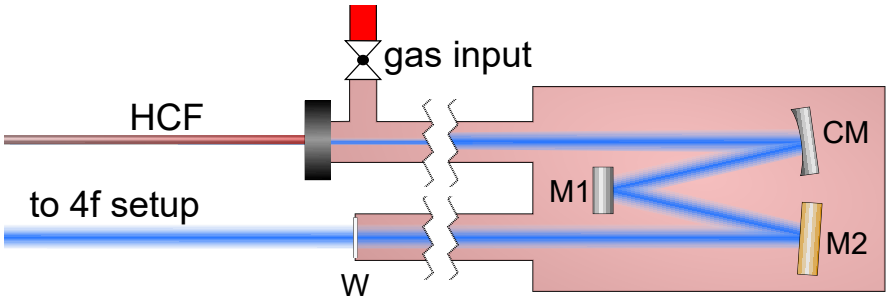

Figure 3.4.: Geometry behind the hollow core fiber including collimation and steering of the beam.

3.4. Dispersion compensation in a 4f setup

A common concept in pulse shaping applications are 4f setups [49]. In general, they consist of a dispersive element (such as a grating or prism) followed by a focusing element (such as a lens or mirror) placed at a distance equal to one focal length ($1f$), another focusing element at twice the focal length ($2f$), and finally, a second dispersive element at a distance equal to one focal length ($1f$). When a 4f setup is perfectly aligned, it becomes dispersion free. Additionally, 4f geometries allow for phase modulation in the Fourier plane, for instance, through a simple mask or spatial light modulator (SLM). Figure 3.5 depicts a perfectly aligned 4f setup comprising two gratings and two lenses, along with a mask positioned in the Fourier plane.

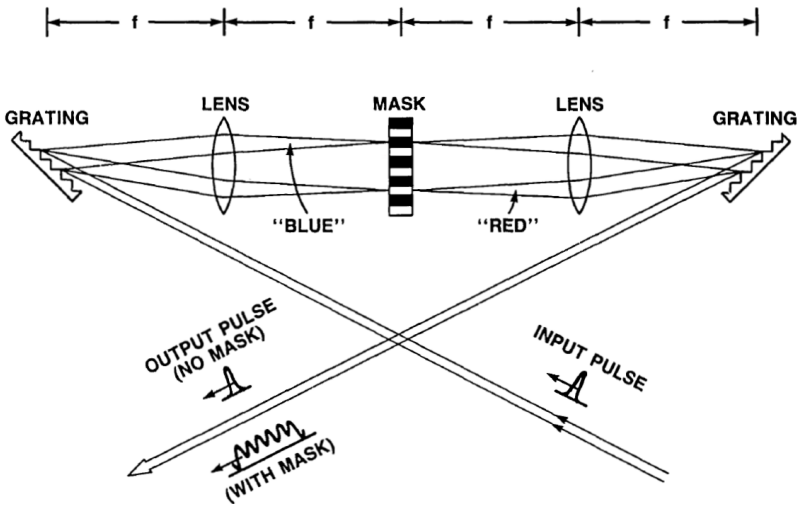

Figure 3.5.: Schematic depiction of a 4f setup with reflection gratings, lenses and a mask in the Fourier plane, taken from [49].

Misalignment in such systems results in various effects, including additional GDD, spatial and angular chirp, and pulse front tilt. Deviation from a perfect 4f geometry can be exploited to manipulate dispersion [50]. Another possibility to adjust the GDD is by introducing a tilted cylindrical lens at the Fourier plane of the arrangement [51]. In this work, a combination of multiple degrees of freedom in a detunable 4f setup is exploited to compensate for the accumulated dispersion after the propagation through the gas-filled HCF.

The 4f setup built in this thesis consists of only one volume phase holographic transmission grating (1400 lines/mm, Wasatch Photonics), one cylindrical lens ($f = 300$ mm), and a retro-reflector composed of two dielectric mirrors (045-0400, Eksma Optics). As illustrated in Figure 3.6, the arrangement is configured such that the beam passes through the grating and the lens twice. To minimize the required grating size, the beam is redirected onto the same region of the grating, leading to an angle of 3° between the incoming/outgoing beams and the horizontal axis.

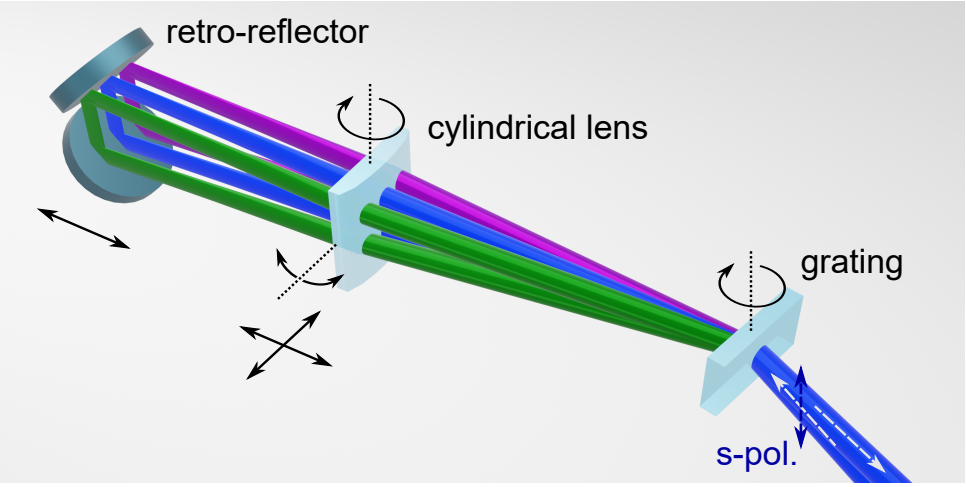

Figure 3.6.: Geometry of the 4f setup. The incoming beam (blue/dashed white arrow) is split up at the grating in three exemplary colors: green, blue, and (ultra)violet. The cylindrical lens parallelizes the incoming beams. The Fourier plane with line foci for each color is located between the two mirrors of the retro-reflector. The second pass through the lens directs the colors at one position on the grating, resulting in a recombined outgoing beam (blue/-dashed white arrow). The solid black arrows indicate degrees of freedom for alignment and dispersion manipulation. The dashed blue arrow indicates the direction of polarization of the incoming light.

The transmission grating is optimized for a wavelength of 380 nm and used in first order Littrow configuration (sometimes referred to as Bragg incidence), where the minus first and zero order transmitted through the grating propagate symmetrically with respect to the grating normal (see Figure 3.7). The theoretical diffraction efficiency for the first order for one polarization can be close to 100% in such a geometry [52]. In the setup constructed in this work, the light is s-polarized and the angle of incidence and diffraction of the first order is 15.4° to the grating normal.

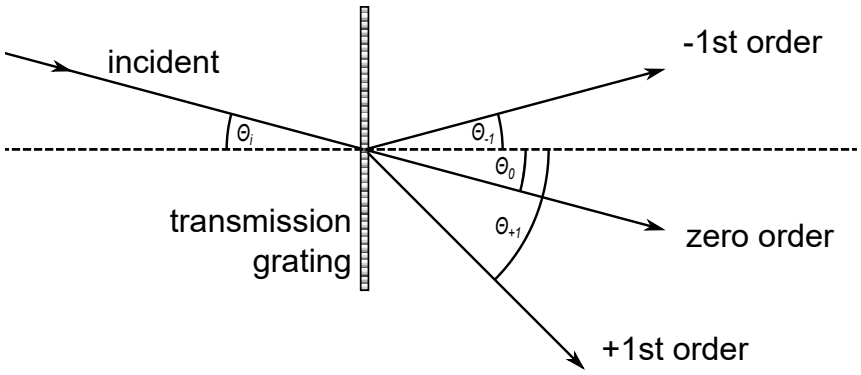

Figure 3.7.: First order Littrow configuration for a transmission grating. The angle of the incident light to the grating normal Θ_i is equal to the angle of the -1st order Θ_{-1} and the angle of the zero order Θ_0.

There are multiple degrees of freedom used for adjustment in the setup, indicated by arrows in Figure 3.6:

- Rotation of the grating to optimize the transmission.
- Position (two axes) of the cylindrical lens to manipulate the GDD and center the lens with respect to the beam.
- Rotation and tilt of the cylindrical lens to further manipulate the dispersion, compensate for the wavefront error introduced by detuning the 4f setup, and mitigate astigmatism.
- Position of the retro-reflector to center the Fourier plane between the mirrors.

In Chapter 4.3, numerical simulations of the spectral phase depending on the detuning of the 4f geometry are described in detail.

Key challenges in building setups operating in the UV range for high peak power pulses include the damage threshold of most coatings, particularly crucial for focused beams, and the fundamental limitations of simple metallic surfaces with respect to reflectivity in this spectral region. Although enhanced aluminum offers improved reflectivity compared to other metals, the reflectivity never exceeds 95%, significantly impacting the overall system efficiency, especially in case of multiple reflections. Moreover, the efficiency of reflective gratings tends to be inferior compared to the NIR. Consequently, a transmission grating and a lens were chosen instead of reflective elements.

The additional dispersion accumulated in the material of the transmission grating and cylindrical lens is compensated together with the dispersion introduced by the gas-filled HCF by detuning the 4f geometry. The cylindrical lens is advantageous compared to a spherical lens, since the line foci in the Fourier plane lead to a reduced peak power density on the mirrors of the retro-reflector.

With only two reflections by dielectric mirrors (R>99.5% for 380-420 nm), the overall transmission of the 4f setup is measured to be 73%. This results in a calculated efficiency of the transmission grating of more than 85% for one pass.

An additional feature of the 4f setup is the ability to manipulate pulses in frequency space in the Fourier plane. By placing a simple amplitude mask between the two mirrors of the retro-reflector and blocking one part of the spectrum, the central frequency of the exiting pulses can be shifted. In Chapter 5, the short UV pulses compressed and manipulated by the 4f setup are analyzed in detail using the FRIAC technique described in Chapter 2.4.3.

3.5. Harmonic generation

After compression, the short UV pulses are focused into a noble gas medium to reach the VUV spectral range by THG. A schematic depiction of the optical setup between the 4f setup and the gas cell is presented in Figure 3.8. Initially, the UV beam undergoes two reflections by dielectric mirrors (M1-2) to realize a small angle of incidence on the focusing mirror (CM). Subsequently, the s-polarized UV light is transferred into vacuum via a fused silica window positioned at Brewster's angle (BW). In the first vacuum chamber, the beam encounters two more reflections by dielectric mirrors (M3-4). M4 is equipped with piezo actuators (Picomotor, New Focus), offering precise control over the focal position in the gas cell. The gas cell itself is located within a connected vacuum chamber, positioned at a distance corresponding to the focal length from CM. The focal length is 2000 mm for most of the data analyzed in Chapter 6. Initial measurements were conducted with a focal length of 3000 mm. However, the conversion efficiency could be improved by choosing a slightly tighter focusing geometry.

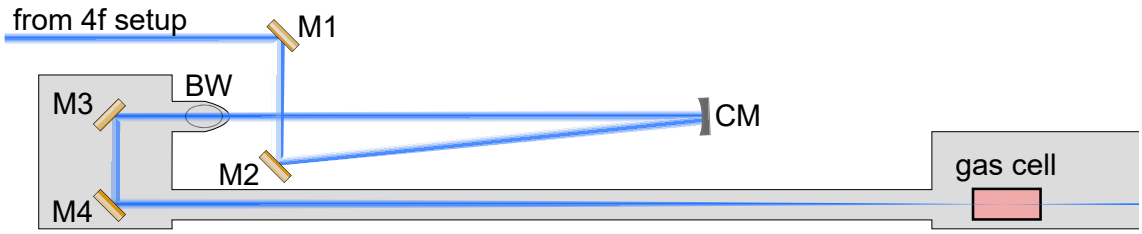

Figure 3.8.: Geometry of the beam path between the 4f setup and the gas cell.

Two different variants of gas cell have been realized, the first is a relatively straightforward static approach, while the second involves a more complex design with a pulsed nozzle. This pulsed nozzle configuration allows for the generation of higher pressures within a confined volume, synchronized with the repetition rate of the laser. Both cells have been operated in the same vacuum chamber, which consists of up to three sub-chambers with removable walls, enabling individual pumping. A three-stage turbomolecular pump (Pfeiffer, SplitFlow 310) that offers three gradations of compression ratio with separate flanges (I, II and III in Figures 3.10 and 3.12) is used to pump the sub-chambers individually. In a differential pumping scheme, the gas for THG can be efficiently pumped, while at the same time a pressure of $< 10^{-5}$ mbar is maintained behind the source.

The beam profile in the focal region is notably influenced by the alignment of the 4f setup. As mentioned above, adjustments of the tilt and rotation of the cylindrical lens in the 4f geometry are crucial for minimizing astigmatism. Figure 3.9 presents M^2 measurements corresponding to focal lengths of 2000 and 3000 mm. For the shorter focal length, yielding a tighter focus, the measured minimal waist was 73 µm. This, together with a pulse duration of 10 fs (see Chapter 5) and an energy of 1 mJ, results in a peak power density of 1.2×10^{15} W/cm^2. For the longer focal length, the minimal waist is given by 87 µm, resulting in a peak power density of 8.4×10^{14} W/cm^2.

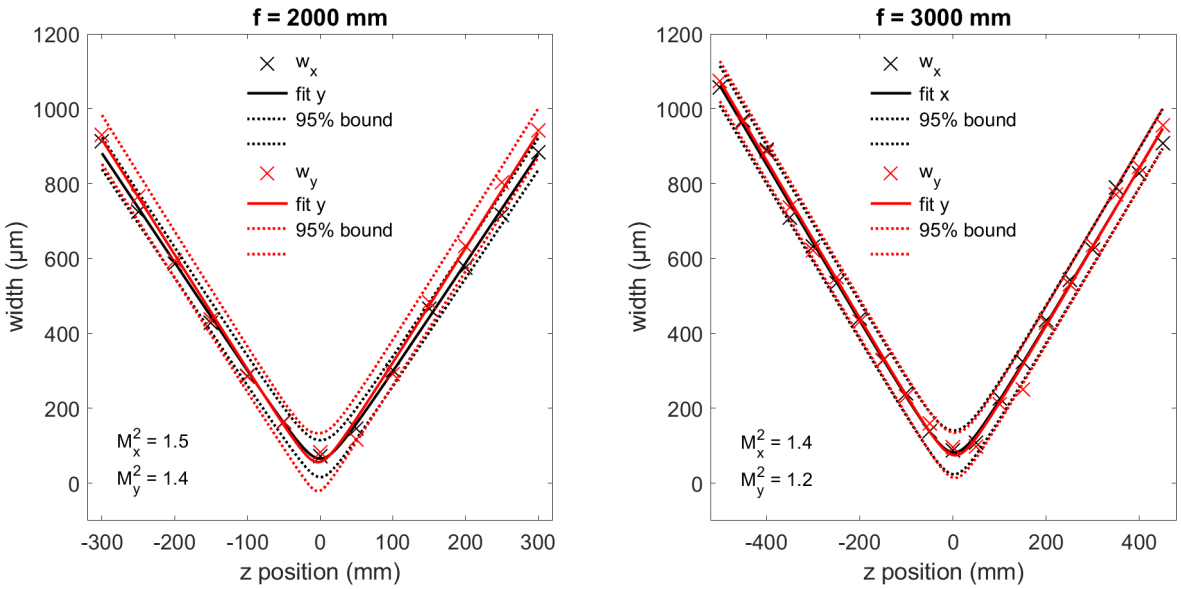

Figure 3.9.: Beam waist scans around the focus for THG along the propagation direction (z) for both the x- and y-direction for focal lengths of 2000 and 3000 mm. Additionally, the fit function determining M^2 values for both directions is shown. The dashed lines indicate the 95% confidence interval of the fit.

3.5.1. Static gas cell

The static gas cell is a construction that has been utilized in previous setups to directly create harmonics of the fundamental 800 nm laser pulses [53–56]. A cut through the cell's geometry is depicted in Figure 3.10 on the left. The gas-filled volume of the cell is terminated by two aluminum foils (labeled 1 and 2) with pinholes, created by the UV beam itself. To adjust the cell's length in vacuum, the tube with the smaller diameter can be moved in and out using a linear stage (see Figure 3.10 on the right). Gas pressure inside the cell is regulated by a dosing valve outside the vacuum chamber and monitored using a pressure gauge implemented in the inlet line. The inlet line is connected to the cell via a feedthrough in the first section of the vacuum chamber (S1 in Figure 3.10 on the right). Phase-matching for the THG process is achieved by adapting both the length and pressure of the cell.

The first stage of the differential pumping scheme is provided by the cylindrical enclosure around the cell, connected to the entrance side (S1) and separated by a third aluminum foil (3) from the central chamber section (S2). Once again, the UV beam creates its own aperture in the foil. Subsequent differential pumping stages are implemented between the second and third section of the vacuum chamber (S2 and S3). Again, there is an aluminum foil with a hole dividing the two sections. Due to the increased beam size, the intensity is insufficient to create a hole, which is large enough for transmission without significant diffraction. Consequently, a small aperture is cut into the foil.

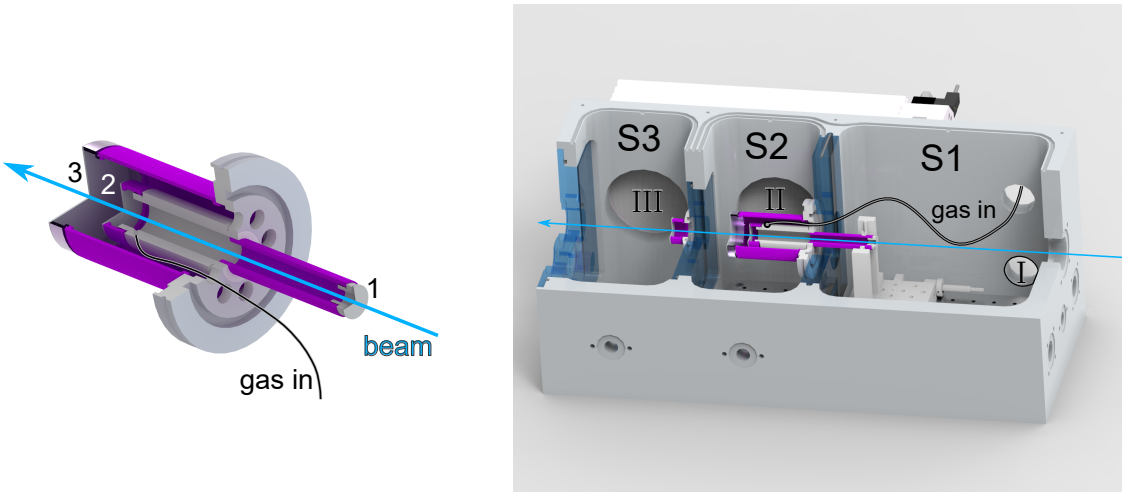

Figure 3.10.: Cut through the static gas cell (left) and entire vacuum chamber with sub-chambers S1-3 (right). The flanges I-III are used for the three stages of the turbomolecular pump.

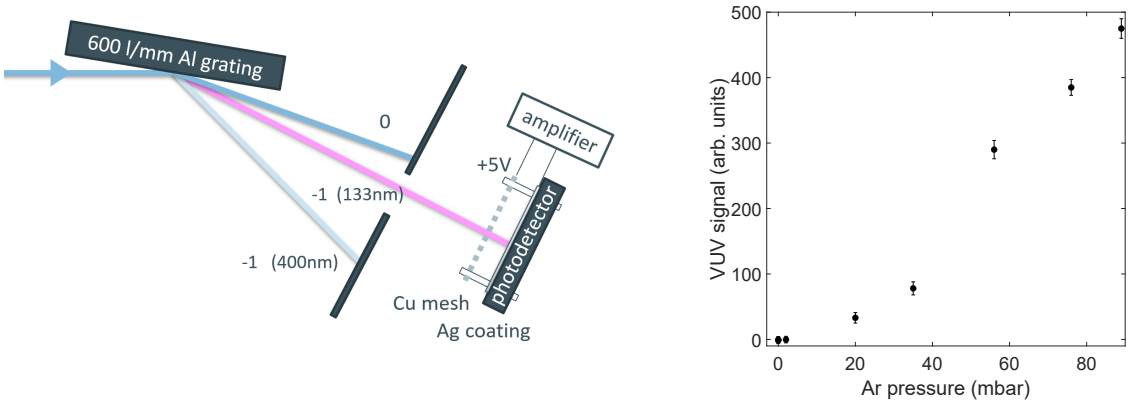

Figure 3.11.: Relative measurement of the generated VUV pulse energy - experimental geometry (left) and measured data (right). The third harmonic is separated from the fundamental by an aluminum diffraction grating. Only the -1st order of the 133 nm radiation arrives on the surface of a simple photodetector. The detector consists of a silver coated plate and a copper mesh with a bias voltage of 5 V.

Helium and argon have been tested for THG in the geometry described above. Typical operation conditions are the following: up to a pressure of 100 mbar in the inlet line to the cell, $< 10^{-1}$ mbar in section S1, $< 10^{-3}$ mbar in section S2 and $< 10^{-5}$ mbar in section S3. For helium, the pumping is less efficient and therefore the pressure in the cell must be kept lower compared to argon. In Figure 3.11, a relative measurement of the generated VUV pulse energy for different argon pressures is depicted. On the left, the measurement principle with an aluminum grating and a simple photodetector is shown. The data on the right indicates that saturation is not attained, and therefore higher VUV output could be expected, if the gas pressure in the cell could be increased. Similarly, longer cell lengths have enhanced the conversion efficiency. To overcome the limitations caused by pumping speed and gas flow, a pulsed construction has been implemented and is discussed in the following.

3.5.2. Pulsed nozzle

The benefit of a pulsed gas cell is a reduced overall gas load while reaching higher pressures in the nonlinear medium. Additionally, the gas is confined to a narrow channel with differential pumping (see Figure 3.12) to further improve the medium density for a given pumping speed. The lateral dimensions of the channel are $500 \times 500\,\mu m$ and the length is 1 cm. The aperture of the pulsed nozzle, through which gas is introduced into the channel in a symmetric and quasi-static manner, is located in the center of the channel. The opening time is 200 µs and the repetition rate is synchronized with the laser to 100 Hz. Besides repetition rate and opening time, the overall gas flow is influenced by the backing pressure of the gas and the voltage on the piezo opening the nozzle. This voltage is continuously tunable. On both sides of the channel, there are holes for differential pumping, which are connected to the first stage of the turbomolecular pump (I). Behind the holes, the geometry is again reduced in diameter to efficiently separate the gas volume in the channel from the outside. The chamber section surrounding the cell is pumped by the second stage of the turbomolecular pump (Figure 3.13, S1+2/II).

The assembly of the pulsed nozzle and gas channel is mounted onto a combination of two linear stages, one horizontal and the other vertical, and one goniometric stage to tilt the channel such that it is parallel to the beam. The entire setup is placed in the central section of the vacuum chamber with the wall to the first section removed, since the first stage of the pump (I) is directly connected to the gas cell. The third section of the vacuum chamber (S3) is again separated by the aluminum foil with an aperture and pumped by the third stage of the turbomolecular pump (III). The typical operation conditions are very similar to the case with the static gas cell, only the pressure in the inlet line to the cell may now be increased to more than 1 bar of

argon or xenon without being limited by pumping speed. The pressure in the line to the first stage of the pump (I) is $< 10^{-1}$ mbar, in the combined section S1+2 it is $< 10^{-3}$ mbar, and in section S3 $< 10^{-5}$ mbar.

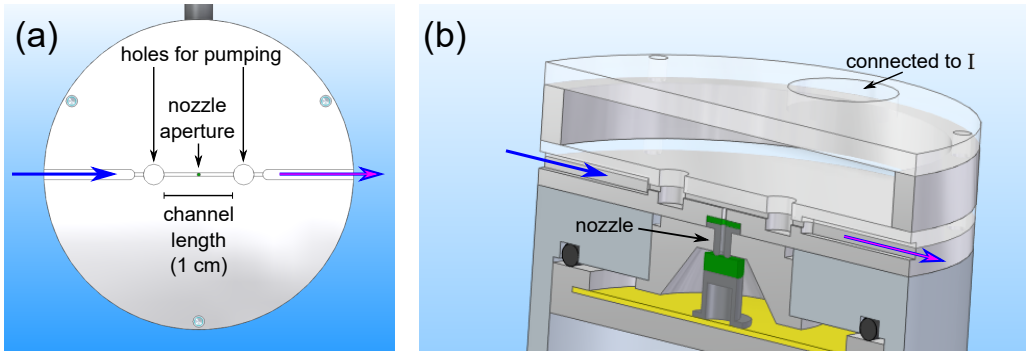

Figure 3.12.: Geometry of the pulsed gas cell - (a) top view of the channel, (b) vertical cut through the cell. The blue/violet arrows indicate the direction of the light.

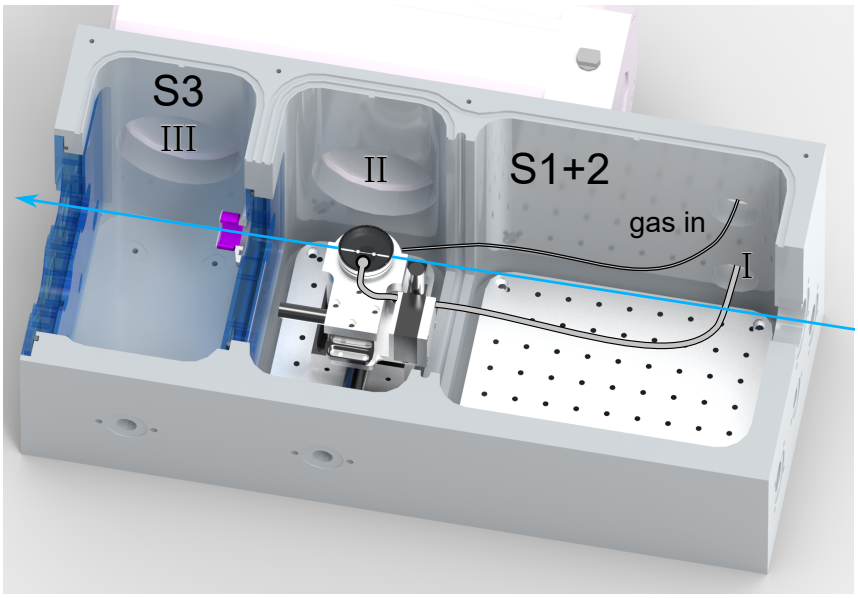

Figure 3.13.: Cut through vacuum chamber with the pulsed gas cell installed. The sections S1 and S2 are combined by removing the wall. The first stage (I) of the turbomolecular pump is directly connected to the cell for efficient pumping of the gas load.

In Figure 3.14, white light emission from ionized gas (xenon) in the channel is depicted. For recording the image, a pressure of 700 mbar is applied, which exceeds the optimal pressure for THG. The absence of light in the center is attributed to the acrylic glass lid being contaminated by sputtered aluminum from the channel walls by the UV pulses. It is evident that the distribution of ionized gas extends beyond the channel, reaching through the holes for differential pumping up to the wider opening leading to the surrounding vacuum chamber, where it abruptly terminates. The densest region, indicating the focal point, is situated within the channel behind the nozzle.

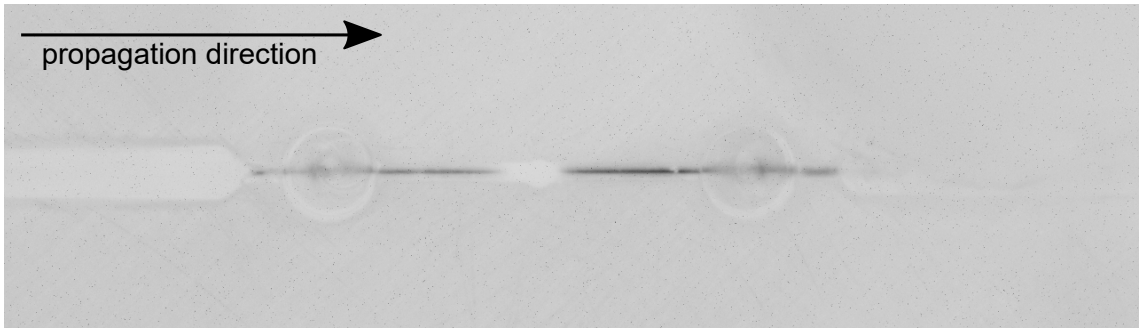

Figure 3.14.: White light emission from ionized gas (xenon) in the cell. The image is recorded with a long-pass filter (OG570, Schott) to exclude the 400 nm stray light. For better visibility, the colors are inverted.

The nonlinear media tested for THG include argon, helium, xenon and nitrogen/ambient air. Among these gases, xenon exhibits the highest conversion efficiency, followed by argon and nitrogen, while helium yields disappointing results. The reason for the exceptional characteristics of xenon compared to the other gases might be a resonance line close to 130 nm [48]. In Chapter 6, the energy measurement and spectral analysis of the generated VUV pulses is discussed in detail.

4. Numerical simulations

In this chapter, numerical simulations are presented regarding different stages of the step-wise manipulation scheme introduced in Chapter 3.

First, light propagation in a HCF (see Chapter 2.3 and 3.3) is discussed, employing two different approaches with corresponding propagation equations: the generalized nonlinear Schrödinger equation (GNLSE) and the unidirectional pulse propagation equation (UPPE). The GNLSE is solved using a 1D split-step Fourier method implemented in MATLAB, which is subsequently expanded to a 2D version exploiting modal decomposition into EH modes. The UPPE is solved using Luna.jl [57] and compared to the results of the GNLSE approach.

To simulate THG in gas as described in Chapter 3.5, the Luna.jl framework is utilized, which incorporates short pulse propagation in fibers as well as in free-space. Since third-order nonlinear processes and ionization effects are readily included, THG can be analyzed with minor adjustments to the original code.

Furthermore, a ray-tracing approach to dispersion manipulation in the detuned 4f setup introduced in Chapter 3.4 is discussed. The calculations are conducted in *Wolfram Mathematica* using the optical design package *Optica EM*.

4.1. Light propagation in a hollow core fiber

Analogous to Chapter 2.2, a general description of dispersive as well as nonlinear effects during propagation in optical fibers is provided by the wave equation (Equation (2.17))

$$\nabla^2 \boldsymbol{\mathcal{E}} - \frac{1}{c_0^2}\frac{\partial^2}{\partial t^2}\boldsymbol{\mathcal{E}} = \mu_0 \frac{\partial^2}{\partial t^2}\boldsymbol{\mathcal{P}}_{\boldsymbol{\mathcal{L}}} + \mu_0 \frac{\partial^2}{\partial t^2}\boldsymbol{\mathcal{P}}_{\boldsymbol{\mathcal{NL}}}, \tag{4.1}$$

where the linear ($\boldsymbol{\mathcal{P}}_{\boldsymbol{\mathcal{L}}}$) and nonlinear ($\boldsymbol{\mathcal{P}}_{\boldsymbol{\mathcal{NL}}}$) part of the polarization are separated. The wave equation directly originates from Maxwell's equations (Equations (2.12)-(2.14)), with the only assumptions being no free currents or charges and a non-magnetic medium. Various numerical methods are available to address the challenge of solving this type of differential equations, each offering distinct advantages for specific situations.

4.1.1. Nonlinear Schrödinger equation

In the GNLSE approach, several assumptions are made to solve Equation (4.1), resulting in a basic propagation equation that is suitable for pulses as short as 10 fs [58]. The approximations include:

- $\mathcal{P}_{\mathcal{NL}}$ is considered a small perturbation to $\mathcal{P}_{\mathcal{L}}$.
- The polarization is assumed to be maintained along the fiber, justifying a scalar approach.
- A slowly-varying-envelope approximation is applied, implying that the pulse envelope changes slowly in both time and space compared to the optical period.
- The nonlinear response is assumed to be instantaneous, neglecting the contribution of molecular vibration (Raman effect) to $\chi^{(3)}$. This assumption holds true for all noble gases.

Here, we outline the pathway to the GNLSE, while a complete derivation can be found for example in [58]. The electric field is expressed as

$$\boldsymbol{\mathcal{E}}(\boldsymbol{r},t) = \frac{1}{2}\hat{x}\left(F(x,y)A(z,t)e^{i(\beta_0 z-\omega_0 t)} + c.c.\right), \tag{4.2}$$

where $\hat{x}$ represents the unit vector of light polarization (assuming linear polarization in x-direction), $F(x,y)$ denotes the transverse field distribution, which is separated from $A(z,t)$, the slowly varying amplitude, and β_0 denotes the wavenumber.

The effective mode area A_{eff} is computed as

$$A_{eff} = \frac{\left(\int_{-\infty}^{\infty}\int_{-\infty}^{\infty}|F(x,y)|^2\,dxdy\right)^2}{\int_{-\infty}^{\infty}\int_{-\infty}^{\infty}|F(x,y)|^4\,dxdy}, \tag{4.3}$$

which necessitates knowledge about the spatial distribution of the fiber mode. For the fundamental EH_{11} mode of a fiber with core radius a, it is given by $A_{eff} = 0.48 \times \pi a^2$.

The nonlinear coefficient γ_{NL} is defined as

$$\gamma_{NL} = \frac{n_2\omega_0}{c_0 A_{eff}}, \tag{4.4}$$

where n_2 represents the nonlinear refractive index and c_0 denotes the vacuum speed of light.

Similar to the Taylor expansion of the spectral phase in Equation (2.5), the phase constant $\beta(\omega)$, which is the imaginary component of the propagation constant $\gamma = \alpha + i\beta$, is expanded into a Taylor series around the central frequency ω_0. The terms of the order n are given by

$$\beta_n = \left[\frac{d^n \beta}{d\omega^n}\right]_{\omega=\omega_0}. \tag{4.5}$$

Neglecting β_n with $n > 3$ and moving to a retarded frame, written as

$$T = t - z/v_g = t - \beta_1 z, \tag{4.6}$$

where T represents the retarded time and v_g denotes the group velocity, the GNLSE is expressed as

$$\frac{\partial}{\partial z}A + \frac{\alpha}{2}A + \frac{i\beta_2}{2}\frac{\partial^2}{\partial T^2}A - \frac{\beta_3}{6}\frac{\partial^3}{\partial T^3}A = i\gamma_{NL}\left(|A|^2 A + \frac{i}{\omega_0}\frac{\partial}{\partial T}\left(|A|^2 A\right)\right), \tag{4.7}$$

where $A = A(z,t)$ is the envelope depending on time and the z-coordinate, α represents the attenuation constant, β_2 denotes the group velocity dispersion (GVD) parameter, β_3 characterizes the cubic dispersion and γ_{NL} stands for the nonlinear coefficient. The terms on the left-hand side of Equation (4.7) account for absorption and dispersion, while those on the right-hand side incorporate the Kerr effect (as discussed in Chapter 2.2.2). The term proportional to $\gamma_{NL}|A|^2$ describes SPM, while the term proportional to γ_{NL}/ω_0 is responsible for self-steepening. Naturally, the one dimensional approach omits self-focusing. Additionally, ionization and plasma effects are neglected.

1D split-step Fourier method

The split-step Fourier method is a pseudo-spectral numerical technique employed to solve nonlinear partial differential equations. Its name "split-step" reflects its approach of computing the solution in small steps, handling the linear and nonlinear components in separate operations. The term "Fourier" indicates that the field is alternately transformed between the time domain, where the linear step is computed, and the frequency domain, where the nonlinear step is computed.

To comprehend the mechanism underlying the split-step Fourier method, we express the GNLSE (Equation (4.7)) as

$$\frac{\partial}{\partial z}A = \left(\widehat{D} + \widehat{N}\right)A, \tag{4.8}$$

where $\widehat{D}$ denotes the linear differential operator that describes dispersion and loss, and $\widehat{N}$ represents the the nonlinear operator governing SPM and self-steepening.

These operators are given by

$$\widehat{D} = -\frac{\alpha}{2} + i\sum_{n=2}^{3} \frac{i^n \beta_n}{n!} \frac{\partial^n}{\partial T^n} = -\frac{i\beta_2}{2}\frac{\partial^2}{\partial T^2} + \frac{\beta_3}{6}\frac{\partial^3}{\partial T^3} - \frac{\alpha}{2}, \tag{4.9}$$

$$\widehat{N} = i\gamma_{NL}\left(|A|^2 + \frac{i}{\omega_0}\frac{1}{A}\frac{\partial}{\partial T}\left(|A|^2 A\right)\right). \tag{4.10}$$

For improved accuracy, higher orders of β ($n > 3$) may always be included in $\widehat{D}$, especially when dealing with shorter pulses.

In the following analysis, we assume that dispersive and nonlinear effects act independently during propagation over a small distance h. Thus, the propagation from a point z to $z + h$ can be performed in two steps. First, only the operator $\widehat{N}$ acts on A, and subsequently, only the operator $\widehat{D}$ acts on A. Assuming that $\widehat{D}$ and $\widehat{N}$ commute, one can write

$$A(z + h, T) = e^{h(\widehat{D}+\widehat{N})}A(z, T) \approx e^{h\widehat{D}}e^{h\widehat{N}}A(z, T). \tag{4.11}$$

The operator $e^{h\widehat{D}}$ is evaluated in the frequency domain, where $\frac{\partial}{\partial T}$ is replaced by $(-i\omega)$, simplifying calculations since $\widehat{D}(-i\omega)$ in Fourier space is merely a number. Utilizing the fast Fourier transform (FFT) algorithm makes the computation efficient, despite the necessity to switch back and forth between the time and the frequency domain. With the aid of the inverse fast Fourier transform (IFFT), the evaluation of the linear operator can be expressed as

$$e^{h\widehat{D}}A(z, T) = IFFT\left\{e^{h\widehat{D}(-i\omega)}FFT\left\{A(z, T)\right\}\right\}. \tag{4.12}$$

The dominant error term made by the assumption of commuting operators can be estimated using the Baker–Campbell–Hausdorff formula [59] to be $\frac{1}{2}h^2[\widehat{D}, \widehat{N}]$. Thus, the method is accurate to the second order in the step size h.

To enhance the accuracy of the method, a symmetrized scheme is employed, which is given by

$$A(z + h, T) \approx e^{\frac{h}{2}\widehat{D}}e^{h\widehat{N}}e^{\frac{h}{2}\widehat{D}}A(z, T). \tag{4.13}$$

In the symmetrized version, the leading error term is proportional to h^3, as the Baker–Campbell–Hausdorff formula needs to be applied twice for three consecutive operators.

To implement the split-step Fourier method, the fiber length is partitioned into small segments, which do not necessarily need to be equally spaced. For each segment h, the field $A(z,T)$ is propagated over a distance of $h/2$ using the FFT and IFFT algorithm as described in Equation (4.12). At the position $h/2$, the field is multiplied by a nonlinear term representing the effect of nonlinearity over the entire segment length h. Subsequently, the field is propagated over the remaining part of the segment $h/2$ considering only dispersion. The propagation scheme for one step is illustrated in Figure 4.1. In Section A.1 in the appendix, the key parts of the MATLAB code are presented to show the actual implementation.

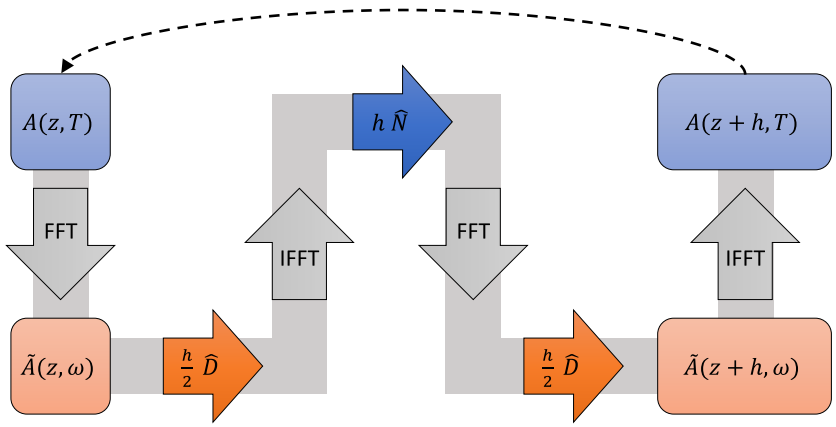

Figure 4.1.: Schematic depiction of one propagation step from z to $z+h$ employing the one dimensional symmetrized split-step Fourier method.

To model the propagation along the HCF in pressure gradient mode, the pressure distribution inside the capillary is described by [60]

$$p(z) = \sqrt{p_{in}^2 + \frac{z}{L}\left(p_{end}^2 - p_{in}^2\right)}, \tag{4.14}$$

where $p(z)$ denotes the pressure at distance z, p_{in} represents the pressure at the fiber entrance, L is the fiber length and p_{end} stands for the pressure at the exit side of the HCF.

The refractive index of the helium gas in the fiber core is computed using the dispersion formula [61]

$$n_{he} = \frac{c_1}{c_2 - \lambda_0^{-2}} + 1, \tag{4.15}$$

where n_{he} represents the refractive index of helium at atmospheric pressure, the first coefficient is given by $c_1 = 0.014755297$, the second coefficient is given by $c_2 = 426.2974$, and $\lambda_0 = 400\,\text{nm}$ denotes the central wavelength.

The nonlinear refractive index of helium at atmospheric pressure is estimated to be $n_2 = 0.41 \times 10^{-24}\ \text{m}^2/\text{W}$ [62].

We will now discuss one specific simulation, which closely mirrors experimental conditions. The numeric grid chosen for this simulation consists of 1000 equally spaced propagation steps, each corresponding to 5 mm. In the time and the frequency domain, we employ $N = 2^{11} = 2048$ steps. The simulation spans a time interval of 900 fs, while the considered frequency range extends up to 3×10^{15} Hz. In Figure 4.2, the temporal and spectral characteristics of the input and output pulse are shown. The asymmetry observed in the temporal shape and the spectral distribution illustrates the impact of self-steepening. When comparing the spectral results with experimental data, we observe a generally strong agreement, despite some variations in shape around the central wavelength and at the shorter wavelength side.

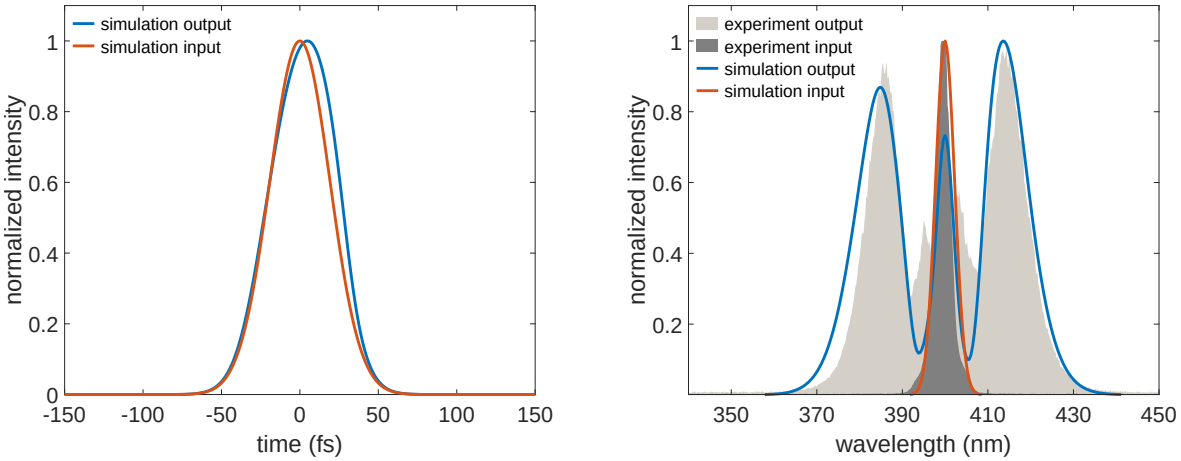

Figure 4.2.: Temporal (left) and spectral distribution (right) of the input and output pulse simulated with the 1D split-step Fourier method. The conditions chosen are close to the experiment: 5 m propagation length, 250 µm fiber inner radius, pressure gradient between 0 and 1.5 bar helium, 400 nm initial central wavelength, 1.2 mJ input pulse energy, 45 fs FWHM input pulse duration, Fourier limited Gaussian input in time and frequency space. The spectral distribution is compared to experimental data.

Naturally, the ideal condition of a Fourier limited Gaussian input pulse is hard to achieve in real-world scenarios. Simulations indicate that the shape of the output spectrum is heavily influenced by the input dispersion of the 400 nm pulses. Since this dispersion cannot be independently tuned but is directly linked to the energy of the 400 nm pulses (see Chapter 3.1), we will numerically investigate how dispersion influences the spectral distributions to gain a qualitative understanding of its impact.

Figure 4.3 illustrates how input GDD affects the output spectra, while Figure 4.4 demonstrates the influence of input TOD. The greater the magnitude of the additional input GDD or TOD is, the narrower the spectral width of the output becomes. Additionally, the sign of the TOD strongly influences the shape of the spectral distribution.

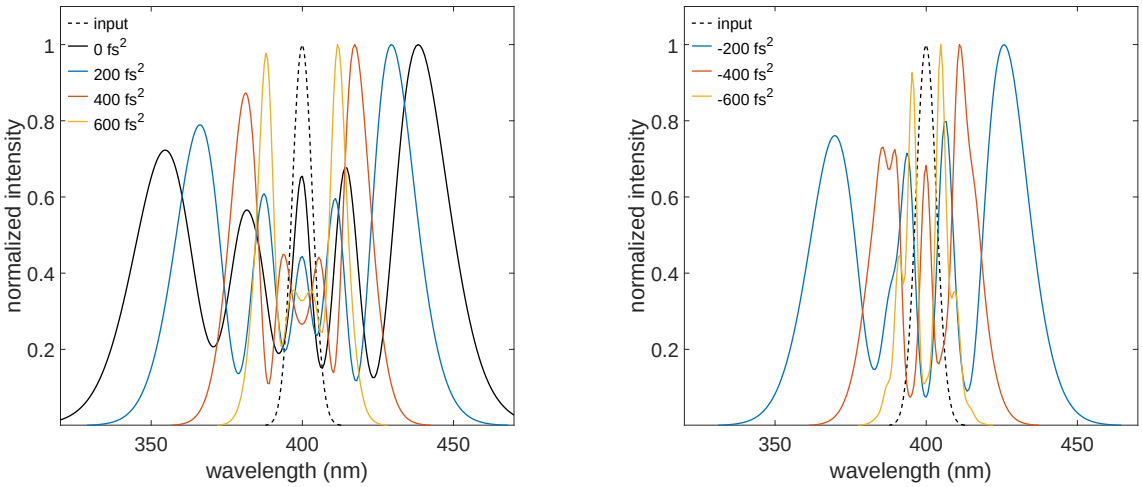

Figure 4.3.: Output spectra for Gaussian pulses with different input GDD. The input spectrum for all cases is the dashed black curve. The parameters of the simulation are as follows: 5 m fiber length, 250 µm fiber inner radius, pressure gradient between 0 and 1.5 bar helium, 30 fs FWHM Fourier limited Gaussian input, 1.5 mJ pulse energy.

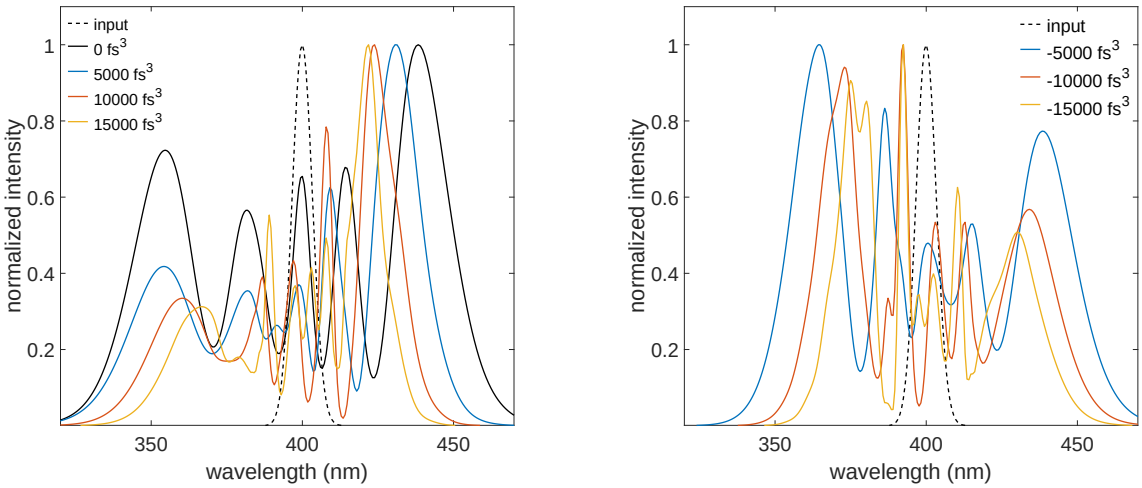

Figure 4.4.: Output spectra for Gaussian pulses with different input TOD. The input spectrum for all cases is the dashed black curve. The parameters of the simulation are the same as in Figure 4.3.

2D split-step Fourier method

To extend the method beyond one-dimensional propagation of the fundamental mode while maintaining reasonable computational effort, the spatial beam profile is decomposed into radially symmetric EH modes. Since radial symmetry is assumed, this approach is only two-dimensional, thus saving computation time compared to full three-dimensional propagation. The intensity profile of the relevant modes exhibit a Bessel-like shape, making a straightforward approach to this problem a Fourier-Bessel series for finite intervals [63].

We restrict ourselves to EH_{nm} with $n = 1$ and $m > 0$ (see Chapter 2.3.1), leading to

$$\tilde{A}(z, r, \omega) = \sum_{m=1}^{\infty} c_m \mathrm{EH}_{1m}(z, r, \omega), \tag{4.16}$$

where EH_{1m} represents the field distribution for the m-th mode and c_m denotes the corresponding coefficient. The distribution EH_{1m} is given by

$$\mathrm{EH}_{1m} = J_0\left(\frac{u_{1m} r}{a}\right), \tag{4.17}$$

where J_0 is the Bessel function of the first kind with index zero, u_{nm} denotes the m-th zero of the Bessel function J_{n-1}, r is the radial coordinate, and a represents the inner radius of the HCF. The coefficients c_m are obtained using the following relation [63]

$$c_m = \frac{2}{a^2 J_1(u_{1m})^2} \int_0^a r\tilde{A}(r)\ \mathrm{EH}_{1m} dr. \tag{4.18}$$

The modes are individually propagated for the dispersion (half) step and then re-composed for the nonlinear step. This process is illustrated in the propagation scheme of our two-dimensional model in Figure 4.5. The dashed gray arrow indicates the procedure of one complete propagation step after another as described in Equation (4.13). The dashed black arrow represents a computationally more efficient procedure, which skips the last IFFT and first FFT operations, along with one modal re- and decomposition for all propagation steps except for the first and last ones.

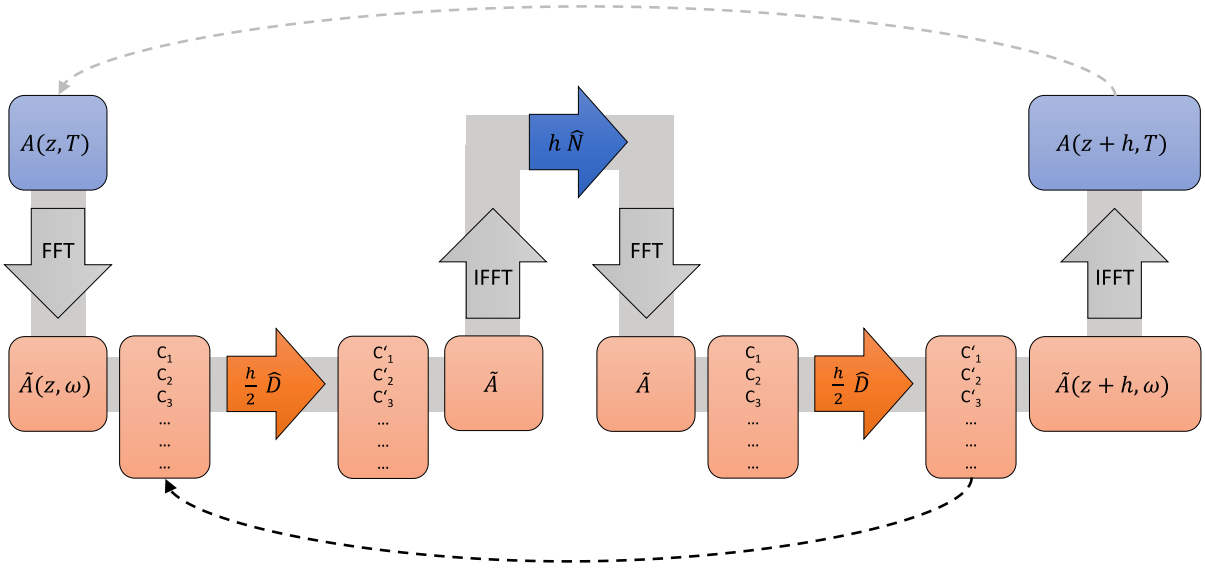

Figure 4.5.: Schematic depiction of one propagation step from z to $z + h$ employing the two-dimensional symmetrized split-step Fourier method. The gray arrow shows one complete propagation step, whereas the black arrow indicates a computationally more efficient procedure.

Ionization effects

To incorporate ionization effects into the simulations, the Perelomov-Popov-Terent'ev (PPT) model [64–66] is choosen to determine ionization rates. The model improves the formalism introduced by Keldysh for non-relativistic ionization rates of hydrogen-like atoms in strong laser fields [67] by considering Coulomb interaction at larger inter-nuclear distances. In the quasi-static limit, the PPT model converges to the well known Ammosov-Delone-Krainov (ADK) model [68].

According to Keldysh theory, there are two regimes of ionization: tunnel ionization and multiphoton ionization. The dominant mechanism may be determined by the Keldysh parameter γ, given by

$$\gamma = \sqrt{\frac{IP}{2U_p}}, \tag{4.19}$$

where IP denotes the ionization potential of the atom and U_p represents the ponderomotive potential. U_p is calculated as

$$U_p = \frac{e^2 E^2}{4 m_e \omega^2}, \tag{4.20}$$

where e is the elemental charge, E denotes the electric field strength, m_e is the electron mass and ω represents the angular frequency of the light. For $\gamma \ll 1$, only tunneling ionization occurs, whereas for $\gamma \gg 1$, multiphoton ionization dominates.

The advantage of the PPT model lies in its ability to accurately predict ionization rates not only within the tunnel ionization range, where the ADK model would suffice, but also in the intermediate regime of $\gamma \approx 1$ in case of noble gases [69].

We compute the ionization rate w following the methodology outlined in [70] (the subsequent calculations are in atomic units)

$$w = Q \cdot w_{SR}, \tag{4.21}$$

where Q characterizes the Coulomb correction and w_{SR} represents the ionization rate for a system bound by a short-range potential. The Coulomb correction Q is approximated by

$$Q \approxeq \left(\frac{2}{F}\right)^{2n^*} (1 + 2e^{-1}\gamma)^{-2n^*}, \tag{4.22}$$

where $F = E/(2\ IP)^{3/2}$ represents the reduced electric field, and $n^* = \mathcal{Z}/\sqrt{2\ IP}$ is the effective principal quantum number of the bound state. This value is determined by the charge number of the atomic core $\mathcal{Z}$ and the ionization potential of the atom IP.

The ionization rate w_{SR} is given by

$$w_{SR} = \frac{2C^2}{\pi}\, IP\, K_0^{-3/2}\beta^{1/2} \sum_{n>n_{th}} \mathcal{F}\left(\sqrt{\beta(n-n_{th})}\right) e^{-\frac{2g(\gamma)}{3F}-2c_1(n-n_{th})}, \tag{4.23}$$

where several terms require further explanation: C denotes the asymptotic coefficient of the bound state wave function, determined by $C^2 = 2^{2n^*-2}/(n^*!)^2$, employing Hartree's approximation [71] for s-states. K_0 compares the ionization potential to the photon energy and is given by $K_0 = IP/\hbar\omega$. The parameter β is defined as $\beta = 2\gamma/\sqrt{1+\gamma^2}$. $\mathcal{F}(...)$ denotes the Dawson integral [72]. n_{th} represents the ionization threshold, given by $n_{th} = K_0(1 + 1/(2\gamma^2))$. Finally, $g(\gamma)$ and c_1 are defined as

$$g(\gamma) = \frac{3}{2\gamma}\left[\left(1+\frac{1}{2\gamma^2}\right)\operatorname{arcsinh}(\gamma) - \frac{\sqrt{1+\gamma^2}}{2\gamma}\right], \tag{4.24}$$

$$c_1 = \operatorname{arcsinh}(\gamma) - \frac{\gamma}{\sqrt{1+\gamma^2}}. \tag{4.25}$$

Given an ionization rate w (Equation (4.21)) dependent on an electric field $E(r,t)$, the ionization probability P of one atom being ionized can be calculated as follows [73]

$$P(r,t) = \left(1 - e^{-\int_{-\infty}^{t} w(E(r,t'))dt'}\right). \tag{4.26}$$

The density of free electrons n_e created by ionization is determined by multiplying the ionization probability with the particle density n_0

$$n_e(r,t) = n_0 P(r,t). \tag{4.27}$$

Since evaluating the integral in Equation (4.26) contributes significantly to the overall computational effort and needs to be performed independently for each radial coordinate r in our numeric grid, we exploit MATLAB's built-in option for parallel computing via a "parfor" loop, considerably reducing the computation time. Naturally, this approach strongly depends on the capabilities of the machine being used.

To incorporate ionization effects into the simulations, the nonlinear operator $\widehat{N}$ (Equation (4.10)) in the GNLSE may be expanded to include an additional term [74]

$$\widehat{N} = i\gamma_{NL}\left(|A|^2 + \frac{i}{\omega_0}\frac{1}{A}\frac{\partial}{\partial T}\left(|A|^2 A\right)\right) - \frac{i\omega_p^2}{2\omega_0 c}, \tag{4.28}$$

where c denotes the speed of light.

The plasma frequency ω_p is calculated from the density of free electrons n_e (Equation (4.27))

$$\omega_p = \sqrt{\frac{e^2 n_e}{m_e \epsilon_0}}, \tag{4.29}$$

where e denotes the elementary charge, m_e represents the (effective) electron mass, and ϵ_0 is the vacuum permittivity.

The introduction of the new term in the nonlinear operator $\widehat{N}$ (Equation (4.28)), which depends on ω_p, induces a frequency shift, known as the plasma blue shift. Additionally, an extra loss term is linked to ionization. However, since we work at low electron densities, we neglect the additional absorption.

In Figure 4.6, the temporal and spectral field envelopes of an exemplary 2D simulation are illustrated. The top row displays the input pulse, while the subsequent three rows show the simulated output pulse for an increasing number of implemented nonlinear effects. Initially, only dispersion is considered with dispersion terms β_n (see Equation (4.5)) computed up to the sixth order for both waveguide dispersion and dispersion in the gas. Subsequently, the Kerr effect is incorporated into the simulation, resulting in spectral broadening due to SPM and self-steepening of the pulse in time. Finally, the correction term for ionization is introduced to the nonlinear operator as described in Equation (4.28). Here, the spectral distribution exhibits a slight shift towards higher frequencies compared to the results obtained previously.

Since the plasma blue shift is not readily apparent in Figure 4.6, the difference between the spectral distribution with and without ionization is depicted in Figure 4.7. There, the shift towards higher frequencies becomes evident.

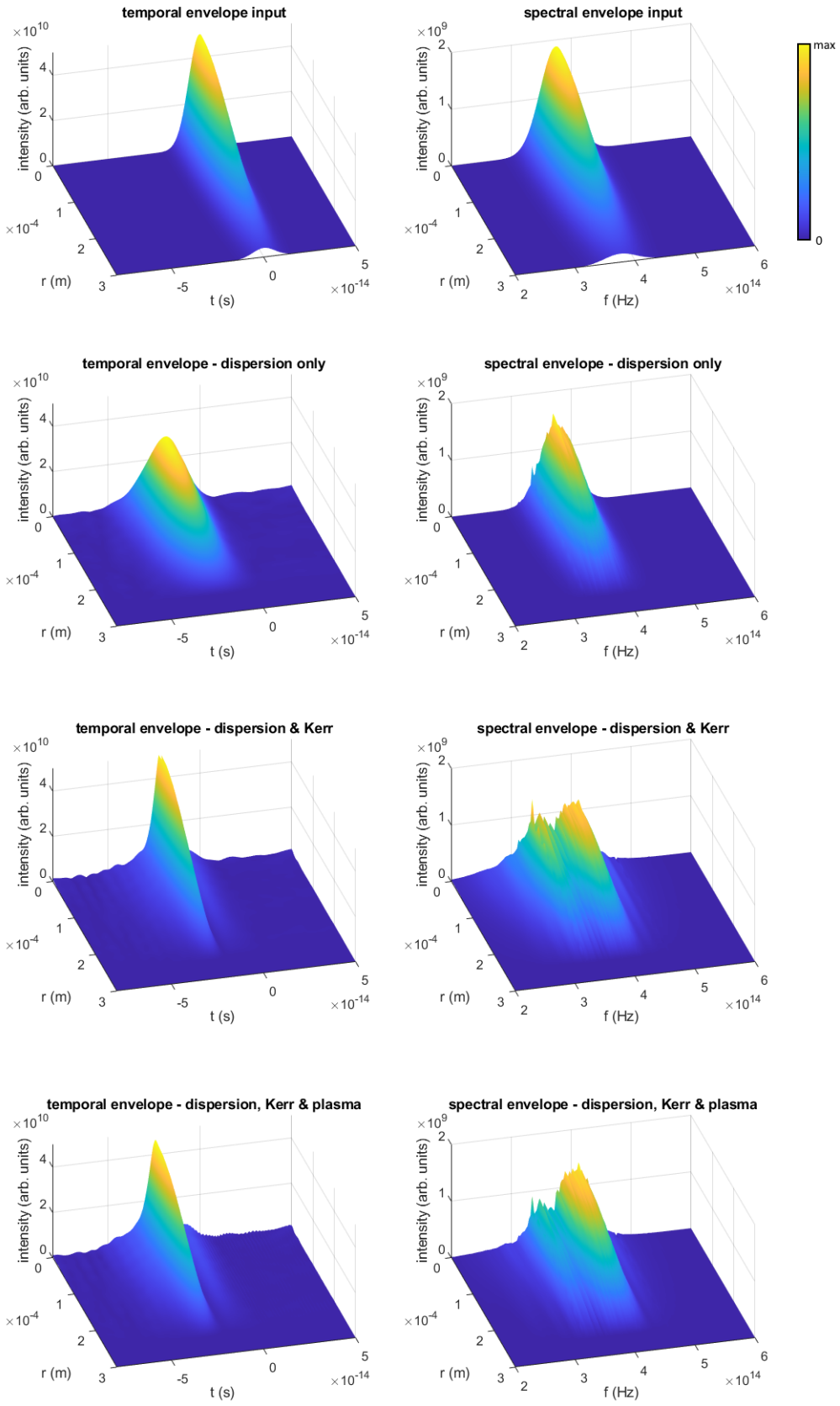

Figure 4.6.: 2D simulation results with increasing number of effects included. Input parameters: 10 fs FWHM pulse duration, 1 mJ pulse energy, 800 nm central wavelength, 1 bar helium, 3 m propagation length, 250 µm fiber inner radius, 1000 propagation steps, 100 grid points in radial direction.

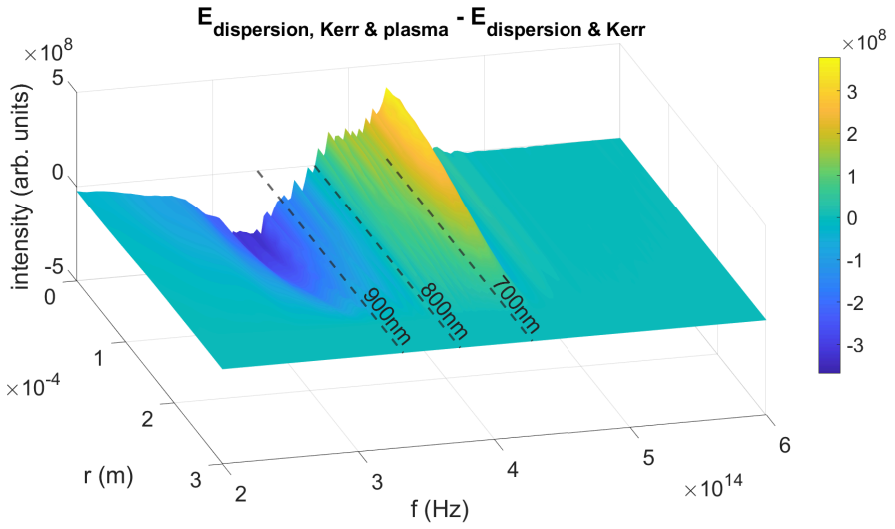

Figure 4.7.: Difference between the simulated spectra from Figure 4.6 with and without ionization (fourth minus third row).

4.1.2. Unidirectional pulse propagation equation

We compare our simulation results, acquired through the solution of the GNLSE with the split-step Fourier method outlined earlier, to a more rigorous approach provided by Luna.jl [57], a versatile tool for simulating nonlinear optical dynamics. The software offers a choice between the z-propagated UPPE and the GNLSE, along with options for single-mode (mode-averaged) or multi-mode propagation in waveguides, as well as full (3+1)D propagation in free space.

Since the unidirectional pulse propagation approach does not rely on the slowly varying envelope approximation, it remains valid for shorter pulses, where the absolute phase between envelope and carrier holds significance. The key approximation lies in assuming that the back-reflected field is weak and can be disregarded for computing the nonlinear response of the medium [75]. Consequently, the nonlinear response itself must be a small perturbation to the linear response. Additionally, when the z-component of the field and response are significantly smaller than the transverse components, a scalar form of the z-propagated UPPE for non-magnetic homogeneous media may be retrieved.

The equation is given by [76]

$$\frac{\partial}{\partial z}E_{k_x,k_y}(\omega,z) = ik_z E_{k_x,k_y}(\omega,z) + \frac{i\omega^2}{2\epsilon_0 c^2 k_z}P_{k_x,k_y}(\omega,z) - \frac{\omega}{2\epsilon_0 c^2 k_z}j_{k_x,k_y}(\omega,z), \quad (4.30)$$

where E_{k_x,k_y} is the transverse field, ω denotes the angular frequency of the light, P_{k_x,k_y} represents the transverse nonlinear polarization, j_{k_x,k_y} is the transverse current density and k_z denotes the z-component of the wave vector given by

$$k_z = \sqrt{\frac{\omega^2\epsilon(\omega)}{c^2} - k_x^2 - k_y^2}, \quad (4.31)$$

where $\epsilon(\omega)$ is the relative permittivity.

Effects that can be incorporated into the numerical model of Luna.jl when solving the UPPE include modal dispersion and loss in waveguides, the optical Kerr effect, Raman scattering in molecular gases or glasses (not relevant in this case, since we study noble gases only), photoionization and plasma dynamics [57]. For photoionization, two models are implemented, which were already mentioned above in Chapter 4.1.1: ADK and PPT.

In the subsequent analysis, the basic propagation example illustrated previously in Figure 4.2 is compared to UPPE simulations conducted using Luna.jl. Figure 4.8 presents the same simulation outcomes as depicted in Figure 4.2, although without normalization. Furthermore, the spectrum is visualized on a logarithmic scale to enhance comparability. In Figure 4.9, results obtained by an equivalent simulation using Luna.jl to solve the UPPE are depicted.

The outcomes derived from the simple 1D split-step Fourier approach addressing the GNLSE, and those obtained through solving the UPPE exhibit nearly perfect agreement. A marginal discrepancy can be found in the shape of the trailing edge of the temporal distribution and in the short wavelength region (close to 350 nm) in the spectral distribution. However, the variation in wavelength is only visible on a logarithmic scale, given the minimal energy in this spectral range.

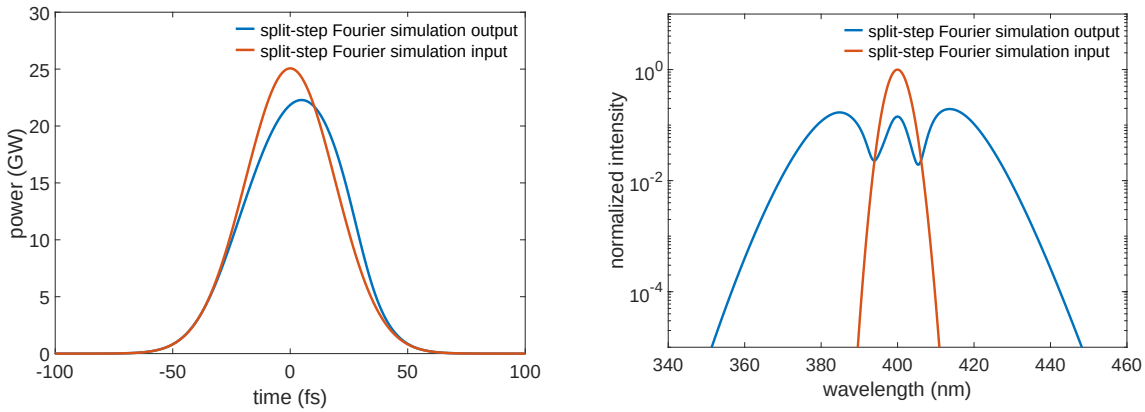

Figure 4.8.: Simulation results from Figure 4.2. Temporal pulse shape on the left and spectral distribution on the right. The spectrum is plotted on a logarithmic scale.

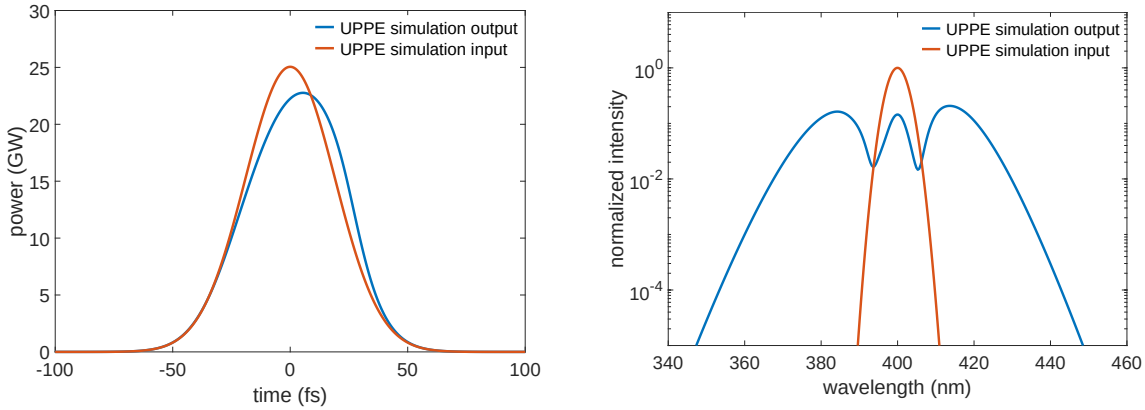

Figure 4.9.: Simulation results obtained by Luna.jl for the same initial conditions as in Figure 4.8. Temporal pulse shape on the left and spectral distribution on the right. The spectrum is plotted on a logarithmic scale.

Generally, the 1D split-step Fourier method, the 2D split-step Fourier method, and solving the UPPE yield nearly identical spectra under conditions close to our experimental parameters, where an input pulse energy of up to 1.5 mJ, a fiber inner radius of 250 µm, and up to 1.5 bar helium in the fiber are assumed. The primary uncertainty lies in the precise shape of the input pulse in the time and the frequency domain, which significantly impacts spectral broadening.

At higher peak powers, the effects of self-focusing, higher-order waveguide modes, and ionization-induced frequency shifts become significant and must be taken into account. However, we aim to avoid this regime, since losses induced by the long propagation length increase with the order of the waveguide mode (see Chapter 2.3.1), and the setup following the HCF is optimized for the beam size and divergence of the fundamental EH_{11} mode. Nevertheless, it is crucial to perform simulations that include these effects to determine in which regime we are operating.

4.2. Third-harmonic generation in gas

To simulate THG in noble gases within the configurations described in Chapter 3.5, the nonlinear pulse propagation provided by Luna.jl [57] is adapted. The key parts of the implementation can be found in Section A.2 in the appendix. Radially symmetric free space propagation is chosen to mitigate computational complexity compared to a full 3D approach. Given the assumption of a perfect Gaussian input pulse in both time and space, together with a homogeneous nonlinear medium, radial symmetry is a valid assumption.

The pressure distribution along the propagation direction is modeled to be either constant or a gradient, following the description provided in Equation (4.14). In the case of the pulsed nozzle, where the gas input is situated at the center of the gas cell, two gradient distributions are defined for the two halves of the cell and merged at the center. The position of the focus within the gas cell can be adjusted freely by varying the curvature of the input wavefront, achieved by specifying a distance from the (virtual) beam waist to the Gaussian input field. Furthermore, the wavelength range and time interval considered are adaptable, as are the initial and maximum step sizes in propagation direction. During propagation, the step size is dynamically adjusted to minimize computation time while ensuring that the computational error remains below a predefined threshold.

In the nonlinear response term, third-order effects are included. Additionally, the PPT ionization rate (see Chapter 4.1.1) is computed to construct the plasma polarization response.

A serious limitation of the accuracy of the THG simulations is the definition of refractive indices in the nonlinear pulse propagation implemented in Luna.jl. These indices are determined using Sellmeier equations for noble gases, primarily derived from data in the visible or infrared range. For instance, the relation used for xenon is only applicable down to 400 nm [77], while the one for helium is valid down to 90 nm [78]. Given that many gases exhibit resonances in the VUV range, careful consideration of the refractive index model is necessary.

For an exemplary simulation optimized for high conversion efficiency in helium, the input parameters are as follows: 0.5 mJ pulse energy, 10 fs FWHM pulse duration (Fourier limited Gaussian), maximum pressure of 1.5 bar helium in the center of the 1 cm long gas cell with a pressure gradient towards vacuum on both sides, 70 µm (virtual) minimal waist and the (virtual) focus position of the fundamental beam is precisely at the end of the cell. However, due to plasma defocusing, the most intense UV beam profile is located directly at the input side.

Figure 4.10 depicts the radial intensity distribution for the 400 nm and 133 nm radiation along the propagation. Figure 4.11 presents the corresponding integrated VUV pulse energy depending on the propagation distance on the left and a polar plot of the spatial distribution of the generated VUV pulse on the right. The resulting pulse energy slightly exceeds 3 µJ, leading to a conversion efficiency of more than 6×10^{-3}.

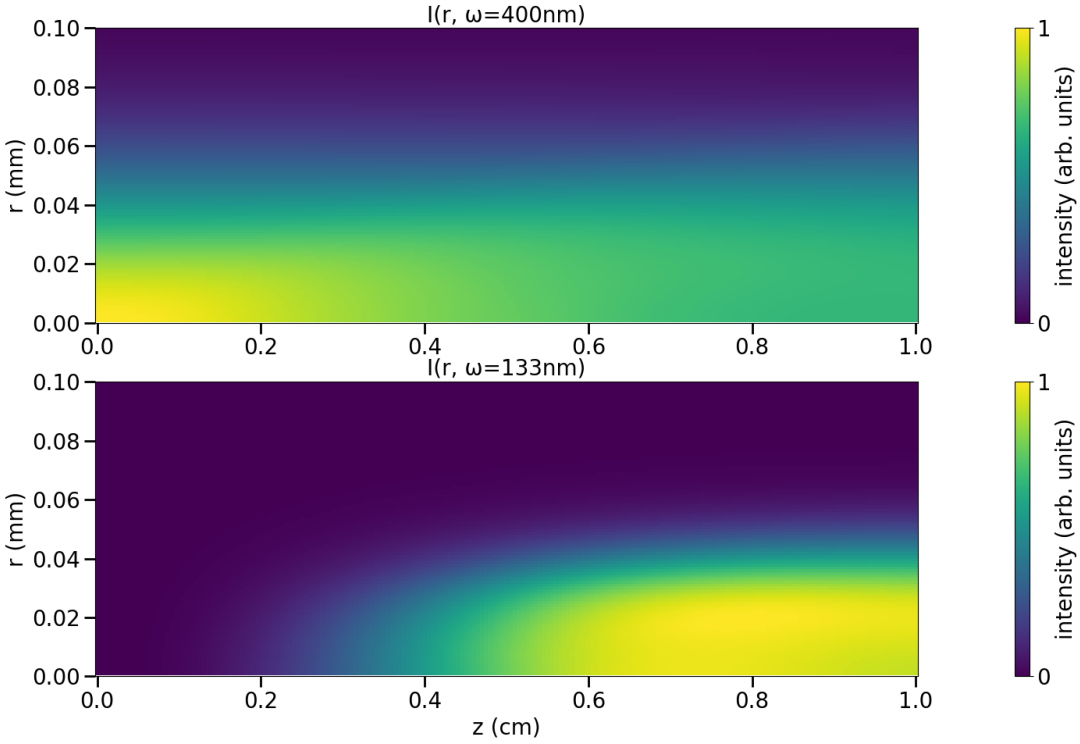

Figure 4.10.: Simulated radial intensity distribution of the fundamental and third-harmonic beam along the propagation for 1.5 bar of helium.

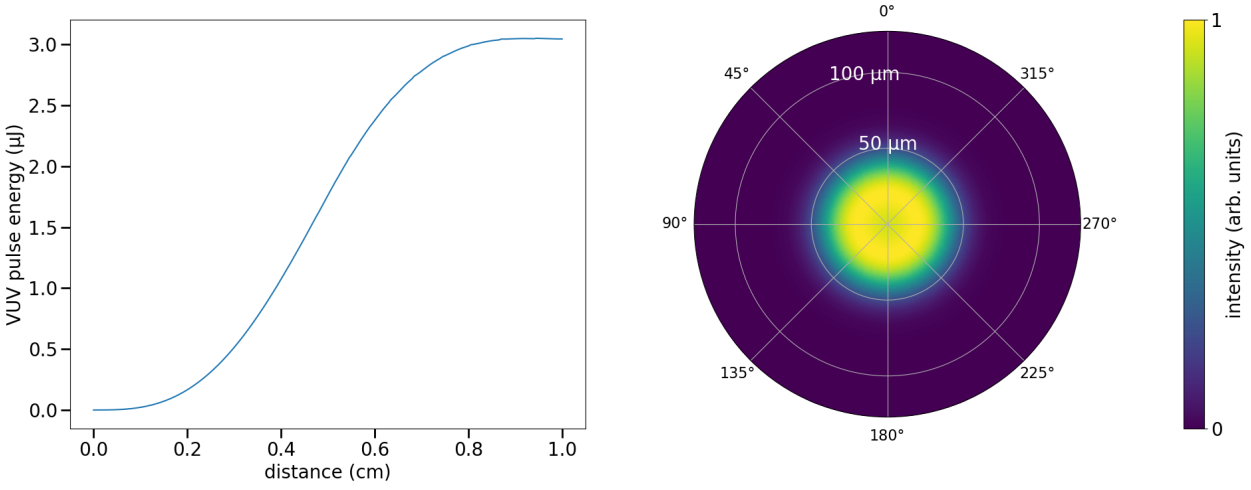

Figure 4.11.: Left: integrated VUV pulse energy, right: polar plot of the VUV spatial profile for 1.5 bar of helium.

When we maintain the same initial conditions but double the maximum pressure (Figure 4.12 and 4.13), we observe that the conversion efficiency decreases. The VUV energy subsides in the second half of the propagation, and the spatial distribution of the generated harmonic pulse exhibits a ring shape with a central minimum, which is generally not preferable for further use of the VUV pulses.

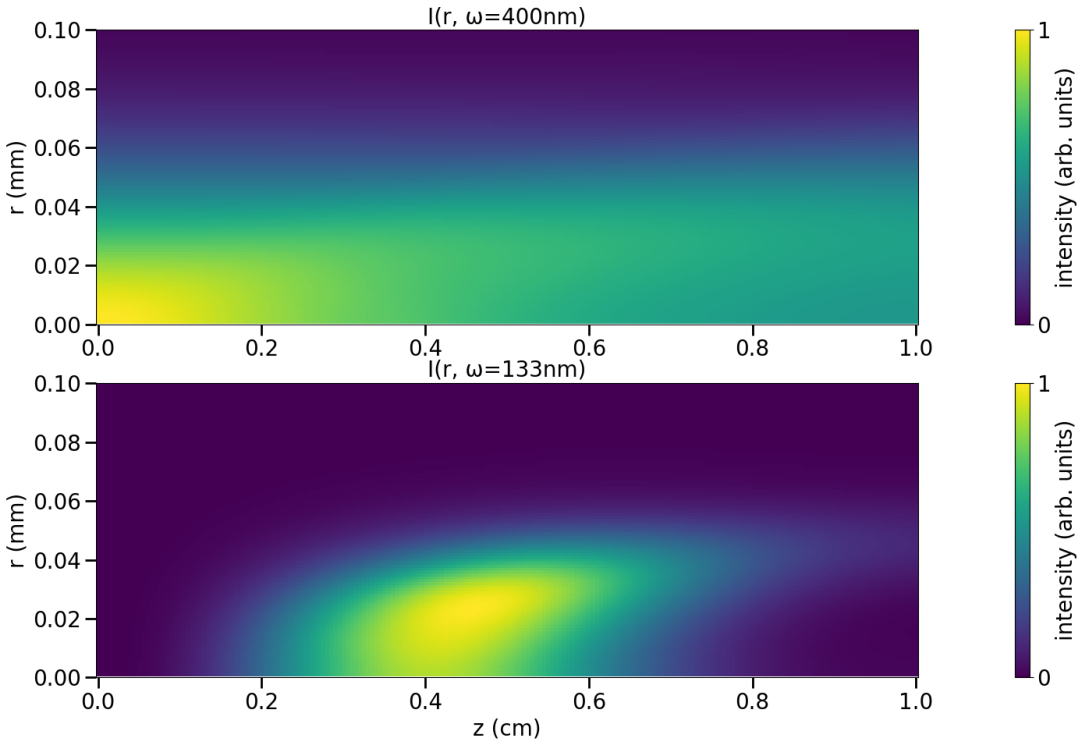

Figure 4.12.: Simulated radial intensity distribution of the fundamental and third-harmonic beam along the propagation for 3 bar of helium.

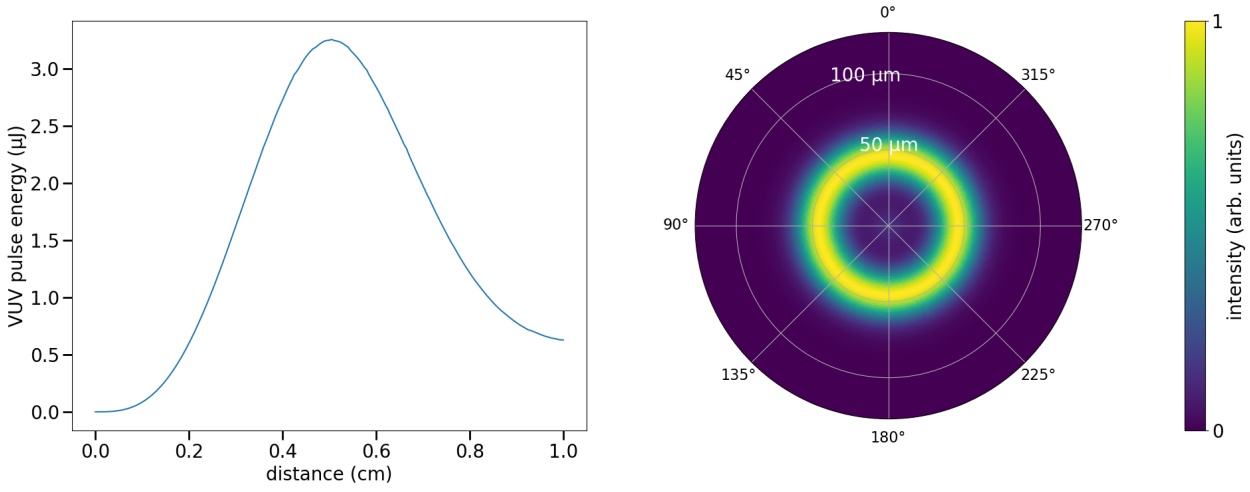

Figure 4.13.: Left: integrated VUV pulse energy, right: polar plot of the VUV spatial profile for 3 bar of helium.

To illustrate the effect of phase mismatch, we investigate a scenario with lower pressure (0.75 bar) that remains constant over a relatively long propagation distance of 15 cm. The minimal waist is increased to 150 µm and the focus position is shifted to the center of the medium to ensure nonlinear interaction over the full simulation length. Figures 4.14 and 4.15 depict the simulation results analogous to Figures 4.10 - 4.13. The oscillations in the VUV energy are a clear indication of phase mismatch.

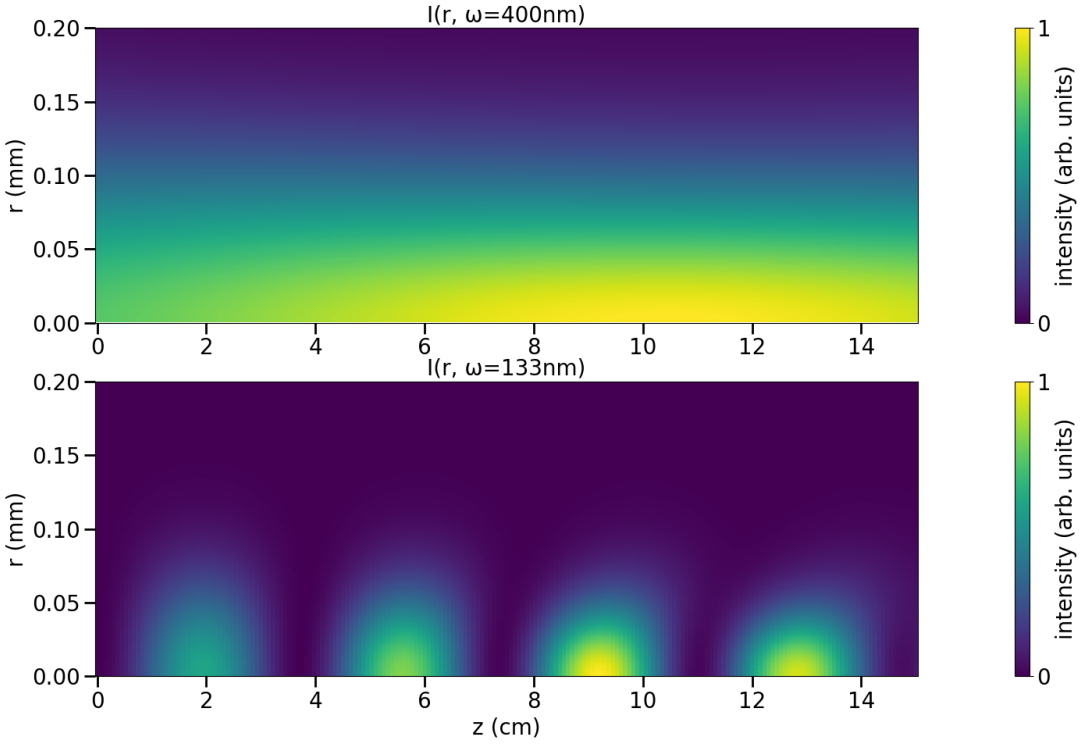

Figure 4.14.: Simulated radial intensity distribution of the fundamental and third-harmonic beam for 0.75 bar of helium and 15 cm propagation length.

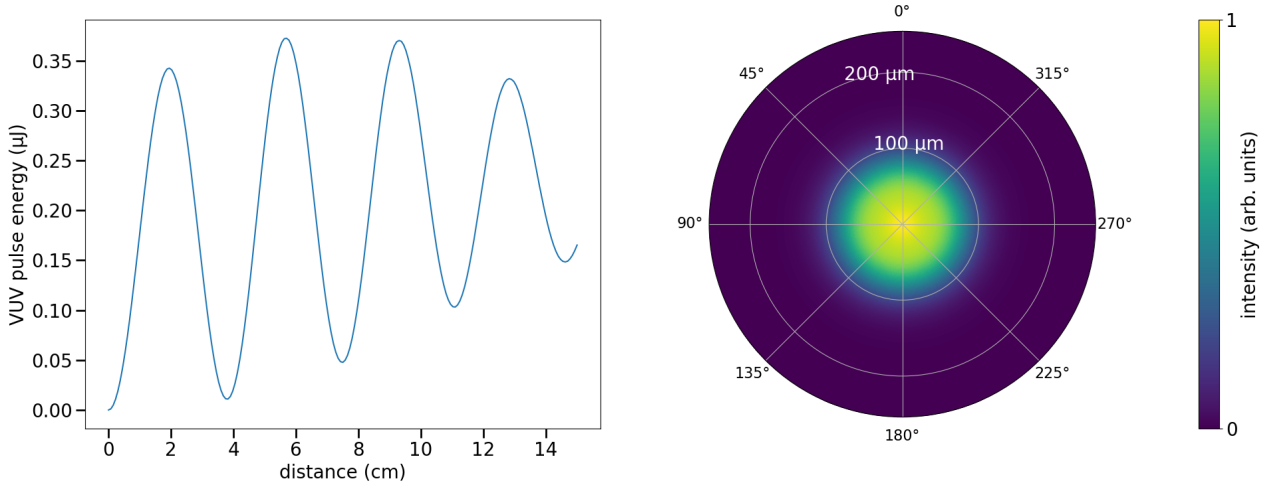

Figure 4.15.: Left: integrated VUV pulse energy, right: polar plot of the VUV spatial profile for 0.75 bar of helium and 15 cm propagation length.

The THG simulations demonstrate the critical importance of optimizing the interplay between medium length, pressure, and pulse peak power. Although direct simulation of the gases used in the experiments described in Chapter 6 is not feasible, the general behaviour can be analyzed. The ring shape observed in Figure 4.13 resembles the beam profile reported by Trabs et al. [27], who attribute it to six-wave mixing processes. In our context, plasma formation due to increased medium density may also contribute to absorption and defocusing of the VUV beam, since there is a pronounced maximum in VUV energy at approximately half the propagation length.

In general, conversion efficiency is maximized with shorter medium lengths, when paired with higher pressure and matched peak power. Consequently, when there is flexibility in selecting other parameters, a shorter cell appears to be preferable to a longer one.

4.3. Dispersion manipulation in a 4f setup

In Chapter 3.4, the 4f setup for dispersion compensation after the HCF is introduced. Simulations of the spectral phase, depending on the exact geometry of the setup, are conducted using *Wolfram Mathematica* with the optical design package *Optica EM*. The code was originally developed by Armin Azima. Only minor adjustments are made to implement the retro-reflector and adjust the dimensions and angles accordingly, since the original version of the code featured just one plane mirror for back-reflection. In Section A.3 in the appendix, parts of the *Mathematica* notebook containing the calculations are presented.

The optical path length, which varies with wavelength, is determined by ray tracing a so-called "rainbow of rays" spanning from 370 to 430 nm and then interpolating the results. Figure 4.16 illustrates the ray tracing geometry involving the grating, lens, and retro-reflector. Note that the grating is not rotated with respect to the lens as an artifact of the way the grating is implemented in *Optica EM*. In the experiment, the rotation of the grating ensures maximum diffraction efficiency as described in Chapter 3.4. Due to the inherent conflict between ray tracing and the wave-optics nature of diffraction at a grating, *Optica EM* simplifies the process by defining the rays to be entirely directed to the desired order, calculating the diffraction angle based on the ray's wavelength.

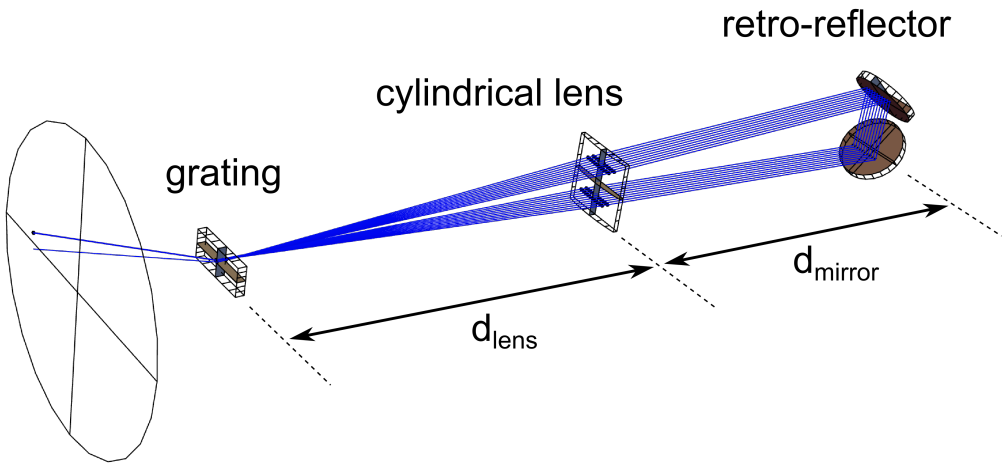

Figure 4.16.: Ray tracing geometry. The distance between grating and lens is denoted d_{lens}, the distance between lens and the mirrors of the retro-reflector is denoted d_{mirror}.

From the differences in optical path length, it is straightforward to calculate the relative phase and its derivatives. Figure 4.17 shows the phase, group delay, GDD and TOD for a scenario, where the properties remain unchanged for the central wavelength, which is 400 nm, corresponding to an angular frequency of 4700 rad/ps.

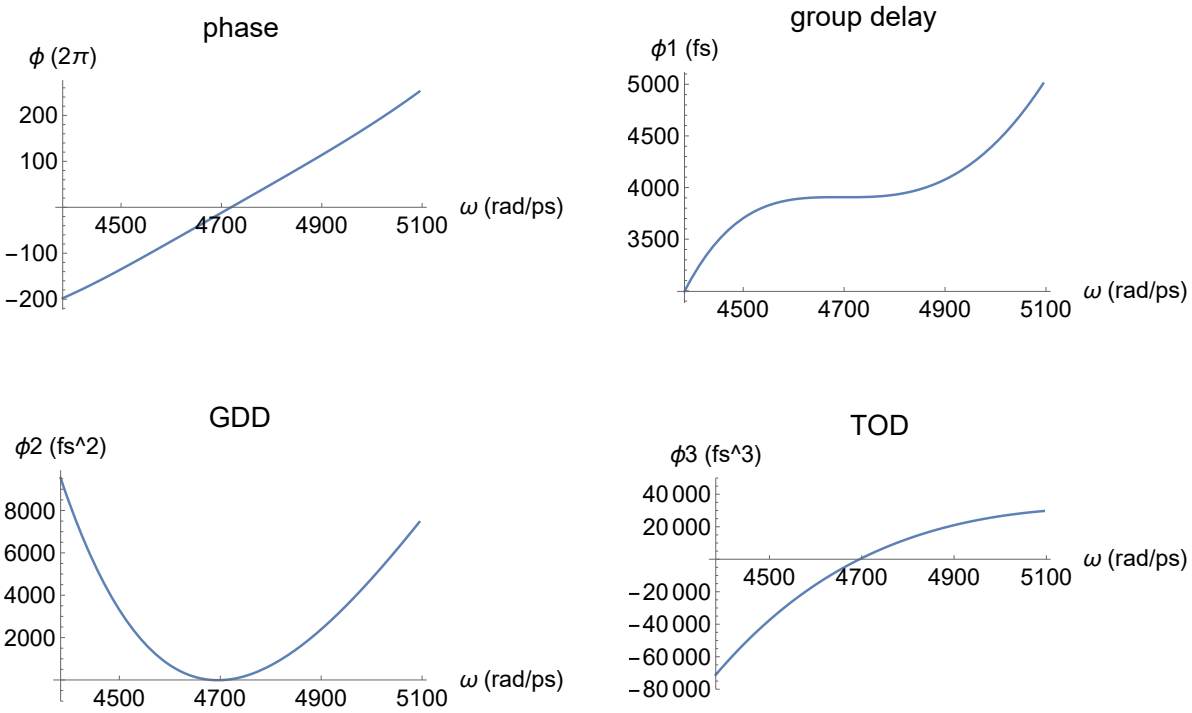

Figure 4.17.: Phase, group delay, GDD and TOD depending on the angular frequency ω. The curves are derived from the optical path length. A frequency of 4700 rad/ps corresponds to the central wavelength of 400 nm.

4.3.1. Shifting the lens

To compensate for the dispersion accumulated in the HCF, GDD values on the order of hundreds of femtoseconds squared are required. This can be achieved by adjusting the position of the cylindrical lens relative to the grating. Figure 4.18 illustrates one exemplary case where the lens is shifted 5 mm away from the grating compared to the situation shown in Figure 4.17.

Evaluating the GDD at 400 nm, one obtains nearly 0 fs^2 in Figure 4.17 (10 fs^2 to be precise) and 2218 fs^2 in Figure 4.18. This shift is observed analogously for shorter distances between the lens and the grating, only the sign of the GDD changes. Figure 4.19 displays values for a shift of ± 10 mm relative to the conditions in Figure 4.17. From the linear behavior of the GDD with respect to the lens position, one can extract a slope of 441 fs^2/mm.

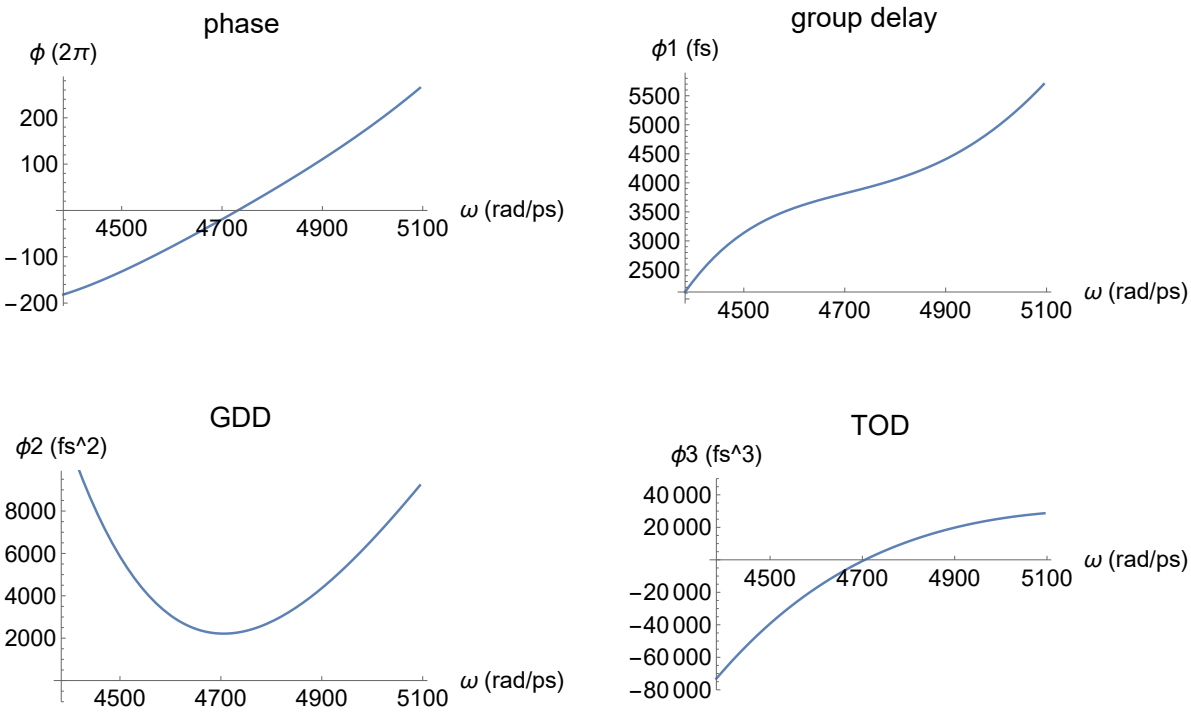

Figure 4.18.: Shifting the cylindrical lens 5 mm: phase, group delay, GDD and TOD depending on the angular frequency ω.

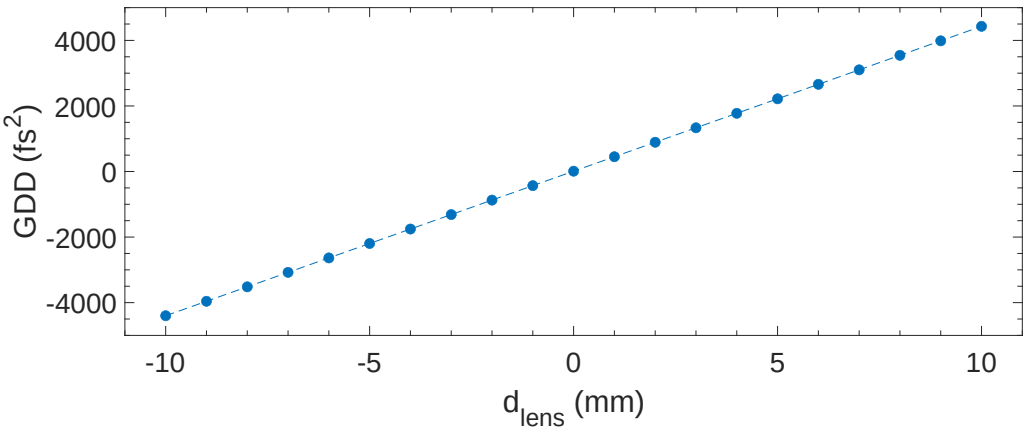

Figure 4.19.: GDD depending the lens position for the central wavelength of 400 nm. The position d_{lens} is given relative to the lens position in Figure 4.17.

4.3.2. Rotating the lens

Another factor influencing dispersion is the rotation of the cylindrical lens. Figure 4.20 depicts the result of 5° rotation with respect to the conditions in Figure 4.17. The most prominent change is the position of the minimum in GDD and thus zero TOD. Consequently, this may be exploited to adjust the TOD at the central wavelength. Figure 4.21 illustrates the numerically retrieved TOD for lens rotations of up to 20°. Of course, there are limitations regarding large rotations in the experiment, since this would affect the beam quality after the 4f setup.

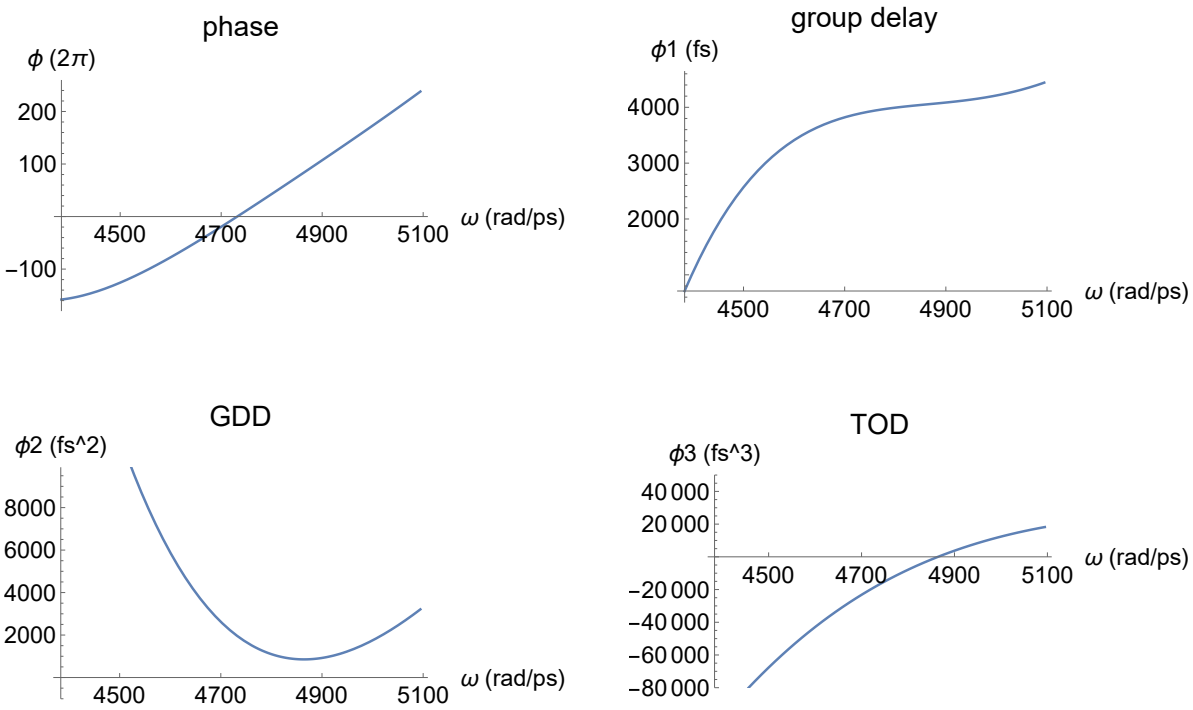

Figure 4.20.: Rotating the cylindrical lens by 5°: phase, group delay, GDD and TOD depending on the angular frequency ω.

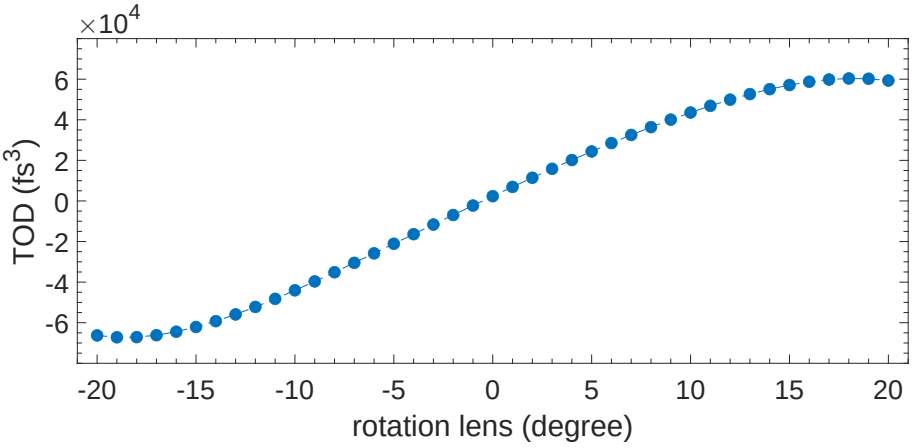

Figure 4.21.: TOD depending the lens rotation for the central wavelength of 400 nm. The rotation is given relative to the situation in Figure 4.17.

To optimize the focus quality behind the 4f setup, there is one additional degree of freedom: the tilt of the lens. Naturally, this is not completely independent from the system's dispersion, but the effect is rather small. The main contribution is an increase in GDD due to longer propagation in the lens material (fused silica), which, in turn, may be compensated by shifting the lens position.

5. UV pulse characterization

This chapter focuses on the generated UV pulses that are spectrally broadened by SPM in a helium-filled HCF and subsequently temporally compressed using a 4f setup for dispersion manipulation.

The pulses are centered around 400 nm, resulting from SHG of 800 nm light. Given that the pulse length of the NIR is 30 fs FWHM and the second-harmonic intensity is proportional to the square of the fundamental intensity, the shortest expected pulse duration for Gaussian pulse shapes generated by the BBO crystal, without any dispersion or distortion and perfect phase-matching for all spectral components, would be $30\,\mathrm{fs}/\sqrt{2} \approx 21.2\,\mathrm{fs}$.

However, this ideal scenario is not achieved due to limitations imposed by the phase-matching bandwidth, which is associated with the group velocity mismatch of the BBO crystal. The bandwidth is calculated as follows [79, 80]

$$\delta\lambda_1 = \frac{1.39\ \lambda_1}{\pi L \left| \frac{\partial n_1}{\partial \lambda_1} - \frac{1}{2}\frac{\partial n_2}{\partial \lambda_2} \right|}, \tag{5.1}$$

where $\delta\lambda_1$ is the supported FWHM bandwidth of the fundamental pulse, λ_1 denotes the fundamental wavelength, λ_2 denotes the second-harmonic wavelength, L stands for the crystal length and $n_{1/2}$ are the respective refractive indices. With $\frac{\partial n_1}{\partial \lambda_1} \approx -0.03/\mu\mathrm{m}$, $\frac{\partial n_2}{\partial \lambda_2} \approx -0.22/\mu\mathrm{m}$ [81], and $L = 280\,\mu\mathrm{m}$, this results in $\delta\lambda_1 \approx 8\,\mathrm{nm}$. Consequently, the bandwidth of the second-harmonic is limited to $\delta\lambda_2 \approx 4\,\mathrm{nm}$, which corresponds to a transform-limited pulse duration of 59 fs for a Gaussian pulse shape.

In the experiment, the spectrum of the 400 nm radiation is measured directly behind the BBO (see Figure 5.1). The width of the spectral distribution is found to be slightly more broadband than expected, 5 nm FWHM, corresponding to a transform-limited pulse duration of 47 fs. The spatial beam profile of the 400 nm focus at the fiber entrance is shown in Figure 3.3.

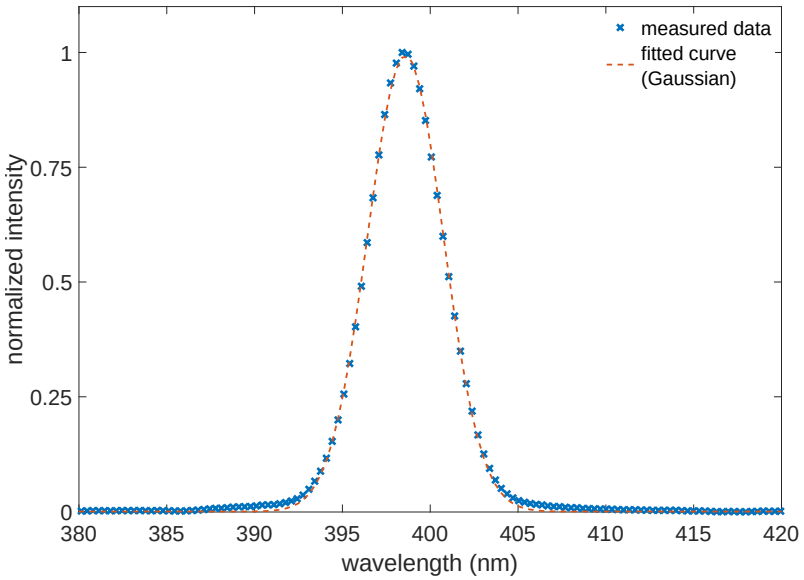

Figure 5.1.: Measurement of the spectral distribution of the UV radiation directly behind the BBO together with a Gaussian fit. The pulse energy in the UV is 6.5 mJ.

5.1. Spectral analysis behind the HCF

The UV spectrum is significantly broadened by SPM in the HCF. Figure 5.2 depicts a comparison between the input and output spectrum under optimized conditions for maximum spectral broadening. The output spectrum is measured in air after three reflections by metallic and dielectric mirrors (see Figure 3.4). Since the dielectric mirror is optimized for the spectral range between 380 nm and 420 nm, the shorter and longer wavelength ranges might be influenced by its reflection characteristics. A combination of fiber incoupling losses, propagation losses, absorption in helium, and losses at the mirrors and window behind the HCF reduces the pulse energy in Figure 5.2 compared to Figure 5.1.

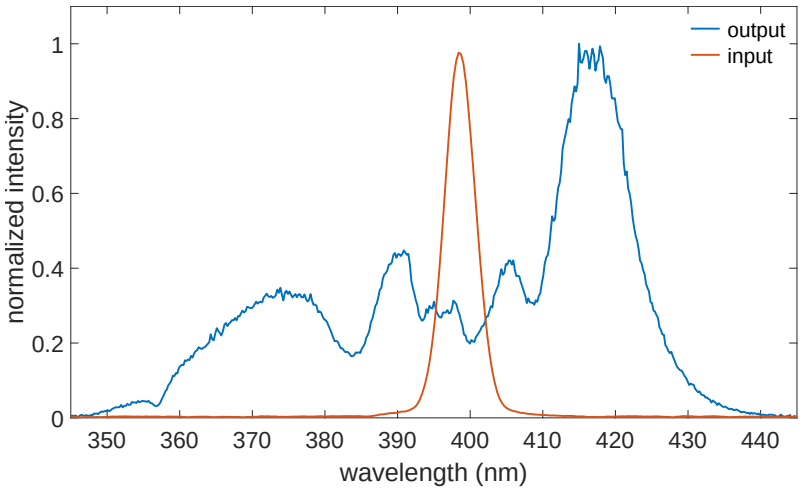

Figure 5.2.: Measurement of spectral broadening by SPM in the HCF. The fiber is filled with 1.5 bar helium in pressure gradient mode and the pulse energy behind the HCF is 1.2 mJ.

Figure 5.3 on the left illustrates the spectral broadening observed at various pressures. The fiber is operated in gradient mode, with vacuum conditions ($< 10^{-1}$ mbar) at the entrance and the specified pressure at the exit side. As expected, an increase in helium pressure results in a broader spectrum. Additionally, a considerable asymmetry in the spectral distribution is observed for higher pressures.

Figure 5.3 on the right presents the spectral broadening corresponding to different pulse energies. Similarly, an increase in pulse energy leads to a broader spectrum. Moreover, a comparable asymmetry to the one seen on the left side is evident for high energies.

The data in Figure 5.3 is compared with simulations close to the expected parameters, which are shown in Figure 5.4. The assumed parameters for the simulations are the following: 47 fs FWHM duration of a transform-limited Gaussian pulse and 5 m fiber length. For the pressure scan, a pulse energy of 1.5 mJ is assumed, accounting for the losses at the mirrors and the window. For the energy scan, the helium pressure is set to 1 bar, with the energies multiplied by 1.25 to compensate for reflection losses.

The overall behavior is similar for lower pressures and pulse energies. However, at higher pressures, the measured spectrum appears truncated for wavelengths above 420 nm. On the shorter wavelength side, the deviations are even more pronounced. This pattern is also observed in the lower wavelength range at higher pulse energies. One possible explanation is a combination of plasma/material absorption and the reflection characteristics of the mirrors.

Another likely contribution to the deviations is the assumption of a transform-limited input pulse in the simulations. Figure 5.5 shows the same simulation results as in Figure 5.4, but with an additional TOD of 15 000 fs^3 applied to the input pulse. This adjustment produces an asymmetry similar to that observed in the experimental data.

To ensure a well-behaved phase and a balanced spectral distribution that is efficiently reflected by the dielectric mirrors in the 4f setup and for beam transport to the gas cell, the spectral range for subsequent experimental investigations is restricted to approximately $380 - 420$ nm.

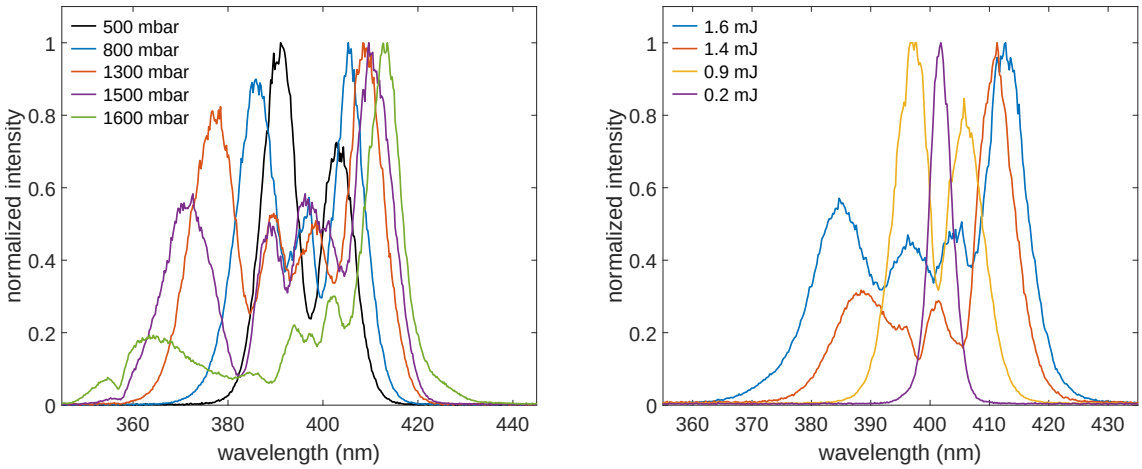

Figure 5.3.: Left: spectral distribution behind the HCF for different helium pressures at the exit side. The energy behind the fiber is between 1.1 and 1.2 mJ for all curves. Right: spectral distribution behind the HCF for different pulse energies with 1 bar helium at the exit side.

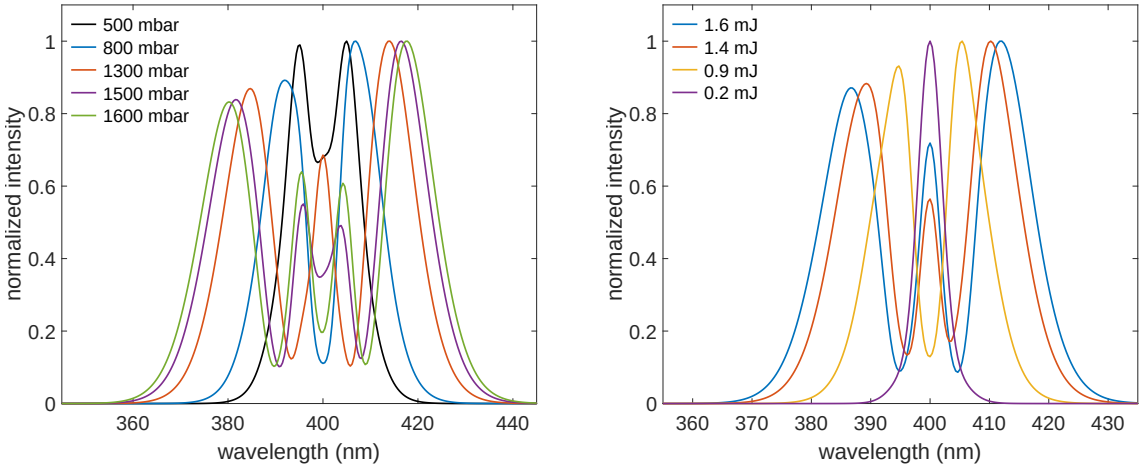

Figure 5.4.: Left: simulation results for the spectral distribution behind the HCF for different helium pressures at the exit side. Right: simulation results for the spectral distribution behind the HCF for different pulse energies with 1 bar helium at the exit side.

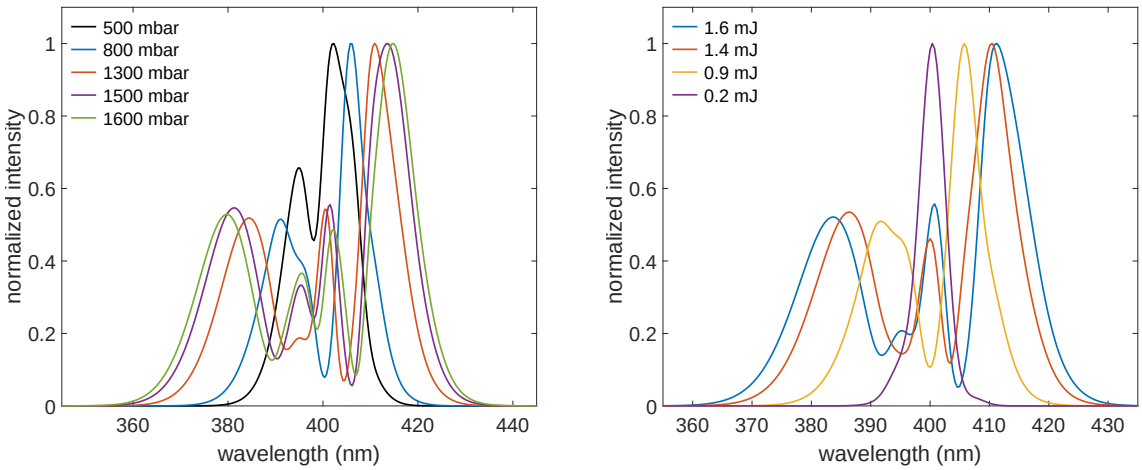

Figure 5.5.: Simulation results for an additional input TOD of 15 000 fs^3.

5.2. Fringe-resolved interferometric autocorrelation

To determine the pulse duration behind the 4f setup, the FRIAC technique is utilized. The theoretical framework for this method is introduced in Chapter 2.4.3. Two replicas of the UV pulse are generated by a double-comb mirror consisting of two silicon gratings, as described in [46]. A delay between the two pulse replicas is induced by moving one of the silicon gratings using a linear stage. Behind the double-comb mirror, the beam is focused onto a detection unit, which is described in Section 5.2.1. In the focal plane, two interference patters develop due to diffraction at the two silicon gratings. When overlapping the patterns by aligning the gratings, the resulting intensity in the zero diffraction order corresponds to the field autocorrelation. Utilizing a second-order process in the detector, the FRIAC trace is obtained (see Equation (2.43)). By driving higher-order processes, higher-order FRIAC traces can be measured, as described in Chapter 2.4.3.

Figure 5.6 depicts the double-comb mirror alongside the intensity distribution in the focal plane, depending on the phase difference between the two pulse replicas. At a phase difference of zero, there is maximum intensity in the 0th diffraction order, whereas at a phase difference of $\pi/2$, the 0th diffraction order vanishes.

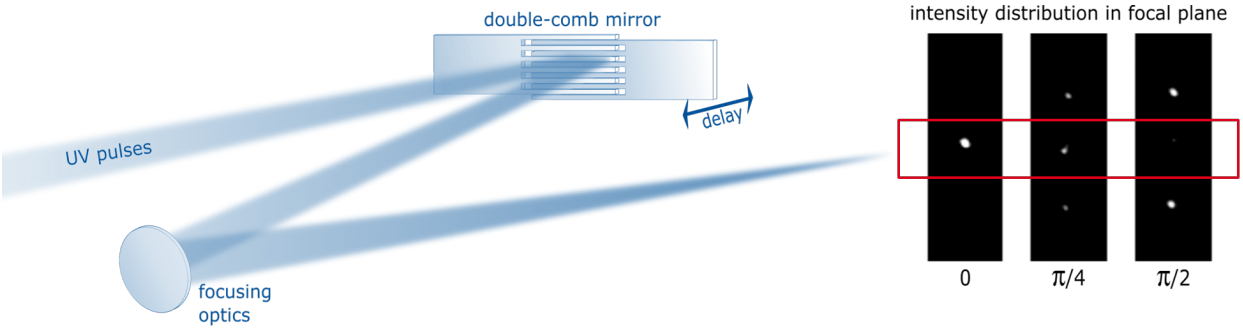

Figure 5.6.: Simplified illustration of the double-comb mirror together with the measured intensity distribution in the focal plane for a phase difference of zero, $\pi/4$ and $\pi/2$ between the two pulse replicas. The red box highlights the 0th diffraction order.

5.2.1. Detection unit

The detection unit comprises three components: a thin platinum wire, an electrode and a glass plate. Figure 5.7 (a) presents a schematic depiction of the detector. The entire setup is mounted on a plastic holder and placed in a vacuum environment on three linear stages for precise adjustment relative to the UV beam.

Behind the glass plate, a long-pass filter is installed to filter out the UV light for fluorescence imaging. Figure 5.7 (b) shows a camera image of the non-overlapped diffraction patterns in the focal plane together with the platinum wire. The electrode and both ends of the wire are connected to the outside via feedthroughs, allowing for the recording of the photoelectron current, application of the bias voltage, and heating of the wire with a small current.

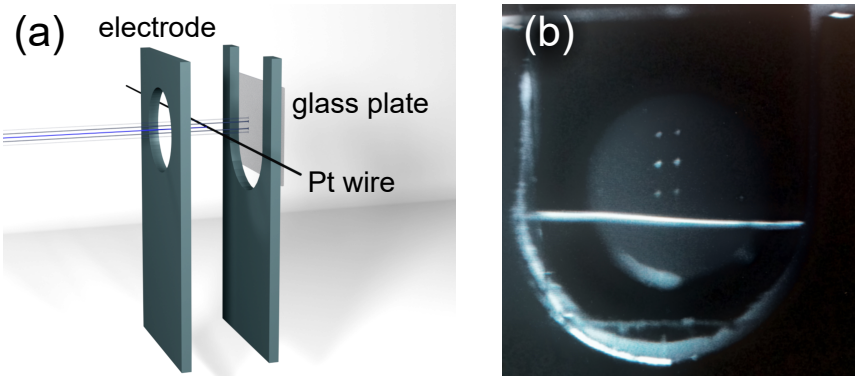

Figure 5.7.: (a) FRIAC detection unit with electrode, platinum wire and glass plate. (b) Fluorescence image of the non-overlapped diffraction patterns in the focal plane and the platinum wire.

To record FRIAC traces, the detector is positioned in the focal plane with the wire completely blocking the zero diffraction order. The shadowing effect of the wire can be observed in the fluorescence, allowing for precise adjustment of the wire position. Photoelectrons are generated at the platinum surface and extracted from the electrode by applying a bias voltage. To enhance the stability of the platinum surface conditions, a small current is sent through the wire to induce slight heating. The photoelectron current is amplified using a preamplifier (SR570, Stanford Research Systems), and the signal is recorded by a digital oscilloscope (WaveRunner, LeCroy), which is controlled by a Python script for data acquisition on a connected computer.

Depending on the UV intensity, second- or higher-order processes result in the emission of photoelectrons from the platinum. The work-function of platinum is in the range of 5.1 to 5.9 eV, the exact value depends on the method of evaluation and the surface conditions [82]. The photon energy corresponding to 400 nm is only 3.1 eV, and thus first-order processes do not contribute to the signal.

5.2.2. Field autocorrelation

When the detector is moved downward such that the wire does not block the beam, the glass plate provides a fluorescence image of the UV intensity distribution in the focal plane, as shown in Figure 5.7 (b). By recording the overlapped diffraction pattern and extracting the fluorescence intensity of the zero diffraction order, the field autocorrelation is obtained (see Chapter 2.4.1).

Figure 5.8 presents extracted data of a 400 nm pulse, which is not spectrally broadened in the HCF, as the fiber is not filled with gas. Additionally, the spectrum computed using the FFT algorithm is depicted. As expected, the trace is modulated symmetrically above and below a constant offset. The inset provides a detailed view of the oscillations near the center. Ideally, the autocorrelation should be symmetric with respect to zero delay. However, a noticeable asymmetry is present, likely due to fluctuations in the laser pulses, combined with slight misalignment of the double-comb mirror. In the spectral distribution, only one peak is observed at the central frequency of the pulse.

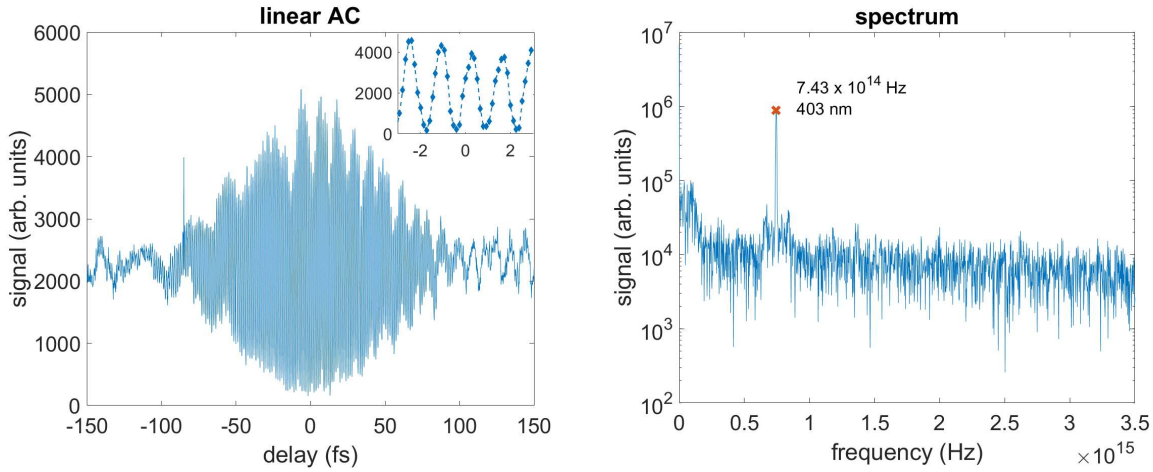

Figure 5.8.: Field autocorrelation extracted from the fluorescence intensity of the zero dispersion order together with the FFT of the signal (spectrum). Note that the spectrum is plotted on a logarithmic scale.

5.2.3. Second- and higher-order FRIAC

Figure 5.9 presents a second-order FRIAC trace of a compressed pulse behind the 4f setup. This pulse exhibits a broadened spectrum, which is shown in Figure 5.14 in the top row. As expected, the oscillations around a constant offset exhibit a ratio of approximately one to eight between the peak and the wings. To extract the pulse duration, the data is low-pass filtered, as explained in Chapter 2.4.3. For simplicity, a Gaussian pulse shape is assumed, and a fit is applied to the low-pass filtered data.

The results are summarized in Table 5.1. The autocorrelation width is determined to be 13.5 fs FWHM, corresponding to a pulse duration of 9.6 fs FWHM. The spectral distribution features a primary peak at the central frequency and a secondary peak at twice the frequency, with the secondary peak being significantly weaker than the primary one.

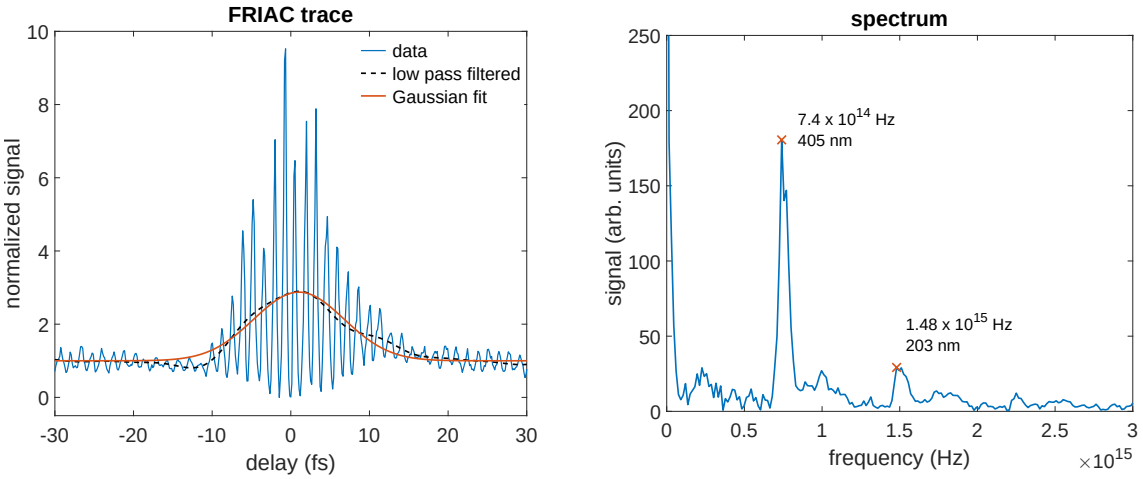

Figure 5.9.: Second-order FRIAC trace together with the FFT of the signal (spectrum). The spectrum is plotted on a linear scale.

Figure 5.10 displays a higher-order FRIAC trace recorded with increased UV intensity on the platinum wire, along with the corresponding spectral distribution. Analogous to the previous case, the data was low-pass filtered. However, due to the potential involvement of multiple processes of different orders, extracting the pulse duration is not straightforward. An upper limit can be determined by assuming a pure process of the highest order observed in the spectrum.

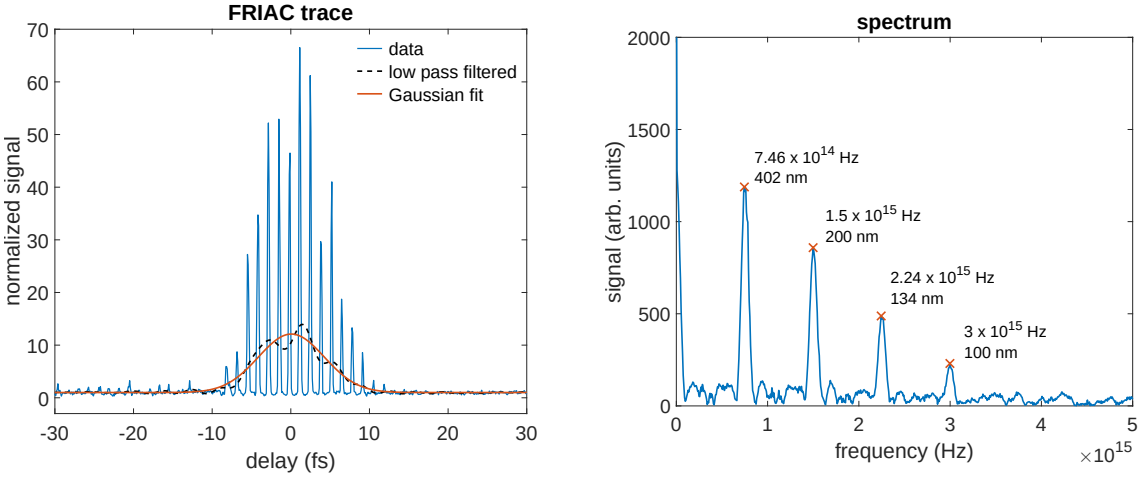

Figure 5.10.: Higher-order FRIAC trace together with the FFT of the signal (spectrum). The spectrum is plotted on a linear scale.

In Figure 5.10 on the right, there are four distinct peaks visible in the spectrum. As expected, these peaks are equally spaced, being integer multiples of the central frequency of the pulse. The highest frequency peak is located at 3×10^{15} Hz,

which is four times the central frequency of the pulse. According to theory (see Chapter 2.4.3), a pure fourth-order process would exhibit a ratio of 1:128 between the peak and the baseline. However, the ratio observed in the experimental data is lower, though it is not sufficiently low to correspond to a pure third-order process, which would show a ratio of 1:32.

The evaluation results are summarized in Table 5.1. The autocorrelation width of the Gaussian fit in Figure 5.10 on the left is 9.9 fs FWHM. Assuming a pure fourth-order process, this corresponds to a pulse duration of 9.4 fs FWHM, which serves as an upper limit and is in good agreement with the results obtained from the second-order FRIAC trace in Figure 5.9.

Table 5.1.: Evaluation of the FRIAC traces in Figure 5.9 and 5.10. The pulse duration of the higher-order trace is computed assuming a pure fourth-order process. This value serves as an upper limit.

	Figure 5.9: second-order	Figure 5.10: higher-order
extracted IAC FWHM (fs)	13.5 ± 0.3	9.9 ± 0.1
calculated pulse FWHM (fs)	9.6 ± 0.2	$\leq (9.4 \pm 0.1)$

5.2.4. Dispersion manipulation

This section covers FRIAC measurements of pulse elongation due to dispersion. Initially, the measurement principle is tested by introducing a known material into the beam path. Subsequently, the effect of detuning the 4f setup is investigated.

Dispersion introduced by additional material

To analyze the impact of pulse broadening due to dispersion on the measured FRIAC traces, dispersion is artificially introduced by placing fused silica in the beam path directly before the autocorrelation measurement. Moreover, any potential (higher-order) chirp in the laser pulse would be difficult to detect in the autocorrelation traces (see Figure 2.9), but it would influence the broadening behavior introduced by the additional material.

Figure 5.11 displays a FRIAC trace measured without the additional material on the left and a FRIAC trace with 1 cm of fused silica on the right. The evaluation results are summarized in Table 5.2. Analogous to Figure 5.8, the pulse is not spectrally broadened in the HCF, as the fiber is not filled with gas.

The autocorrelation width of the Gaussian fit in Figure 5.11 without additional material is 63 fs FWHM, whereas the autocorrelation width with 1 cm of fused silica in the UV beam is 80 fs FWHM. Due to insufficient sampling, the maximum order of processes involved cannot be definitively determined from the Fourier transformed data. However, since the ratio between peak value and baseline is higher than 1:32, contributions from the fourth order are assumed. This results in an upper limit for the pulse duration of 60 fs without additional material and 76 fs with 1 cm of fused silica.

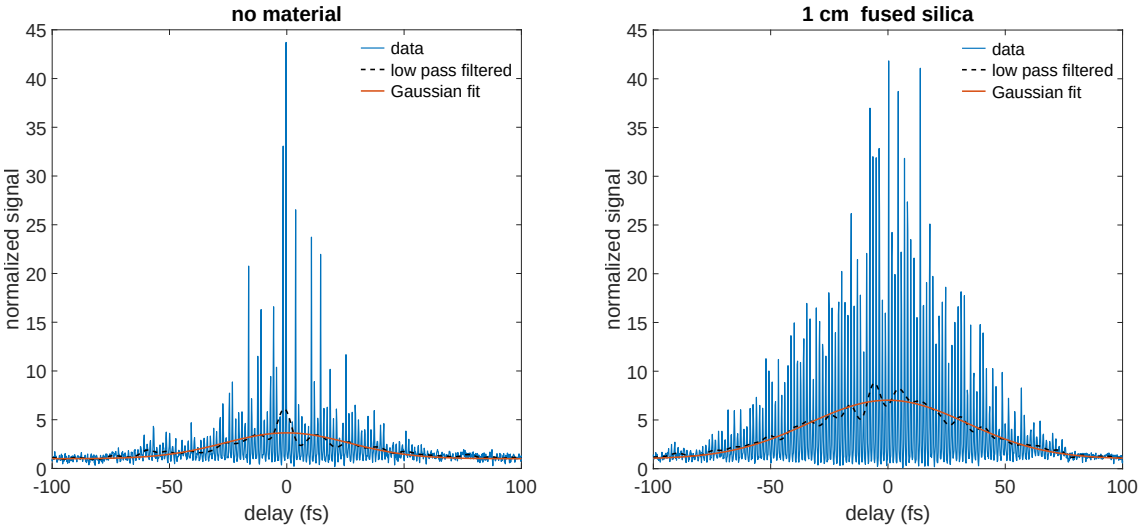

Figure 5.11.: FRIAC traces with and without 1 cm of fused silica in the beam path. The traces suffer from under-sampling due to the long delay values.

Table 5.2.: Evaluation of the FRIAC traces in Figure 5.11. The pulse duration is computed assuming a pure fourth-order process. This value serves as an upper limit.

	no material	1 cm fused silica
extracted IAC FWHM (fs)	63 ± 2	$79,8 \pm 0.8$
calculated pulse FWHM (fs)	$\leq (60 \pm 2)$	$\leq (76.0 \pm 0.8)$
expected GDD (fs^2)	0	976
expected pulse FWHM (fs)	60 ± 2	75.0 ± 0.8

Since the GVD of fused silica is approximately 97.6 fs^2/mm for 400 nm radiation [83], the total GDD expected from 1 cm propagation is 976 fs^2. Assuming a 60 fs input pulse, the expected duration behind the material is 75 fs, which is slightly shorter than the extracted values from the measurement but reasonably close to the expected value and well within the range of uncertainty.

Dispersion manipulation in the 4f setup

To investigate the effect of detuning the 4f setup in the experiment and compare it to the numerical simulations presented in Chapter 4.3, FRIAC traces are recorded for different lens positions. Three exemplary traces are depicted in Figure 5.12, while the corresponding evaluation results are provided in Table 5.3.

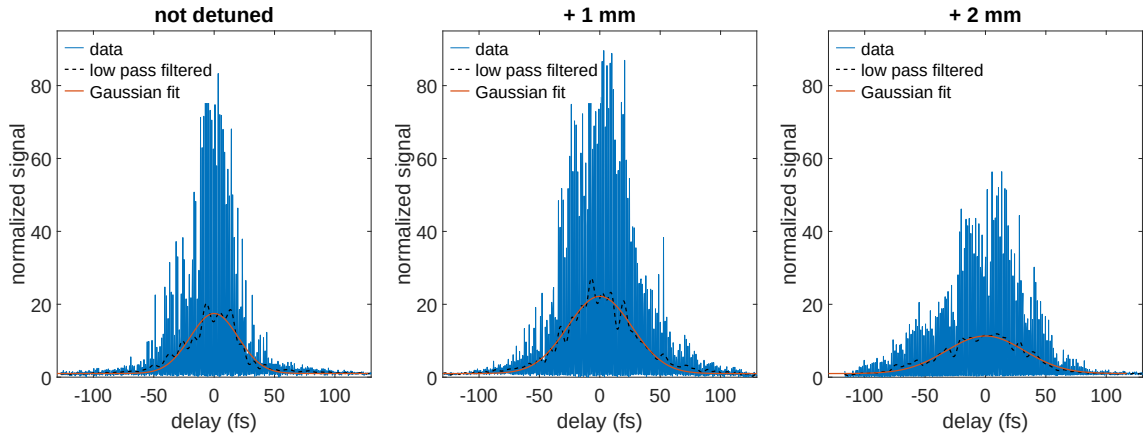

Figure 5.12.: FRIAC traces for three different lens positions in the 4f setup.

Table 5.3.: Evaluation of the FRIAC traces for three different lens positions together with the expected GDD values (taken from Figure 4.19) and calculated GDD for the extracted pulse lengths, assuming $0\,\mathrm{fs}^2$ for the non-detuned scenario.

	non-detuned	+ 1 mm	+ 2 mm
extracted IAC FWHM (fs)	46.8 ± 0.8	61.6 ± 0.8	73 ± 1
calculated pulse FWHM (fs)	$\leq (44.6 \pm 0.8)$	$\leq (58.7 \pm 0.8)$	$\leq (69 \pm 1)$
expected GDD (fs^2)	0	441	882
expected pulse FWHM (fs)	44.6 ± 0.8	52.4 ± 0.5	70.7 ± 0.3

The evaluation of the measurements for three lens position reveals significant pulse broadening for the detuned cases. Qualitatively, the observed behavior aligns well with the simulations. However, the elongated pulse for 1 mm lens detuning is slightly longer than expected.

Furthermore, a certain asymmetry is apparent in the FRIAC traces. Since the ideal autocorrelation signal is expected to be completely symmetric, it is evident that systematic errors are present in the experimental setup. Possible sources of error include intensity drifts and pointing instabilities during a single delay scan, which typically lasts half an hour.

5.2.5. Spectral selection

As discussed in Chapter 3.4, the 4f setup allows for the manipulation of pulses in the frequency domain by inserting a simple mask between the two mirrors of the retro-reflector, thereby blocking a part of the spectrum. Figure 5.13 provides a schematic depiction of this geometry. Figure 5.14 displays second-order FRIAC traces for a pulse with a full spectrum, as well as two pulses with modified spectra. Additionally, the corresponding UV spectra are shown.

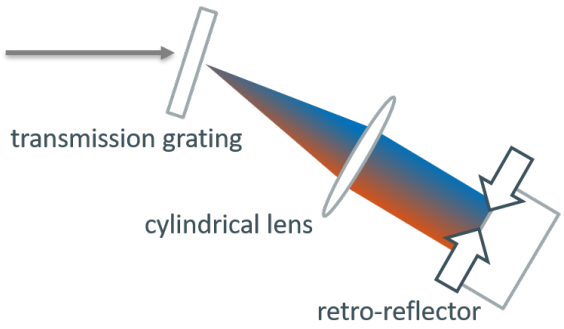

Figure 5.13.: Geometry of the 4f setup together with a mask to cut the spectrum. The position of the mask is denoted by the two arrows at the retro-reflector.

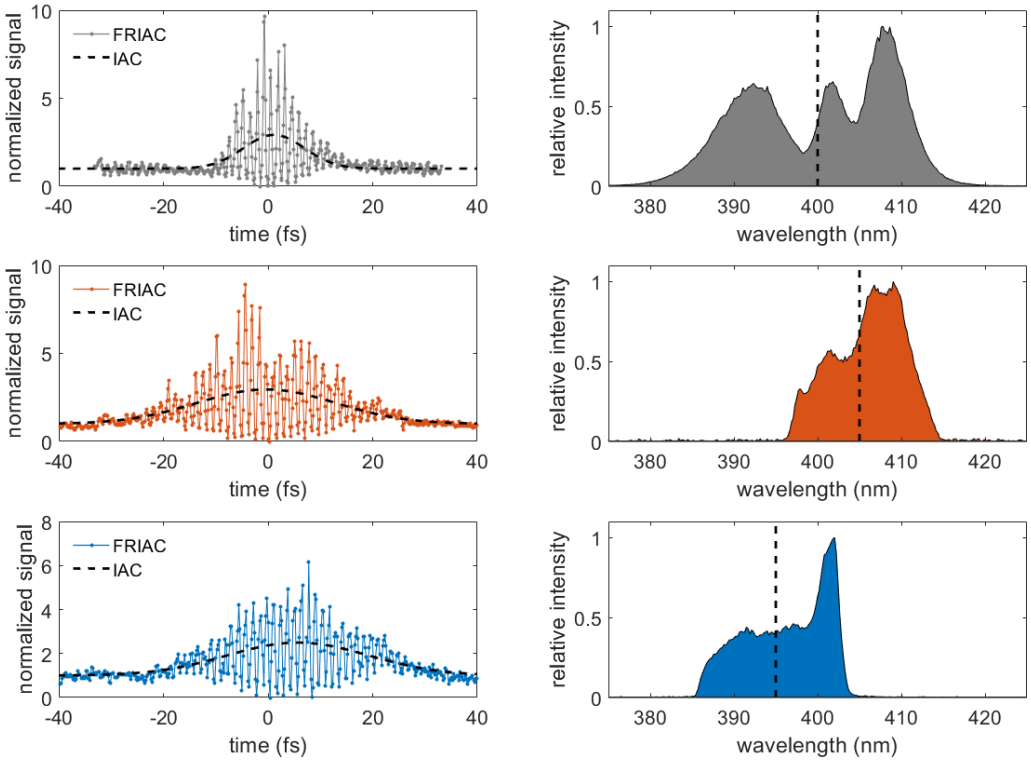

Figure 5.14.: Second-order FRIAC traces recorded behind the 4f setup together with the corresponding UV spectra. Top: shortest pulse, full spectrum (no mask). Middle: longer pulse, red part of the spectrum. Bottom: longer pulse, blue part of the spectrum.

Table 5.4.: Evaluation of the FRIAC traces in Figure 5.14.

	top	middle	bottom
extracted IAC FWHM (fs)	13.5 ± 0.3	31 ± 1	31.3 ± 0.8
calculated pulse FWHM (fs)	9.6 ± 0.2	22.1 ± 0.7	22.1 ± 0.6
central wavelength (nm)	≈ 400	≈ 405	≈ 395
$1/e^2$ spectral width (nm)	≈ 29.3	≈ 16.6	≈ 16.3

The FRIAC measurement with the full spectrum was previously shown along with the corresponding FFT in Figure 5.9. Since the pulse is relatively close to the transform limit, it is expected that measurements with the cut spectra would exhibit a longer pulse duration, which is indeed observed in the experiment. Furthermore, the shape of the FRIAC traces is slightly altered for the cut spectra, revealing wings with fading fringes on both sides, which is an indication for dispersion (see Chapter 2.4.3).

Calculating the TBP to determine the quality of pulse compression is not straightforward in this case, primarily because the spectra generated by SPM do not resemble a Gaussian distribution. To characterize and compare the spectra, the $1/e^2$ definition is chosen to calculate the spectral widths and central wavelengths in Table 5.4. Despite the cut spectral width being slightly broader than half the full spectral width for both cases, the pulse duration is slightly longer than double the value of the short pulse. This observation confirms that the spectral phase is not perfectly flat for the cut spectra shown in Figure 5.14 (middle and bottom).

However, it is feasible to tune the central wavelength of the UV over an interval of 10 nm, while maintaining a reasonably short pulse duration of 22 fs FWHM. For the full spectrum, pulses as short as 10 fs FWHM are obtained.

These UV pulses are utilized to generate wavelength-tunable VUV radiation by third-harmonic generation. In Figure 3.9, beam waist scans around the focus for THG generation together with calculated M^2 values are presented. An experimental characterization of the resulting VUV pulses is provided in the following chapter.

6. VUV pulse characterization

As described in Chapter 3.5, the VUV spectral range is reached through THG of UV pulses in a gas cell. Given the significantly enhanced performance of the pulsed gas cell compared to the static gas cell, all pulses analyzed in this chapter are generated using the pulsed version.

The nonlinear media utilized for frequency conversion in this chapter are argon and xenon, as these gases show the highest conversion efficiency in the experiment. Unfortunately, the refractive index model used in the simulations introduced in Chapter 4.2 is not valid in the VUV range for these gases. Especially for xenon, with a resonance line at 129.6 nm [48], the linear and nonlinear refractive index in the VUV is not straightforward to implement in the pulse propagation provided by Luna.jl [57]. Therefore, a direct comparison between simulation and experiment is beyond the scope of this work.

6.1. Energy measurement

An absolute measurement of photon numbers in the VUV spectral range is challenging since it requires either efficient separation from the much more intense 400 nm fundamental radiation or a detection scheme that is exclusively sensitive to VUV wavelengths. Separating the 400 nm radiation from the generated VUV pulses for conventional energy measurements, such as using a photodiode, is difficult due to the high sensitivity of most detectors to stray UV light. Additionally, each reflection at dielectric mirrors or silicon Brewster plates used for wavelength separation results in significant loss in the VUV range. Therefore, a technique that is insensitive to UV radiation and relies on single-photon absorption is chosen.

Figure 6.1 presents a schematic depiction of the detection tube, which contains a gaseous medium that converts absorbed VUV radiation into a measurable current via photoionization. The tube is installed at a distance of one meter from the origin of the harmonic conversion to prevent material damage and unwanted multiphoton processes due to high UV intensities. The gas is confined by thin magnesium fluoride windows (1.5 mm) at both the entrance and exit side of the tube. Iodobenzene molecules are ionized by single-photon absorption of VUV photons. A 12.5 cm long

wire, positioned parallel to the beam within the tube, collects the resulting charged particles. The detection of either electrons or ions is controlled by the polarity of the applied bias voltage (see Figure 6.2). Valves at the gas inlet and outlet ensure a steady flow of gas at a constant pressure, thereby maintaining a continuous supply of non-ionized particles.

Iodobenzene is selected due to its ionization energy of 8.8 eV [84], which is low enough to permit single-photon absorption of the VUV light, while being sufficiently high to prevent two-photon absorption of the UV radiation. The absorption cross section of iodobenzene at 133 nm is 75 Mb [85].

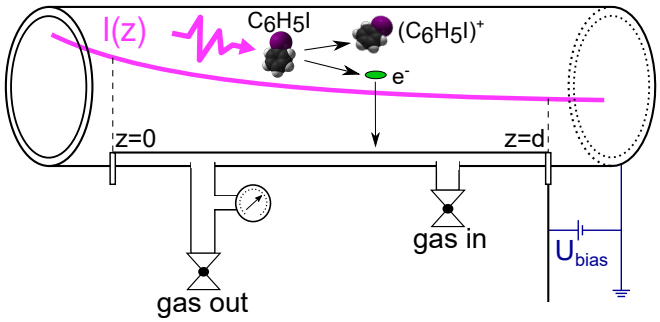

Figure 6.1.: Detection tube for VUV pulse energy measurement via absorption in iodobenzene. $I(z)$ is the light intensity and d is the wire length. In the illustrated case, a positive bias voltage is applied to the wire to detect electrons.

Due to absorption, the VUV intensity and photon number exhibit an exponential decay. The photon number N as a function of the propagation distance z is given by

$$N(z) = N_0 e^{-\rho\sigma z}, \tag{6.1}$$

where N_0 denotes the initial photon number, ρ represents the particle density and σ is the absorption cross section. The number of absorbed photons ΔN is expressed as

$$\Delta N = N(0) - N(L) = N_0(1 - e^{-\rho\sigma d}), \tag{6.2}$$

where d is the length of the wire. When no processes other than single-photon absorption by VUV radiation are involved, the number of charged particles detected equals ΔN. This results in

$$\Delta N = \left|\frac{Q}{q}\right|, \tag{6.3}$$

where Q denotes the detected charge for a single pulse and q represents the elementary charge. Combining Equation (6.2) and Equation (6.3) yields

$$N_0 = \frac{\Delta N}{(1 - e^{-\rho\sigma d})} = \frac{Q}{q(1 - e^{-\rho\sigma d})}. \tag{6.4}$$

The pulse energy E is computed by multiplying the number of photons with the photon energy

$$E = h\nu N_0 = 9.3\,\mathrm{eV} \times \frac{Q}{q(1 - e^{-\rho\sigma d})}, \tag{6.5}$$

where h is the Planck constant, ν denotes the light frequency and together they result in the VUV photon energy of 9.3 eV.

The current from the wire is measured using a variable gain sub-femtoampere current amplifier (DDPCA-300, FEMTO) connected to a digital oscilloscope (WaveRunner, LeCroy). Due to the relatively low repetition rate of 100 Hz, single-shot resolution is achieved. Integrating the measured data directly yields the accumulated charge for a single pulse.

6.1.1. Bias voltage

Figure 6.2 presents measured data for various bias voltages. Positive voltages correspond to electron detection, whereas negative voltages correspond to ion detection. Figure 6.3 shows the computed charge as a function of the bias voltage.

Overall, the signal behavior in Figure 6.2 exhibits symmetry with respect to the applied bias voltage. As the absolute value of the bias voltage increases, the peak height correspondingly increases. Moreover, higher bias voltages lead to narrower peaks due to the increased velocities of the charged particles. Interestingly, even at zero bias voltage, a small positive signal is observed, likely attributed to photoelectron emission from the wire due to scattered VUV light.

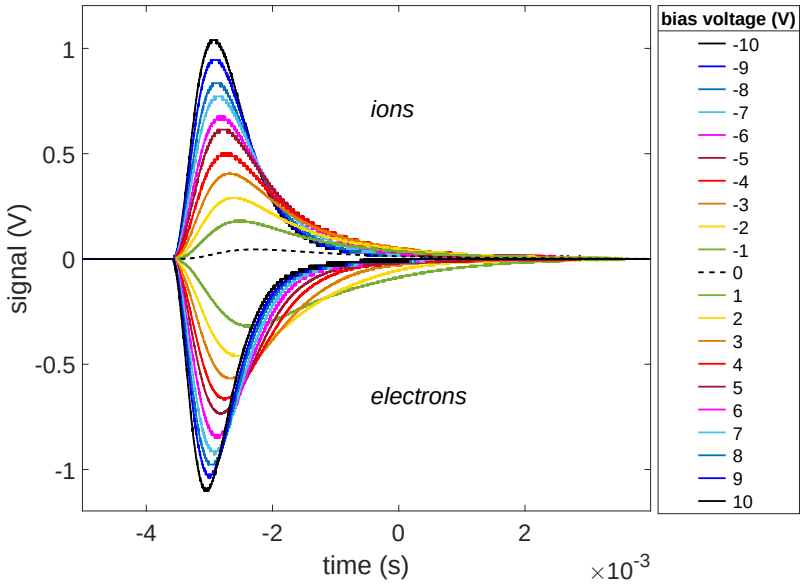

Figure 6.2.: Bias voltage scan. The amplifier setting is 10^7 V/A, and the data is averaged over 20 shots. The UV energy is 0.9 mJ, and the backing pressure of the pulsed nozzle is 220 mbar argon.

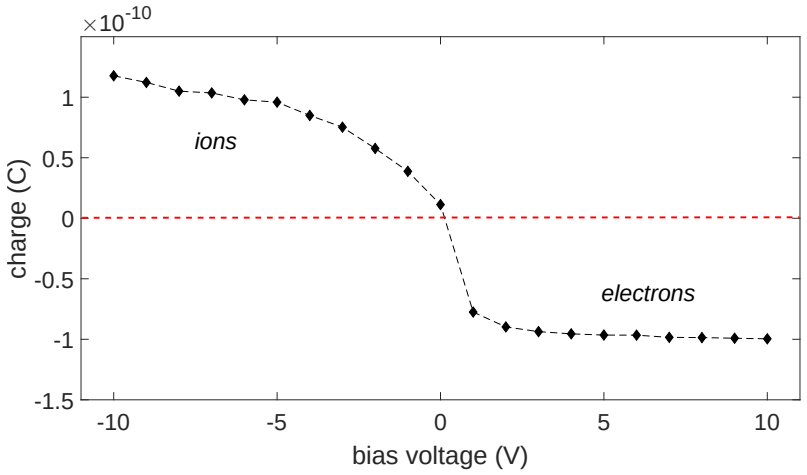

Figure 6.3.: Accumulated charge for a single pulse as a function of the bias voltage, computed by integrating the data from Figure 6.2.

Regarding the charge accumulated for a single pulse, which is depicted in Figure 6.3, the dependence on bias voltage differs slightly between the detection of electrons and ions. For ion detection, the charge increases more gradually with higher bias voltages and does not appear to approach saturation within the analyzed voltage range. In contrast, for electron detection, the increase in charge is much steeper at lower voltages and close to a bias voltage of 10 V, the accumulated charge for electron detection seems to be saturated.

The different characteristics observed for electrons and ions are most likely attributed to the significantly higher drift velocity and longer mean free path of electrons. Consequently, electron detection using a positive bias voltage of 10.5 V was chosen for the energy measurements.

6.1.2. Pressure dependence

To further investigate the performance of the detector, measurements for various iodobenzene pressures are conducted for ion and electron detection. Figure 6.4 presents the data obtained for ion detection, while the data for electron detection is shown in Figure 6.5.

In both cases, the curves recorded at higher pressures exhibit significant temporal broadening. Additionally, these broadened curves show a saturation effect in charge at higher pressures. A certain saturation effect is anticipated due to the accelerated exponential decay of the VUV photon number in the gas at increased particle densities. However, this phenomenon occurs at lower pressures than expected and is probably attributed to collisions between the particles at higher densities or space charge effects at the wire.

Since the measured curves do not exhibit unwanted broadening effects in the lower pressure range, relatively low iodobenzene pressures are chosen. In this range, an almost linear relationship between the computed charge and the applied iodobenzene pressure is expected and observed (see Figure 6.6 and Figure 6.7). However, the extrapolation of this linear behavior does not converge to zero at zero iodobenzene pressure. This offset will be analyzed and discussed in the following section.

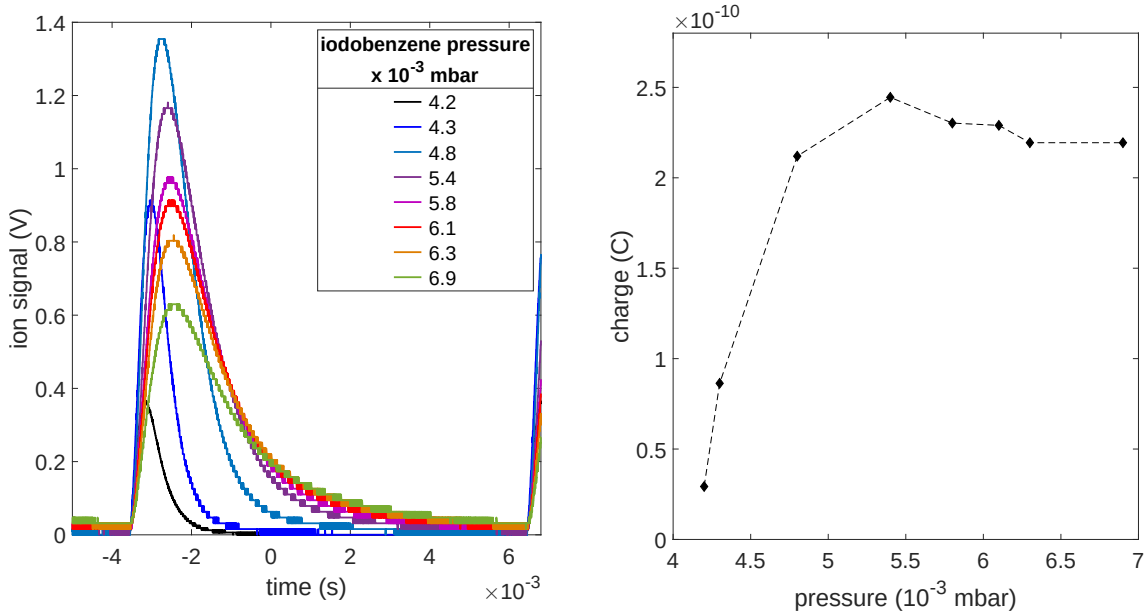

Figure 6.4.: Scan of the iodobenzene pressure for a bias voltage of −10 V. The amplifier settings and experimental parameters are the same as in Figure 6.2.

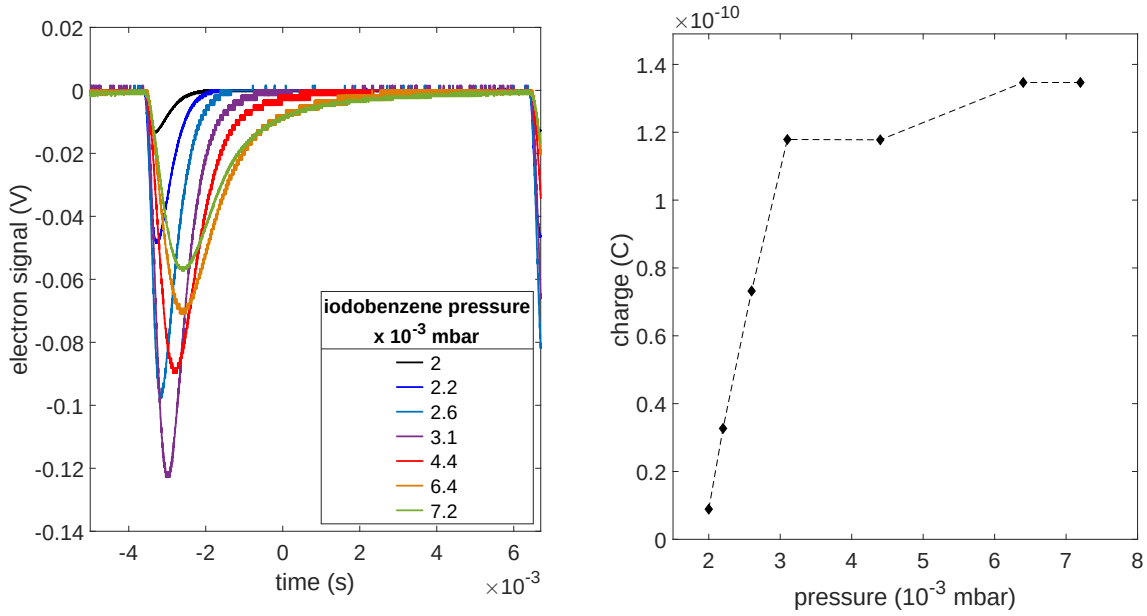

Figure 6.5.: Scan of the iodobenzene pressure for a bias voltage of 10.5 V. The amplifier setting is 10^6 V/A and the data is averaged over 20 shots. The UV energy is 1.1 mJ and the argon backing pressure of the nozzle is 160 mbar.

6.1.3. THG in argon

Figure 6.6 presents measured data for optimized THG conditions in argon. Prior to the measurements, the lens position, rotation and tilt in the 4f setup are adjusted to maximize the output signal. Additionally, the backing pressure of the gas and the voltage on the piezo opening the nozzle are carefully optimized.

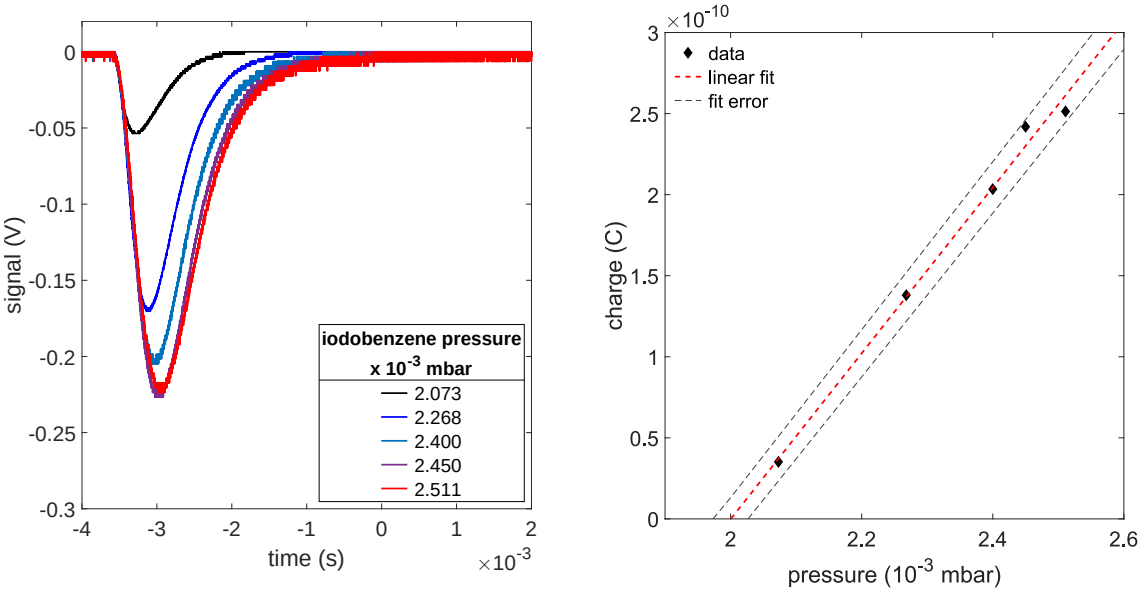

Figure 6.6.: Scan of the iodobenzene pressure for optimized THG conditions in argon. The UV energy is 1 mJ and the backing pressure of the pulsed nozzle is 290 mbar. The amplifier setting is 10^6 V/A, the bias voltage is 10.5 V and the data is averaged over 20 shots.

To determine the VUV pulse energy, a linear fit is applied to the accumulated charge for a single pulse depending on the iodobenzene pressure, which is shown in Figure 6.6 on the right. The fit reveals a pressure offset of 2×10^{-3} mbar, likely caused by the positioning of the gauge, which is not located directly within the detection tube but in the gas outlet line, as depicted in Figure 6.1.

Subtracting the retrieved offset from the measured pressure values and using Equation (6.5), yields a pulse energy of approximately 200 nJ in the detection tube. Table 6.1 summarizes the results of the calculation. The particle density in iodobenzene was modeled with the van der Waals equation using $a = 33.53\,\mathrm{L^2bar/mol^2}$ and $b = 0.1658\,\mathrm{L/mol}$ [82].

Table 6.1.: Evaluation of the VUV energy measurement for THG in argon (Figure 6.6).

iodobenzene pressure (10^{-4} mbar)	0.73	2.68	4.00	4.50	5.11
measured charge (10^{-10} C)	0.35	1.38	2.03	2.42	2.51
energy (10^{-7} J)	1.95	2.08	2.06	2.18	2.00
mean energy (10^{-7} J)	2.05 ± 0.09				

To compute the conversion efficiency, the UV pulse energy in the gas cell is calculated from the values measured behind the HCF, taking the transmission of the 4f setup (73%) and the reflections at the subsequent steering mirrors ($4\times99.5\%$) and focusing mirror (90%) into account. The total VUV energy is calculated from the measured pulse energy in the tube, considering the reflection (5%) and absorption (23%) of the magnesium fluoride window. For the UV, one obtains a scaling factor of 0.64 due to known losses between UV pulse energy measurement and harmonic generation, and for the VUV, one obtains a scaling factor of 1.3 due to known losses at the window between harmonic generation and VUV pulse energy measurement. The resulting UV energy is 0.64 mJ, the VUV energy is 267 nJ, and the conversion efficiency is 4.2×10^{-4}.

6.1.4. THG in xenon

Figure 6.7 presents measured data for THG in xenon. It is worth noting that the conditions were not optimized to the same degree as in the argon measurement shown in Figure 6.6. Similar to the previous case, the linear fit shows a pressure offset of 1.99×10^{-3} mbar, which is subtracted from the measured pressure values for further analysis. The evaluation reveals a pulse energy of approximately 220 nJ in the detection tube, corresponding to 286 nJ in the gas cell and a conversion efficiency of 3.7×10^{-4}. This is similar to the previous results in argon despite less carefully optimized THG parameters. The calculation results are given in Table 6.2.

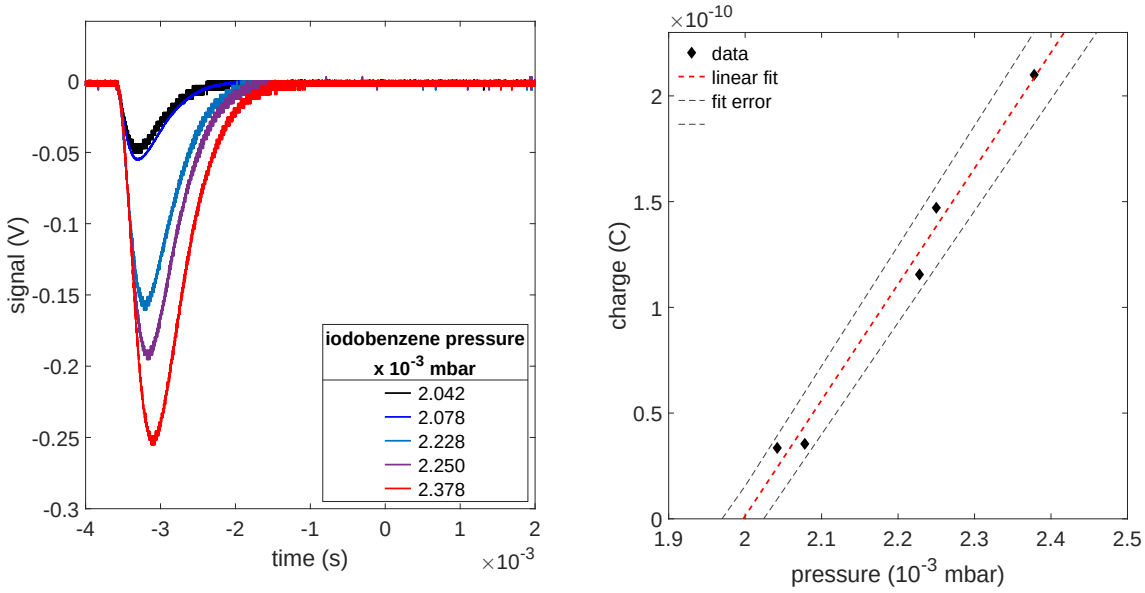

Figure 6.7.: Scan of the iodobenzene pressure for THG in xenon. The UV energy is 1.2 mJ and the backing pressure of the pulsed nozzle is 130 mbar. The amplifier settings are the same as in Figure 6.6.

Table 6.2.: Evaluation of the VUV energy measurement for THG in xenon (Figure 6.7).

iodobenzene pressure (10^{-4} mbar)	0.48	0.84	2.34	2.56	3.84
measured charge (10^{-10} C)	0.335	0.355	1.155	1.471	2.100
energy (10^{-7} J)	2.82	1.71	2.00	2.33	2.22
mean energy (10^{-7} J)	2.2 ± 0.4				

Since the iodobenzene pressure scans are fairly time and xenon consuming – two scarce resources towards the end of this PhD project – single measurements for further optimized THG in xenon are conducted under the same conditions as in Figure 6.7, using the retrieved value for the pressure offset in the detection tube. Figure 6.8 presents single-shot data of multiple pulses, whereas Figure 6.9 shows a measurement averaged over 100 shots.

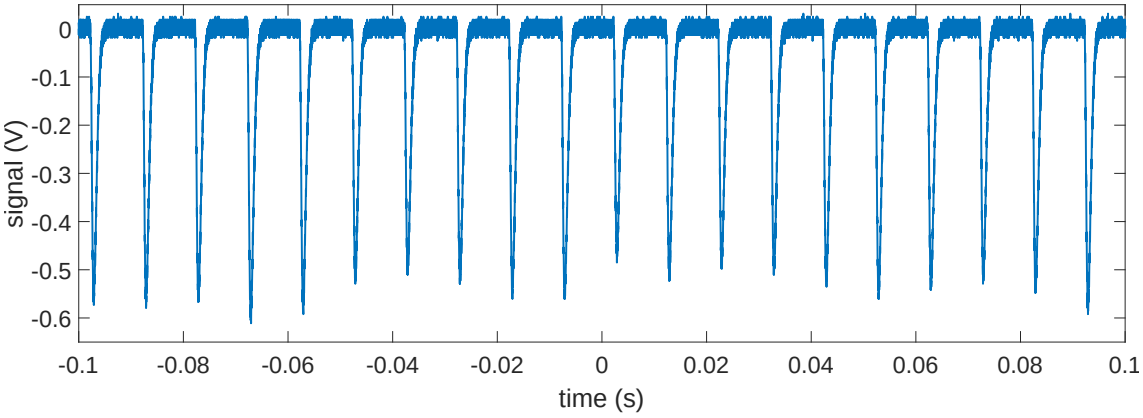

Figure 6.8.: Single-shot measurement of 20 VUV pulses for optimized THG in xenon. The UV energy is 1.4 mJ and the backing pressure of the pulsed nozzle is 200 mbar. The amplifier setting is 10^6 V/A and the bias voltage is 10.5 V. The offset-subtracted iodobenzene pressure in the detection tube is 2.03×10^{-4} mbar.

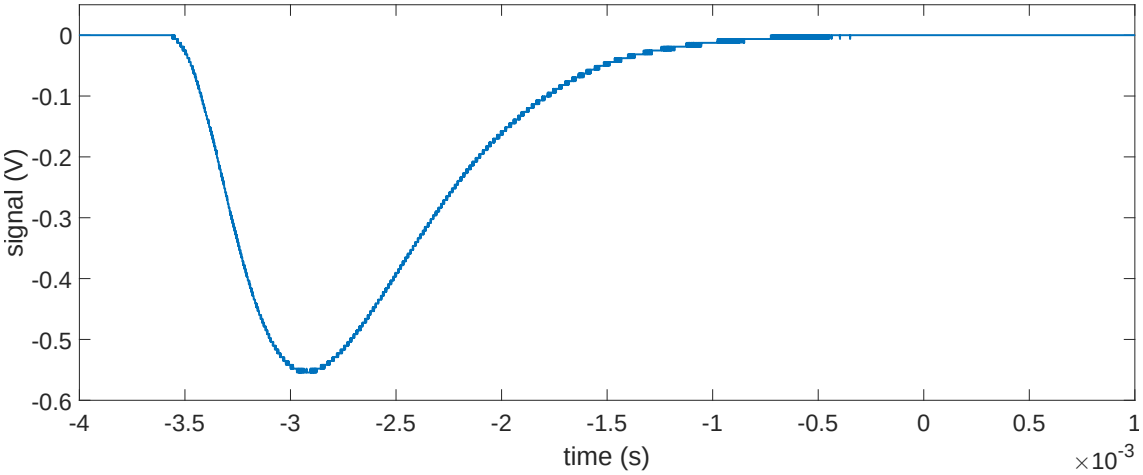

Figure 6.9.: Energy measurement for optimized THG in xenon, averaged over 100 shots. The settings are the same as in Figure 6.8.

The mean integrated charge and corresponding energy for the pulses in Figure 6.8 is given in Table 6.3, along with the values from the averaged measurement shown in Figure 6.9. The mean energy of the pulses in Figure 6.8 is (1.17 ± 0.08) µJ, which aligns well with the value of 1.23 µJ for the averaged measurement. The resulting conversion efficiency is 1.7×10^{-3}, with a UV energy of 0.9 mJ and a mean VUV energy of 1.5 µJ in the gas cell.

Table 6.3.: Evaluation of the VUV energy measurement for optimized THG in xenon.

		charge (10^{-10} C)	energy (10^{-6} J)
Figure 6.8	mean	5.75	1.17
	std. dev.	0.41	0.08
Figure 6.9	100 shot avg.	6.07	1.23

6.2. Spectral analysis

To investigate the spectral characteristics of the harmonic radiation generated in the gas cell, diffraction at a reflection grating was utilized. Figure 6.10 shows a schematic depiction of the experimental setup. The grating, coated with aluminum and featuring a groove density of 1200 lines/mm, is positioned one meter from the gas cell, which is operated with xenon. The diffracted light arrives at a phosphor screen (P43). The screen is imaged by a CCD camera. To eliminate UV stray light, a long-pass filter (GG455, Schott) is placed between the screen and the camera. The zero diffraction order and the minus first diffraction order of the UV radiation are prevented from hitting the phosphor screen using beam blocks. To calibrate the spectrum, both beam blocks can be removed to allow imaging of the UV radiation. The entire setup is placed in a vacuum environment, only the camera is located outside the vacuum chamber behind a window.

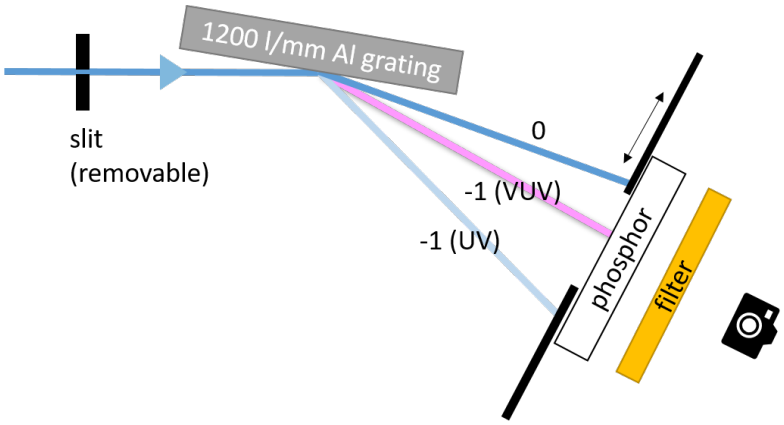

Figure 6.10.: Geometry of the experimental setup for spectral analysis of the VUV light.

6.2.1. Beam profile

Figure 6.11 presents a background-subtracted image of the minus first diffraction order, originating from the full beam profile of the VUV radiation. In addition to the prominent profile of the third harmonic (133 nm), the fifth harmonic of the 400 nm light (80 nm) is also visible. Since dispersion affects only the horizontal direction in Figure 6.11, the vertical intensity distribution, depicted in Figure 6.12, corresponds to the vertical VUV beam profile, assuming a linear behavior of the phosphor screen.

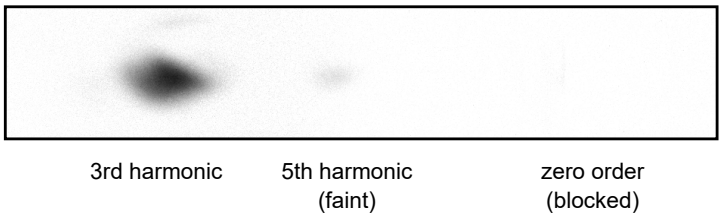

Figure 6.11.: Camera image of the minus first diffraction order of the VUV radiation without slit. The image is background-subtracted and the colors are inverted for better visibility.

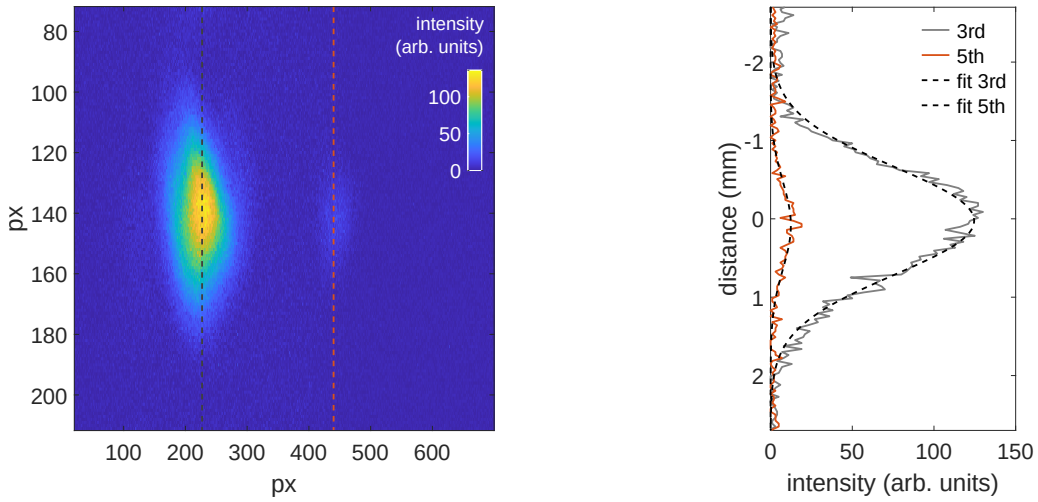

Figure 6.12.: Vertical cut through the harmonic beam profiles on the phosphor screen together with Gaussian fit functions. The distance axis is calibrated using the known diameter of the phosphor screen.

The vertical cut through the beam profile depicted in Figure 6.12 displays a well-behaved Gaussian-like shape for the 133 nm radiation. This observation suggests that the process differs from the six-wave mixing reported by Trabs et al. [27], which would be characterized by a ring shaped profile.

The Gaussian fit functions in Figure 6.12 on the right yield a FWHM diameter of 1.6 mm for the profile of the third harmonic and 1.3 mm for the profile of the fifth harmonic, which corresponds to $1/e^2$ beam radii of $w_{3rd} = 1.4\,\text{mm}$ and $w_{5th} = 1.1\,\text{mm}$, respectively. Together with a propagation distance of approximately 105 cm from the center of the gas cell, an estimate for the divergence half angles of the VUV beams is given by $\Theta_{3rd} \approx 1.3\,\text{mrad}$ and $\Theta_{5th} \approx 1.1\,\text{mrad}$. From the data presented in Figure 3.9 on the left, one obtains a divergence half angle of the fundamental 400 nm radiation of $\Theta_{400} = M^2\lambda_{400}/\pi w_{400} \approx 2.6\,\text{mrad}$, which is significantly larger than the value for the harmonic beams.

6.2.2. Quantitative analysis

To quantitatively analyze the spectral characteristics, a 60 µm slit is positioned in front of the grating. This setup increases the spectral resolution by avoiding convolution with the spatial beam profile. Due to the significantly higher intensity of the zero diffraction order compared to the other orders, two images are captured with different acquisition times and then merged to form a complete dataset of the diffracted light. Figure 6.13 displays the merged image along with the integrated intensity distribution. The spectrogram features four distinct peaks corresponding to the zero diffraction order, the minus first diffraction order of the 400 nm fundamental, the minus first order the third harmonic, and the minus first order of the fifth harmonic.

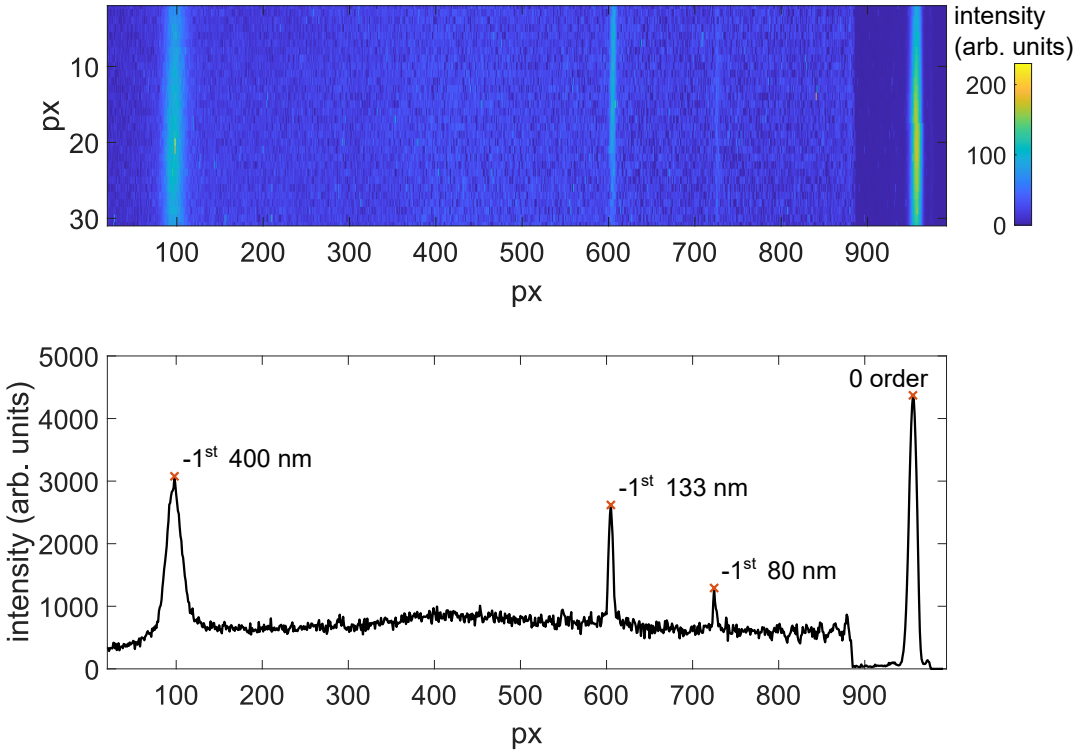

Figure 6.13.: Merged image of the diffracted light on the phosphor screen together with the integrated intensity distribution.

Using the geometry of the setup – specifically, the incidence angle on the grating ($\alpha = 65°$) and the angle between the phosphor and the grating ($\theta = 50°$) – the wavelengths of these harmonic peaks can be calculated by calibrating the measurement with the known wavelength of the UV radiation. Figure 6.14 depicts a sketch of the geometry with the relevant angles.

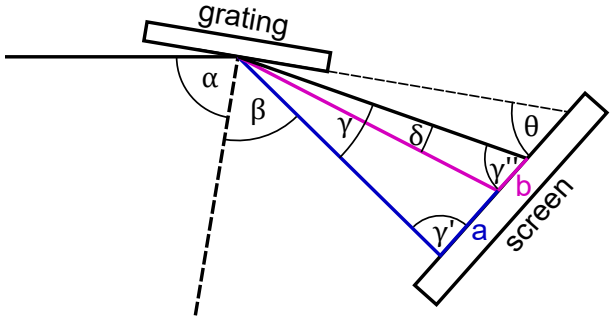

Figure 6.14.: Geometry of grating and screen with the relevant angles for the calculation.

The diffraction angle of the UV radiation, β, is calculated as

$$\beta = -\arcsin\left(\frac{\lambda_0}{g} - \sin(\alpha)\right) = 25.2°, \tag{6.6}$$

where $\lambda_0 = 400\,\text{nm}$ is the fundamental wavelength and $g = 1/1200$ mm is the grating period.

The angle between the zero diffraction order and the minus first order of the fundamental, γ, and the angles γ' and γ'' (see Figure 6.14) are given by

$$\gamma = \alpha - \beta = 39.8°, \gamma' = 90° + \beta - \theta = 65.2°, \gamma'' = 180° - \gamma - \gamma' = 75°. \tag{6.7}$$

To determine the angle between the zero diffraction order and the minus first order of the harmonics, δ, using distances a and b on the phosphor screen, the law of sines is applied twice and solved for δ

$$\frac{\sin(\gamma')}{\sin(\gamma)}(a+b) = \frac{\sin(180° - \gamma'' - \delta)}{\sin(\delta)}\, b \quad \rightarrow \quad \delta_{3rd} = 16.7°,\ \delta_{5th} = 10.9°. \tag{6.8}$$

Finally, the wavelength of the harmonic peaks λ_H is computed as

$$\lambda_H = (\sin(\alpha) - \sin(\alpha - \delta))\, g. \tag{6.9}$$

The resulting values for the wavelength are (133 ± 3) nm for the third harmonic and (80 ± 2) nm for the fifth harmonic, assuming a precision of one degree for the angles α and θ.

6.2.3. Relative wavelength shift

As detailed in Chapter 5.2.5, the central wavelength of the UV may be adjusted over an interval of 10 nm while maintaining a pulse duration of 22 fs FWHM. In the following, the spectral shift in the generated harmonic radiation will be analyzed.

Figure 6.15 illustrates the spectral distribution of the fundamental used for THG in the subsequent measurements under three conditions: full spectrum, only the blue part of the spectrum, and only the red part of the spectrum. Similar to Figure 5.14, the shift in central wavelength is approximately 10 nm.

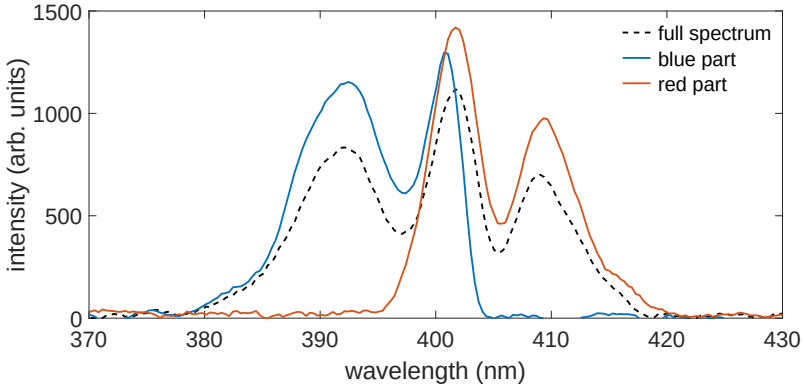

Figure 6.15.: Spectrum of the fundamental UV radiation. The full spectrum is depicted together with the cut spectra.

To enhance the spectral resolution and accurately record the wavelength shift in the harmonic radiation, the distance between the grating and the phosphor screen is increased. Consequently, the reference points from the fundamental 400 nm radiation are lost. However, since the objective is to measure relative wavelength shifts, the only additional information needed is the distance between screen and grating, which is 210 mm for the subsequent measurements, and an image of a known calibration target at the screen position to enable pixel-to-distance conversion.

Figure 6.16 presents the recorded images of the minus first diffraction order of the third harmonic on the left and the integrated spectral distribution on the right. To convert the x-axis from distance on the screen to wavelength shift, a linear approximation is applied due to the small difference in diffraction angle. Gaussian functions are fitted to the data to determine the central wavelength differences for the blue- and red-shifted spectra. The retrieved values are -1.4 nm and 1.4 nm, respectively, resulting in an overall shift of 2.8 nm between the two cut spectra. This value is only slightly lower than the expected value of $10\,\text{nm}/3 = 3.33\,\text{nm}$.

Similar to the third harmonic in Figure 6.16, Figure 6.17 presents the recorded images of the minus first diffraction order of the fifth harmonic. Again, Gaussian functions are fitted to the data to determine the difference in central wavelength for the blue- and the red-shifted spectra. The computed values are -0.3 nm and 0.2 nm, respectively, resulting in an overall shift of 0.5 nm between the two cut spectra. This value is notably lower than the expected value of $10\,\text{nm}/5 = 2\,\text{nm}$.

Naturally, the harmonic intensity is significantly reduced for the cut spectra. This reduction is caused not only by the decreased fundamental energy, due to blocking a portion of the beam, but also by the longer duration of the fundamental pulse resulting from the narrower spectral width.

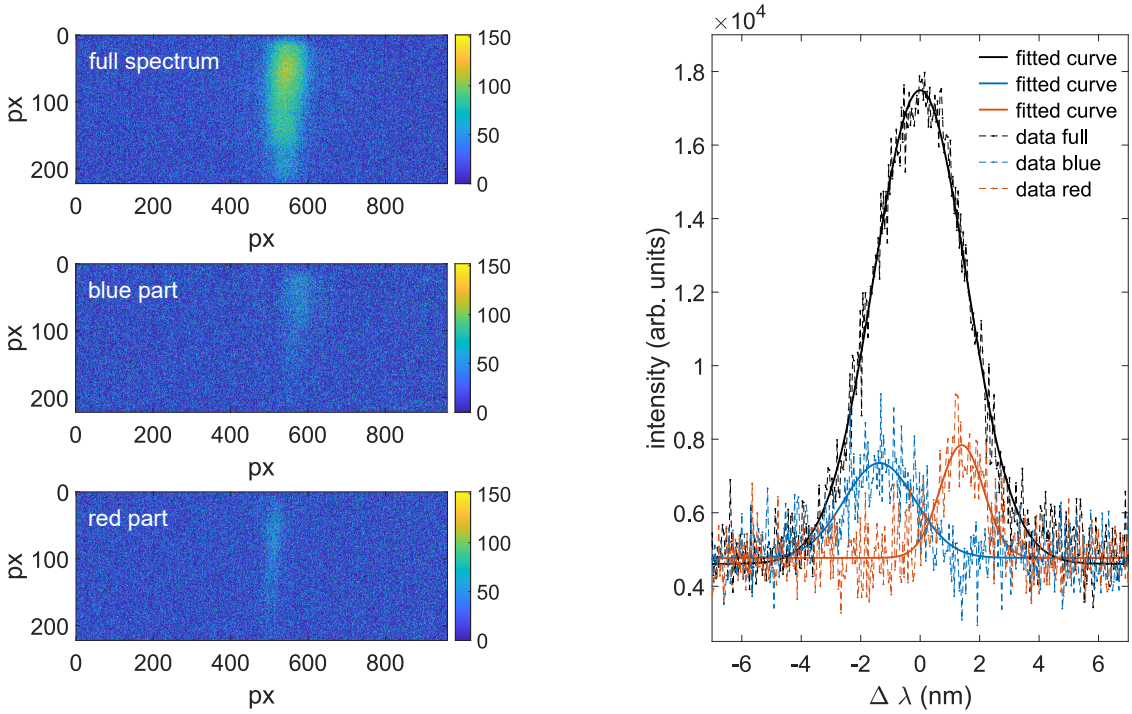

Figure 6.16.: Image of the minus first diffraction order of the third harmonic on the phosphor screen (left) and integrated spectral distribution (right).

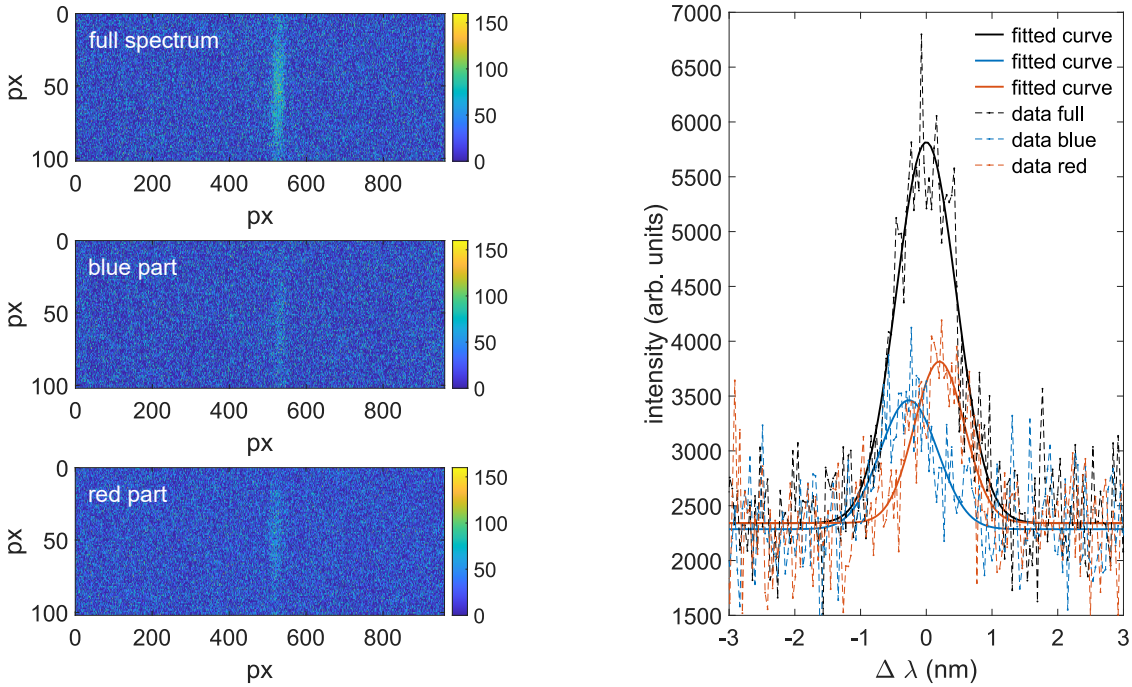

Figure 6.17.: Image of the minus first diffraction order of the fifth harmonic on the phosphor screen (left) and integrated spectral distribution (right).

7. Discussion & Outlook

In this chapter, the experimental results obtained in Chapters 5 and 6 are summarized and compared with the theoretical predictions and simulations established in Chapters 2 and 4. Subsequently, a few exemplary applications of the ultrashort pulsed light source in the VUV are presented, and possibilities for optimizing the experimental setup are considered.

The **UV pulses** characterized in Chapter 5 were found to be as short as 10 fs FWHM, employing the FRIAC technique. Unlike earlier experiments utilizing the same double-comb mirror structure as a split-and-delay unit, the detection scheme is based on solid-state photoelectron emission from a platinum wire. Notably, the order of the nonlinear detection process scales with the light intensity incident on the platinum wire. This phenomenon might be explained by above-threshold photoemission [86–90], which is the solid-state analogue to above-threshold ionization in molecules [91, 92]. To validate this hypothesis, an analysis of the kinetic energy distribution of the emitted photoelectrons would be required. Similar FRIAC experiments, using the same detection unit but at lower light intensities, have been conducted with the third harmonic of a Ti:Sa laser ($\approx$ 260 nm) (unpublished, UV source described in [93]) and with RDWs generated in a HCF setup ($\approx$ 220 nm) [94]. These measurements did not exhibit dominant higher-order detection processes, likely due to their significantly lower peak power density.

Wavelength-tunability of the UV pulses was achieved through spectral selection in the Fourier plane of the 4f geometry, as described in Chapter 3.4. While maintaining a reasonably short pulse duration of 22 fs FWHM, the central wavelength can be adjusted over a range of 10 nm, as detailed in Chapter 5.2.5.

The **VUV pulses** characterized in Chapter 6 were generated through THG in xenon and argon. Contrary to the simulations, which predicted helium as the ideal candidate due to its favorable ratio of ionization probability to third-order nonlinearity, xenon exhibited the highest conversion efficiency in the experiments. However, the available pumping speed was insufficient to achieve more than 100 mbar backing pressure for helium, resulting in suboptimal performance. As shown in Chapter 4.2, optimal conditions were predicted for 1.5 bar of helium.

Among the tested noble gases – helium, argon and xenon – all other media have led to higher VUV yield than helium, as increased backing pressures of up to 1 bar could be realized. In argon, VUV pulses of approximately 260 nJ were generated with a conversion efficiency of 4.2×10^{-4} (see Chapter 6.1.3), while xenon produced VUV pulses of approximately 1.5 µJ with a conversion efficiency of 1.7×10^{-3} (see Chapter 6.1.4). The exceptional characteristics of xenon might be attributed to a resonance line close to 130 nm [48].

The spectral analysis of the VUV radiation in Chapter 6.2.2 confirmed a central wavelength of 133 nm (9.32 eV) for the third harmonic and 80 nm (15.5 eV) for the fifth harmonic, with the fifth harmonic exhibiting significantly lower intensity. The dispersed beam profile observed on a phosphor screen in Chapter 6.2.1 displayed a well-behaved Gaussian-like shape in the vertical direction. This observation suggests that the process differs from the six-wave mixing reported by Trabs et al. [27], which is characterized by a ring shaped profile.
The concept of tuning the VUV wavelength by adjusting the fundamental of the THG was successfully demonstrated in Chapter 6.2.3, with an overall shift of 2.8 nm (0.19 eV) for the third-harmonic radiation, which is reasonably close to the expected shift of 3.3 nm (0.23 eV). However, the fifth-harmonic radiation could only be shifted by 0.5 nm (0.1 eV), which is significantly less than the expected 2 nm (0.38 eV).

A temporal analysis of the VUV pulses has not been performed in this work. Such an analysis could be conducted similarly to the characterization of the UV pulses, utilizing the FRIAC technique. However, the detection unit introduced in Chapter 5.2.1 is unsuitable for this purpose, as the photon energy of the VUV radiation exceeds the work function of any metal. Therefore, a detection scheme based on two-photon ionization of gases such as argon, krypton or xenon could be employed.

Applications

The ultrashort pulsed source at 133 nm built in this thesis is intended for use in time-resolved VUV spectroscopy of atomic and molecular systems.
One potential application is the study of VUV photodissociation dynamics of CO_2, a critical process in planetary atmospheres. CO_2 has an absorption band centered around 133 nm, characterized by pronounced vibrational structures [95].
Other interesting target systems include O_2 and H_2O, which are equally significant in atmospheric processes. The increased photon energy of 9.3 eV, compared to the 7.7 eV used in previous pump-probe studies [20–22], provides a wider single-photon ionization window for the probe and thus allows for an extended analysis of the electronic dynamics.

Among the various organic compounds available for study, polycyclic aromatic hydrocarbons (PAHs) are prominent examples. Their ionization energies typically fall within the VUV range, such as naphthalene with an ionization energy of 8.1 eV or fluorene with an ionization energy of 7.9 eV [48], which enables single-photon ionization with 9.3 eV.

Optimization

A key challenge in building and operating the experimental setup in this work was the HCF. Coupling high-power UV pulses into a hollow waveguide limits the feasible peak power and repetition rate. Additionally, the stretched fiber is quite space-consuming in the laboratory, as it is 5 m long and requires an extra safety distance for incoupling and outcoupling at both ends to prevent damages on folding mirrors. With the recent development in multipass cells [96], a more compact and stable technique for spectral broadening might be a viable option to replace the HCF.

The limiting factor in terms of tunability was the overall spectral width of the fundamental. By selecting mirrors that support a larger spectral bandwidth, the spectral width could be increased at the expense of pulse energy. However, selecting only a fraction of the spectrum reduces the pulse energy and elongates the pulses in time, leading to drastically lower conversion efficiencies to the VUV. Therefore, the generation of RDWs might offer a more promising approach for achieving wide tuning ranges while maintaining reasonable conversion efficiencies [15].

To improve the numerical simulations of THG using Luna.jl, it is essential to implement a realistic model for the refractive index in the VUV. This is particularly challenging near resonances, as the framework currently relies on Sellmeier equations. In the UV, far from resonances, Wanie et al. have demonstrated that the code is capable of producing qualitatively reliable predictions for THG in argon and neon [97].

List of acronyms

ADK	Ammosov-Delone-Krainov	49
BBO	beta barium borate	1
CEP	carrier-envelope phase	6
CPA	chirped pulse amplification	27
DFG	difference frequency generation	14
EH	hybrid electromagnetic	19
FEL	free electron laser	2
FFT	fast Fourier transform	44
FOD	fourth-order dispersion	6
FRIAC	fringe-resolved interferometric autocorrelation	5
FWHM	full width at half maximum	7
GDD	group delay dispersion	6
GNLSE	generalized nonlinear Schrödinger equation	41
GVD	group velocity dispersion	43
HCF	hollow core capillary fiber	1
HE	hybrid electromagnetic	19
IAC	intensity autocorrelation	23
IFFT	inverse fast Fourier transform	44
KBBF	potassium beryllium fluoroborate	1
KTP	potassium titanyl phosphate	13
LBO	lithium triborate	1
NIR	near-infrared	5
PAH	polycyclic aromatic hydrocarbon	97
PPT	Perelomov-Popov-Terent'ev	49
RDW	resonant dispersive wave	1
SFG	sum frequency generation	14
SHG	second-harmonic generation	5

SLM	spatial light modulator	32
SPIDER	spectral phase interferometry for direct electric-field reconstruction	28
SPM	self-phase modulation	5
TBP	time-bandwidth product	7
TE	transverse electric	19
THG	third-harmonic generation	2
Ti:Sa	titanium-sapphire	2
TM	transverse magnetic	19
TOD	third-order dispersion	6
UPPE	unidirectional pulse propagation equation	41
UV	ultraviolet	3
VUV	vacuum ultraviolet	1

Bibliography

[1] H. J. Eichler and J. Eichler. *Laser: Bauformen, Strahlführung, Anwendungen*. Vol. 8. Springer Vieweg, 2015. DOI: 10.1007/978-3-642-41438-1.

[2] T. Nakazato, I. Ito, Y. Kobayashi, X. Wang, C. Chen, and S. Watanabe. "Phase-matched frequency conversion below 150 nm in $KBe_2BO_3F_2$". In: *Optics Express* 24.15 (July 2016), p. 17149. DOI: 10.1364/oe.24.017149.

[3] H. Zhong, C. Bao, T. Lin, S. Zhou, and S. Zhou. "A newly designed femtosecond $KBe_2BO_3F_2$ device with pulse duration down to 55 fs for time- and angle-resolved photoemission spectroscopy". In: *Review of Scientific Instruments* 93.11 (Nov. 2022). DOI: 10.1063/5.0106864.

[4] D. Cyranoski. "Materials science: China's crystal cache". In: *Nature* 457.7232 (Feb. 2009), pp. 953–955. DOI: 10.1038/457953a.

[5] K. Konishi, D. Akai, Y. Mita, M. Ishida, J. Yumoto, and M. Kuwata-Gonokami. "Tunable third harmonic generation in the vacuum ultraviolet region using dielectric nanomembranes". In: *APL Photonics* 5.6 (June 2020). DOI: 10.1063/5.0008568.

[6] H. Kim, S. Han, Y. W. Kim, S. Kim, and S.-W. Kim. "Generation of coherent extreme-ultraviolet radiation from bulk sapphire crystal". In: *ACS Photonics* 4.7 (June 2017), pp. 1627–1632. DOI: 10.1021/acsphotonics.7b00350.

[7] J. Seres, E. Seres, C. Serrat, and T. Schumm. "Non-perturbative generation of DUV/VUV harmonics from crystal surfaces at 108 MHz repetition rate". In: *Optics Express* 26.17 (Aug. 2018), p. 21900. DOI: 10.1364/oe.26.021900.

[8] M. Ghotbi, M. Beutler, and F. Noack. "Generation of 25 µJ vacuum ultraviolet pulses with sub-50 fs duration by noncollinear four-wave mixing in argon". In: *Optics Letters* 35.20 (Oct. 2010), p. 3492. DOI: 10.1364/ol.35.003492.

[9] G. H. C. New and J. F. Ward. "Optical third-harmonic generation in gases". In: *Physical Review Letters* 19.10 (Sept. 1967), pp. 556–559. DOI: 10.1103/physrevlett.19.556.

[10] A. McPherson, G. Gibson, H. Jara, U. Johann, T. S. Luk, I. A. McIntyre, K. Boyer, and C. K. Rhodes. "Studies of multiphoton production of vacuum-ultraviolet radiation in the rare gases". In: *Journal of the Optical Society of America B* 4.4 (Apr. 1987), p. 595. DOI: 10.1364/josab.4.000595.

[11] M. Ferray, A. L'Huillier, X. F. Li, L. A. Lompre, G. Mainfray, and C. Manus. "Multiple-harmonic conversion of 1064 nm radiation in rare gases". In: *Journal of Physics B: Atomic, Molecular and Optical Physics* 21.3 (Feb. 1988), pp. L31–L35. DOI: 10.1088/0953-4075/21/3/001.

[12] F. Krausz. "The birth of attosecond physics and its coming of age". In: *Physica Scripta* 91.6 (May 2016), p. 063011. DOI: 10.1088/0031-8949/91/6/063011.

[13] F. Belli, A. Abdolvand, J. C. Travers, and P. S. J. Russell. "Highly efficient deep UV generation by four-wave mixing in gas-filled hollow-core photonic crystal fiber". In: *Optics Letters* 44.22 (Nov. 2019), p. 5509. DOI: 10.1364/ol.44.005509.

[14] D. E. Couch, D. D. Hickstein, D. G. Winters, S. J. Backus, M. S. Kirchner, S. R. Domingue, J. J. Ramirez, C. G. Durfee, M. M. Murnane, and H. C. Kapteyn. "Ultrafast 1 MHz vacuum-ultraviolet source via highly cascaded harmonic generation in negative-curvature hollow-core fibers". In: *Optica* 7.7 (July 2020), p. 832. DOI: 10.1364/optica.395688.

[15] J. C. Travers, T. F. Grigorova, C. Brahms, and F. Belli. "High-energy pulse self-compression and ultraviolet generation through soliton dynamics in hollow capillary fibres". In: *Nature Photonics* 13.8 (Apr. 2019), pp. 547–554. DOI: 10.1038/s41566-019-0416-4.

[16] U. Becker and D. A. Shirley, eds. *VUV and soft X-ray photoionization*. Springer US, 1996. DOI: 10.1007/978-1-4613-0315-2.

[17] P. Schmüser, M. Dohlus, J. Rossbach, and C. Behrens. *Free-electron lasers in the ultraviolet and X-ray regime: Physical principles, experimental results, technical realization*. Springer International Publishing, 2014. DOI: 10.1007/978-3-319-04081-3.

[18] A. Singer, F. Sorgenfrei, A. P. Mancuso, N. Gerasimova, O. M. Yefanov, J. Gulden, T. Gorniak, T. Senkbeil, A. Sakdinawat, Y. Liu, D. Attwood, S. Dziarzhytski, D. D. Mai, R. Treusch, E. Weckert, T. Salditt, A. Rosenhahn, W. Wurth, and I. A. Vartanyants. "Spatial and temporal coherence properties of single free-electron laser pulses". In: *Optics Express* 20.16 (July 2012), p. 17480. DOI: 10.1364/oe.20.017480.

[19] D. Rompotis, T. Gebert, M. Wieland, F. Karimi, and M. Drescher. "Efficient generation of below-threshold harmonics for high-fidelity multi-photon physics in the VUV spectral range". In: *Optics Letters* 40.8 (Apr. 2015), p. 1675. DOI: 10.1364/ol.40.001675.

[20] O. Schepp, A. Baumann, D. Rompotis, T. Gebert, A. Azima, M. Wieland, and M. Drescher. "Tracing few-femtosecond photodissociation dynamics on molecular oxygen with a single-color pump-probe scheme in the VUV". In: *Physical Review A* 94.3 (Sept. 2016). DOI: 10.1103/physreva.94.033411.

[21] A. Baumann, S. Bazzi, D. Rompotis, O. Schepp, A. Azima, M. Wieland, D. Popova-Gorelova, O. Vendrell, R. Santra, and M. Drescher. "Weak-field few-femtosecond VUV photodissociation dynamics of water isotopologues". In: *Physical Review A* 96.1 (July 2017). DOI: 10.1103/physreva.96.013428.

[22] D. Rompotis, A. Baumann, O. Schepp, T. Maltezopoulos, M. Wieland, and M. Drescher. "Single-shot nonlinear spectroscopy in the vacuum-ultraviolet". In: *Optica* 4.8 (July 2017), p. 871. DOI: 10.1364/optica.4.000871.

[23] A. Baumann, D. Rompotis, O. Schepp, M. Wieland, and M. Drescher. "Time-resolved dissociation dynamics of iodomethane resulting from Rydberg and valence excitation". In: *The Journal of Physical Chemistry A* 122.21 (May 2018), pp. 4779–4784. DOI: 10.1021/acs.jpca.8b01248.

[24] O. Schepp, A. Baumann, M. Wieland, A. Azima, and M. Drescher. "VUV-induced dynamics of the electronically excited C_2D_4 molecule in a single-color pump-probe experiment". In: *Chemical Physics Letters: X* 3 (July 2019), p. 100024. DOI: 10.1016/j.cpletx.2019.100024.

[25] C.-J. Lai, G. Cirmi, K.-H. Hong, J. Moses, S.-W. Huang, E. Granados, P. Keathley, S. Bhardwaj, and F. X. Kärtner. "Wavelength scaling of high harmonic generation close to the multiphoton ionization regime". In: *Physical Review Letters* 111.7 (Aug. 2013). DOI: 10.1103/physrevlett.111.073901.

[26] U. Sapaev, A. Husakou, and J. Herrmann. "Combined action of the bound-electron nonlinearity and the tunnel-ionization current in low-order harmonic generation in noble gases". In: *Optics Express* 21.21 (Oct. 2013), p. 25582. DOI: 10.1364/oe.21.025582.

[27] P. Trabs, H.-H. Ritze, and F. Noack. "Generation of 800 nJ 133 nm femtosecond vacuum UV pulses by third harmonic generation in argon". In: *Conference on Lasers and Electro-Optics*. CLEO QELS. OSA, 2016. DOI: 10.1364/cleo_qels.2016.fm4a.4.

[28] P. Trabs. "Erzeugung und Anwendung von Femtosekunden Lichtimpulsen im vakuum-ultravioletten Spektralbereich". PhD thesis. FU Berlin, 2015.

[29] H. Zhou, W. Li, L. Shi, D. Wang, L. Ding, and H. Zeng. "Efficient generation of vacuum and extreme ultraviolet pulses". In: *Laser Physics Letters* 11.2 (Jan. 2014), p. 025402. DOI: 10.1088/1612-2011/11/2/025402.

[30] V. Svoboda, M. D. J. Waters, D. Zindel, and H. J. Wörner. "Generation and complete polarimetry of ultrashort circularly polarized extreme-ultraviolet pulses". In: *Optics Express* 30.9 (Apr. 2022), p. 14358. DOI: 10.1364/oe.449411.

[31] J.-C. Diels and W. Rudolph. *Ultrashort laser pulse phenomena*. Elsevier, 2006. DOI: https://doi.org/10.1016/B978-0-12-215493-5.X5000-9.

[32] A. Weiner. *Ultrafast optics*. John Wiley & Sons, 2009. DOI: 10.1002/9780470473467.

[33] International Organization for Standardization. *Lasers and laser-related equipment – Test methods for laser beam widths, divergence angles and beam propagation ratios*. ISO 11146-1:2021. 2021.

[34] R. W. Boyd. *Nonlinear optics*. Academic Press, 2008. DOI: 10.1016/b978-0-12-369470-6.00020-4.

[35] B. E. A. Saleh and M. C. Teich. *Fundamentals of photonics*. John Wiley & Sons, 1991. DOI: 10.1002/0471213748.

[36] N. Bloembergen, R. K. Chang, S. S. Jha, and C. H. Lee. "Optical second-harmonic generation in reflection from media with inversion symmetry". In: *Physical Review* 174.3 (Oct. 1968), pp. 813–822. DOI: 10.1103/PhysRev.174.813.

[37] C. G. Durfee, S. Backus, H. C. Kapteyn, and M. M. Murnane. "Intense 8-fs pulse generation in the deep ultraviolet". In: *Optics Letters* 24 (1999), pp. 697–699. DOI: 10.1364/OL.24.000697.

[38] C. G. Durfee, A. R. Rundquist, S. Backus, C. Herne, M. M. Murnane, and H. C. Kapteyn. "Phase matching of high-order harmonics in hollow waveguides". In: *Physical Review Letters* (1999). DOI: 10.1103/PhysRevLett.83.2187.

[39] M. Nisoli, S. Stagira, S. D. Silvestri, O. Svelto, S. Sartania, Z. Cheng, M. Lenzner, C. Spielmann, and F. Krausz. "A novel-high energy pulse compression system: Generation of multigigawatt sub-5-fs pulses". In: *Applied Physics B: Lasers and Optics* 65.2 (Aug. 1997), pp. 189–196. DOI: 10.1007/s003400050263.

[40] E. A. J. Marcatili and R. A. Schmeltzer. "Hollow metallic and dielectric waveguides for long distance optical transmission and lasers". In: *Bell System Technical Journal* 43.4 (July 1964), pp. 1783–1809. DOI: 10.1002/j.1538-7305.1964.tb04108.x.

[41] R. L. Abrams. "Coupling losses in hollow waveguide laser resonators". In: *IEEE Journal of Quantum Electronics* 8.11 (1972). DOI: 10.1109/JQE.1972.1076875.

[42] T. Nagy, M. Forster, and P. Simon. "Flexible hollow fiber for pulse compressors". In: *Applied Optics* 47.18 (June 2008), p. 3264. DOI: 10.1364/ao.47.003264.

[43] F. Böhle, M. Kretschmar, A. Jullien, M. Kovacs, M. Miranda, R. Romero, H. Crespo, U. Morgner, P. Simon, R. Lopez-Martens, and T. Nagy. "Compression of CEP-stable multi-mJ laser pulses down to 4 fs in long hollow fibers". In: *Laser Physics Letters* 11.9 (June 2014), p. 095401. DOI: 10.1088/1612-2011/11/9/095401.

[44] A. Monmayrant, S. Weber, and B. Chatel. "A newcomer's guide to ultrashort pulse shaping and characterization". In: *Journal of Physics B* 43.10 (May 2010), p. 103001. DOI: 10.1088/0953-4075/43/10/103001.

[45] K. Naganuma, K. Mogi, and H. Yamada. "General method for ultrashort light pulse chirp measurement". In: *IEEE Journal of Quantum Electronics* 25.6 (June 1989), pp. 1225–1233. DOI: 10.1109/3.29252.

[46] T. Gebert, D. Rompotis, M. Wieland, F. Karimi, A. Azima, and M. Drescher. "Michelson-type all-reflective interferometric autocorrelation in the VUV regime". In: *New Journal of Physics* 16.7 (July 2014), p. 073047. DOI: 10.1088/1367-2630/16/7/073047.

[47] C. Iaconis and I. A. Walmsley. "Spectral phase interferometry for direct electric-field reconstruction of ultrashort optical pulses". In: *Optics Letters* 23.10 (May 1998), p. 792. DOI: 10.1364/ol.23.000792.

[48] A. Kramida and Y. Ralchenko. *NIST atomic spectra database, NIST standard reference database 78*. 1999. DOI: 10.18434/T4W30F. URL: https://physics.nist.gov/asd.

[49] A. M. Weiner, J. P. Heritage, and E. M. Kirschner. "High-resolution femtosecond pulse shaping". In: *J. Opt. Soc. Am. B* 5.8 (1988). DOI: 10.1364/JOSAB.5.001563.

[50] N. Dimitrov, P. Lazarova, L. Stoyanov, I. Stefanov, and A. Dreischuh. "Dispersion control in a folded 4-f system for shaping femtosecond laser pulses". In: *Proceedings of SPIE* (Jan. 2017). DOI: 10.1117/12.2264705.

[51] M. E. Durst, D. Kobat, and C. Xu. "Tunable dispersion compensation by a rotating cylindrical lens". In: *Optics Letters* 34.8 (Apr. 2009), p. 1195. DOI: 10.1364/OL.34.001195.

[52] M. G. Moharam and T. K. Gaylord. "Diffraction analysis of dielectric surface-relief gratings". In: *Journal of the Optical Society of America* 72.10 (Oct. 1982), p. 1385. DOI: 10.1364/JOSA.72.001385.

[53] T. Gebert. "Messung ultrakurzer molekularer Zeitkonstanten mit nichtlinearer interferometrischer Autokorrelation bei 160 nm Wellenlänge". PhD thesis. Universität Hamburg, 2014.

[54] D. Rompotis. "A single-shot nonlinear autocorrelation approach for time-resolved physics in the vacuum ultraviolet spectral range". PhD thesis. Universität Hamburg, 2015.

[55] O. Schepp. "Untersuchungen zur Reaktionsdynamik kleiner Moleküle mittels interferometrischer VUV-VUV Anrege-Abfrage Spektroskopie". PhD thesis. Universität Hamburg, 2018.

[56] A. Baumann. "Time-resolved ultrafast photoreaction dynamics of small molecules in the vacuum ultraviolet spectral range". PhD thesis. Universität Hamburg, 2018.

[57] C. Brahms and J. C. Travers. *Luna.jl*. 2023. DOI: 10.5281/ZENODO.5513570. URL: https://github.com/LupoLab/Luna.jl.

[58] G. P. Agrawal. *Nonlinear fiber optics*. AT&T Bell Laboratories, 2013. DOI: 10.1016/b978-0-12-397023-7.00021-8.

[59] B. C. Hall. *Lie groups, Lie algebras, and representations: An elementary introduction*. Springer Science & Business Media, 2003. DOI: 10.1007/978-3-319-13467-3.

[60] A. Suda, M. Hatayama, K. Nagasaka, and K. Midorikawa. "Generation of sub-10-fs, 5-mJ-optical pulses using a hollow fiber with a pressure gradient". In: *Applied Physics Letters* 86.11 (Mar. 2005), p. 111116. DOI: 10.1063/1.1883706.

[61] C. Cuthbertson and M. Cuthbertson. "The refraction and dispersion of neon and helium". In: *Proceedings of the Royal Society of London* 135.826 (Feb. 1932), pp. 40–47. DOI: 10.1098/rspa.1932.0019.

[62] C. Bree, A. Demircan, and G. Steinmeyer. "Method for computing the nonlinear refractive index via Keldysh theory". In: *IEEE Journal of Quantum Electronics* 46.4 (Apr. 2010), pp. 433–437. DOI: 10.1109/jqe.2009.2031599.

[63] J. Schroeder. "Signal processing via Fourier-Bessel series expansion". In: *Digital Signal Processing* 3.2 (Apr. 1993), pp. 112–124. DOI: 10.1006/dspr.1993.1016.

[64] A. M. Perelomov, V. S. Popov, and M. V. Terent'ev. "Ionization of atoms in an alternating electric field". In: *Soviet Physics JETP* 23.5 (1966), p. 924.

[65] A. M. Perelomov, V. S. Popov, and M. V. Terent'ev. "Ionization of atoms in an alternating electric field: II". In: *Soviet Physics JETP* 24.1 (1967), p. 207.

[66] A. M. Perelemov and V. S. Popov. "Ionization of atoms in an alternating electric field: III". In: *Soviet Physics JETP* 25.336 (1967).

[67] L. V. Keldysh. "Ionization in the field of a strong electromagnetic wave". In: *Soviet Physics JETP* 20.5 (Nov. 1965), p. 1307.

[68] M. V. Ammosov, N. B. Delone, and V. P. Krainov. "Tunnel ionization of complex atoms and of atomic ions in an alternating electromagnetic field". In: *Soviet Physics JETP* 64.6 (1986), p. 1191.

[69] S. F. J. Larochelle, A. Talebpour, and S. L. Chin. "Coulomb effect in multiphoton ionization of rare-gas atoms". In: *Journal of Physics B: Atomic, Molecular and Optical Physics* 31.6 (Mar. 1998), pp. 1215–1224. DOI: 10.1088/0953-4075/31/6/009.

[70] S. V. Popruzhenko, V. D. Mur, V. S. Popov, and D. Bauer. "Strong field ionization rate for arbitrary laser frequencies". In: *Physical Review Letters* 101.19 (Nov. 2008). DOI: 10.1103/physrevlett.101.193003.

[71] D. R. Hartree. "The wave mechanics of an atom with a non-coulomb central field. Part I: Theory and methods". In: *Mathematical Proceedings of the Cambridge Philosophical Society* 24.1 (Jan. 1928), pp. 89–110. DOI: 10.1017/s0305004100011919.

[72] H. G. Dawson. "On the numerical value of $\int_0^h ex^2dx$". In: *Proceedings of the London Mathematical Society* s1-29.1 (Nov. 1897), pp. 519–522. DOI: 10.1112/plms/s1-29.1.519.

[73] M. Geissler, G. Tempea, A. Scrinzi, M. Schnürer, F. Krausz, and T. Brabec. "Light propagation in field-ionizing media: Extreme nonlinear optics". In: *Physical Review Letters* 83.15 (Oct. 1999), pp. 2930–2933. DOI: 10.1103/physrevlett.83.2930.

[74] M. F. Saleh and F. Biancalana. *Shaping light in nonlinear optical fibers - Novel nonlinear optical phenomena in gas-filled hollow-core photonic crystal fibers.* Ed. by S. Boscolo and C. Finot. JohnWiley & Sons Ltd, 2017. Chap. 3, pp. 65–89.

[75] M. Kolesik, J. V. Moloney, and M. Mlejnek. "Unidirectional optical pulse propagation equation". In: *Physical Review Letters* 89.28 (Dec. 2002). DOI: 10.1103/physrevlett.89.283902.

[76] M. Kolesik and J. V. Moloney. "Nonlinear optical pulse propagation simulation: From Maxwell's to unidirectional equations". In: *Physical Review E* 70.3 (Sept. 2004). DOI: 10.1103/physreve.70.036604.

[77] A. Börzsönyi, Z. Heiner, M. P. Kalashnikov, A. P. Kovács, and K. Osvay. "Dispersion measurement of inert gases and gas mixtures at 800 nm". In: *Applied Optics* 47.27 (Sept. 2008), p. 4856. DOI: 10.1364/ao.47.004856.

[78] A. Ermolov, K. F. Mak, M. H. Frosz, J. C. Travers, and P. S. J. Russell. "Supercontinuum generation in the vacuum ultraviolet through dispersive-wave and soliton-plasma interaction in a noble-gas-filled hollow-core photonic crystal fiber". In: *Physical Review A* 92.3 (Sept. 2015). DOI: 10.1103/physreva.92.033821.

[79] A. Laubereau. *Ultrashort laser pulses: Generation and applications - Optical nonlinearities with ultrashort pulses*. Ed. by W. Kaiser. Springer Berlin Heidelberg, 1993. Chap. 3, pp. 35–112. DOI: 10.1007/BFb0070977.

[80] R. C. Miller. "Second harmonic generation with a broadband optical maser". In: *Physics Letters A* 26.5 (Jan. 1968), pp. 177–178. DOI: 10.1016/0375-9601(68)90104-7.

[81] D. Eimerl, L. Davis, S. Velsko, E. K. Graham, and A. Zalkin. "Optical, mechanical, and thermal properties of barium borate". In: *Journal of Applied Physics* 62.5 (Sept. 1987), pp. 1968–1983. DOI: 10.1063/1.339536.

[82] W. Haynes, ed. *CRC handbook of chemistry and physics*. CRC Press, Taylor & Francis Group, LLC, June 2014. DOI: 10.1201/b17118.

[83] I. H. Malitson. "Interspecimen comparison of the refractive index of fused silica". In: *Journal of the Optical Society of America* 55.10 (Oct. 1965), p. 1205. DOI: 10.1364/josa.55.001205.

[84] S. Fujisawa, K. Ohno, S. Masuda, and Y. Harada. "Penning ionization electron spectroscopy of monohalobenzenes: Fluorobenzene, chlorobenzene, bromobenzene, and iodobenzene". In: *Journal of the American Chemical Society* 108.21 (Oct. 1986), pp. 6505–6511. DOI: 10.1021/ja00281a010.

[85] M. H. Palmer, T. Ridley, S. V. Hoffmann, N. C. Jones, M. Coreno, M. de Simone, C. Grazioli, M. Biczysko, A. Baiardi, and P. Limão-Vieira. "Interpretation of the vacuum ultraviolet photoabsorption spectrum of iodobenzene by ab initio computations". In: *The Journal of Chemical Physics* 142.13 (Apr. 2015). DOI: 10.1063/1.4916121.

[86] S. Luan, R. Hippler, H. Schwier, and H. O. Lutz. "Electron emission from polycrystalline copper surfaces by multi-photon absorption". In: *Europhysics Letters (EPL)* 9.5 (July 1989), pp. 489–494. DOI: 10.1209/0295-5075/9/5/014.

[87] W. S. Fann, R. Storz, and J. Bokor. "Observation of above-threshold multiphoton photoelectric emission from image-potential surface states". In: *Physical Review B* 44.19 (Nov. 1991), pp. 10980–10982. DOI: 10.1103/physrevb.44.10980.

[88] G. Farkas, C. Toth, and A. Kohazi-Kis. "Above-threshold multiphoton photoelectric effect of a gold surface". In: *Optical Engineering* 32.10 (1993), p. 2476. DOI: 10.1117/12.145288.

[89] M. Aeschlimann, C. A. Schmuttenmaer, H. E. Elsayed-Ali, R. J. D. Miller, J. Cao, Y. Gao, and D. A. Mantell. "Observation of surface enhanced multiphoton photoemission from metal surfaces in the short pulse limit". In: *The Journal of Chemical Physics* 102.21 (June 1995), pp. 8606–8613. DOI: 10.1063/1.468962.

[90] M. Schenk, M. Krüger, and P. Hommelhoff. "Strong-field above-threshold photoemission from sharp metal tips". In: *Physical Review Letters* 105.25 (Dec. 2010). DOI: 10.1103/physrevlett.105.257601.

[91] P. Agostini, F. Fabre, G. Mainfray, G. Petite, and N. K. Rahman. "Free-free transitions following six-photon ionization of xenon atoms". In: *Physical Review Letters* 42.17 (Apr. 1979), pp. 1127–1130. DOI: 10.1103/physrevlett.42.1127.

[92] J. H. Eberly, J. Javanainen, and K. Rzazewski. "Above-threshold ionization". In: *Physics Reports* 204.5 (June 1991), pp. 331–383. DOI: 10.1016/0370-1573(91)90131-5.

[93] M. Galli, V. Wanie, D. P. Lopes, E. P. Månsson, A. Trabattoni, L. Colaizzi, K. Saraswathula, A. Cartella, F. Frassetto, L. Poletto, F. Légaré, S. Stagira, M. Nisoli, R. Martínez Vázquez, R. Osellame, and F. Calegari. "Generation of deep ultraviolet sub-2-fs pulses". In: *Optics Letters* 44.6 (Mar. 2019), p. 1308. DOI: 10.1364/ol.44.001308.

[94] H. A. Rashtabadi. "Tailored generation, modulation, and characterization of deep- and vacuum-ultraviolet ultrashort pulses". PhD thesis. Universität Hamburg, 2024.

[95] E. C. Y. Inn, K. Watanabe, and M. Zelikoff. "Absorption coefficients of gases in the vacuum ultraviolet. Part III. CO_2". In: *The Journal of Chemical Physics* 21.10 (Oct. 1953), pp. 1648–1650. DOI: 10.1063/1.1698637.

[96] A.-L. Viotti, M. Seidel, E. Escoto, S. Rajhans, W. P. Leemans, I. Hartl, and C. M. Heyl. "Multi-pass cells for post-compression of ultrashort laser pulses". In: *Optica* 9.2 (Feb. 2022), p. 197. DOI: 10.1364/optica.449225.

[97] V. Wanie, P. Barbato, J. Hahne, S. Ryabchuk, A. B. Wahid, D. Amorim, E. P. Månsson, A. Trabattoni, R. Osellame, R. Martínez Vázquez, and F. Calegari. "Ultraviolet supercontinuum generation using a differentially-pumped integrated glass chip". In: *Journal of Physics: Photonics* 6.2 (Mar. 2024), p. 025005. DOI: 10.1088/2515-7647/ad2bd3.

A. Appendix

A.1. MATLAB code for solving the GNLSE

Since the 2D version of the split-step Fourier MATLAB code is distributed over various files, and even the much simpler 1D version exeeds the scope of this appendix, only the key parts of the 1D code are presented here to illustrate the implementation. The theory behind the method is described in Chapter 4.1.1.

First, input parameters are given:

```
%% define parameters

red = false;              % red is 800 nm
blue = true;              % blue is 400 nm

selfsteep = true;
loss = true;

steps =2000;              % steps in propagation direction
L = 5;                    % fiber length

T_0 =30*10^-15;           % (temp.) Pulse length [s] FWHM
Energy =1*10^-3;          % pulse Energy [J]

p_end = 1.5;              % press in bar at fiber output
p_in =0;                  % press in bar at fiber output

a =250*10^-6;             % fiber core radius [m]


GDD = 0*(10^-15)^2;       %GDD [s^2]
TOD =0*(10^-15)^3;        %TOD [s^3]
FOD = 0*(10^-15)^4;       %FOD [s^4]
```

Waveguide dispersion, loss coefficient, nonlinear coefficient and pressure gradient are calculated from those input parameters. Subsequently, the numeric grid and the input field for the propagation are defined:

```
%% numeric grid

dL =L/steps;          % step
N=2^12;               % #steps
dt=T_0*30/N;          % timestep
t=(-N/2:N/2-1)*dt;    % time grid

df=1/(dt*N);          % freq step
f=(-N/2:N/2-1)*df;    % freq grid

```

```
156
157 AA=zeros(1,N);       %Coeff for FFT, iFFT
158 for jj=1:N
159     AA(jj)=(-1).^(jj-1);
160 end
161
162 %% input field fourier-limit
163
164 A1 = sqrt(P_0)*exp(-1/2*(2*sqrt(log(2))*t/T_0).^2);  %Gaussian field
```

Thereafter, the operator D is calculated for each propagation step:

```
223 %% define dispersion
224
225 D=zeros(steps,N);
226 for x=1:steps
227
228 D(x,:)=exp(dL/2*(-0.5*alpha(x)+(0.5*1i*beta_2(x)*(2*pi*f).^2)+(1i*beta_3(x)/6*(2*pi
        *f).^3)+(1i*beta_4(x)/factorial(4)*(2*pi*f).^4)+(1i*beta_5(x)/factorial(5)*(2*
        pi*f).^5)+(1i*beta_6(x)/factorial(6)*(2*pi*f).^6)));
229 end
```

Finally, the propagation starts:

```
238 %% propagation
239 for xx=1:steps
240 disp(strcat('step ',num2str(xx),' of  ',num2str(steps))) %count steps
241 time(xx)=toc;
242
243 %% 1/2 disp step
244 F=AA.*fftshift(ifft(A));
245 A=AA.*fftshift(fft((F.*(D(xx,:)))));
246
247 %% NL step
248 derivative_abs=deriv1(abs(A).^2,dt);
249 derivative_a=deriv1(A,dt);
250     if selfsteep ==true
251         NL(xx,:) = exp(dL*1i*gamma(xx)*(abs(A)).^2-(0.5*2*gamma(xx)./omega_0*dL).*(
              derivative_abs+conj(A).*derivative_a)); % with self-steep
252     else
253         NL(xx,:) = exp(dL*1i*gamma(xx)*(abs(A)).^2); % without self-steep
254     end
255 A=NL(xx,:).*A;
256
257 %% 1/2 disp step
258 F=AA.*fftshift(ifft(A));
259 A=AA.*fftshift(fft((F.*(D(xx,:)))));
260
261 %% save
262 H=AA.*fftshift(ifft(A))*dt*N;
263 Spec(xx+1,:)=abs(H).^2;
264 I(xx+1,:)=abs(A).^2;
265 Spec_l(xx+1,:)=abs(H).^2*2*pi*c./lambda.^2;
266
267 end
268
269 Energy_test_output=sum(abs(A).^2)*dt; %should be Energy
270 Eout = A;
271 Fout = AA.*fftshift(ifft(Eout))*dt*N;
272 f1 = f + omega_0/(2*pi);
273 lambda=10^9*c./f1; % [nm]
```

Eout and Fout are the output fields in time and frequency space. I and Spec contain information about the evolution of the fields along the propagation.

Thereafter, various different plots are generated, showing the temporal and spectral distribution as well as the phase of the pulse, as shown in Figures A.1 and A.2.

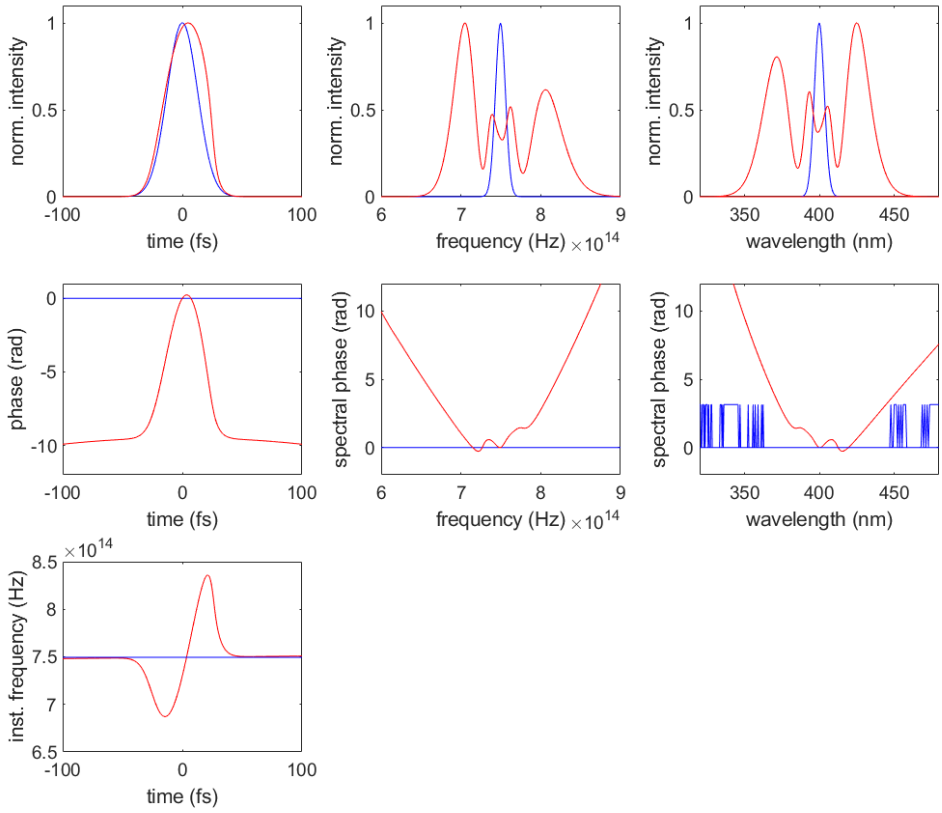

Figure A.1.: Temporal and spectral distribution of the input pulse (blue) and the output pulse (red) together with the phase characteristics.

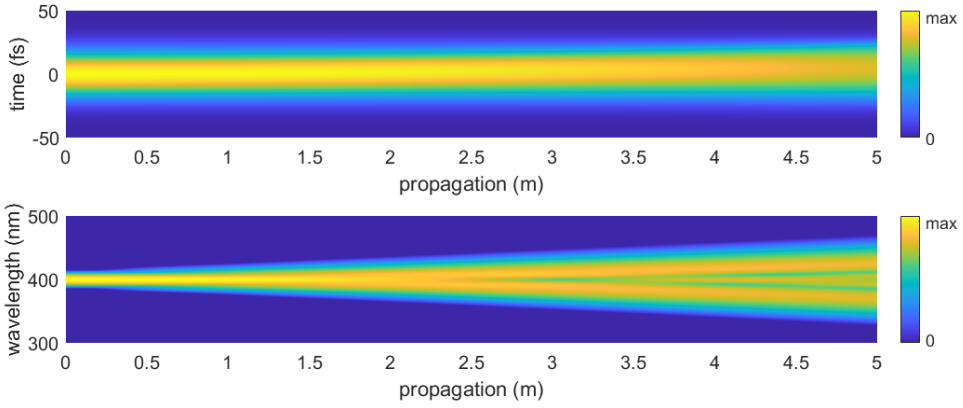

Figure A.2.: Temporal and spectral evolution along the propagation.

A.2. Julia code for THG using Luna.jl

In the following, the the key parts of the code utilizing Luna.jl [57] to simulate THG are presented. Details about the approach can be found in Chapter 4.2.

First, the input parameters are defined:

```
using Luna
import Luna.PhysData: wlfreq
import FFTW
import Luna: Hankel
import NumericalIntegration: integrate, SimpsonEven

gas = :HeJ      # options are: HeJ, Ne, Xe, Ar, Kr...
pres = 1.5      # maximum pressure in bar
low = 0         # minimum pressure in bar
τ = 10e-15      # input pulse FWHM in seconds
λ0 = 400*1e-9   # input wavelegth in meter
w0 = 70e-6      # gaussian beam waist at focus in meter
energy = 0.5e-3 # input pulse energy
L = 0.01        # length of the gas cell in meter
Z=(0, L/2, L)   # defining points for presure gradient
P=(0,pres,0)    # values for pressure gradient
R = 1e-3        # radius of the considered volume in meter
N = 1024        # number of points in radial direction
(coren,dens)=Capillary.gradient(gas,Z,P);
```

Then, the grid is defined. Subsequently, the linear and nonlinear response terms and the input field are calculated:

```
ionpot = PhysData.ionisation_potential(gas)
ionrate = Ionisation.ionrate_fun!_PPTcached(gas, λ0)
responses = (Nonlinear.Kerr_field(PhysData.γ3_gas(gas)),Nonlinear.PlasmaCumtrapz
    (grid.to, grid.to, ionrate, ionpot))
linop = LinearOps.make_linop(grid, q, coren)
normfun = NonlinearRHS.norm_radial(grid, q, coren)
inputs = Fields.GaussGaussField(λ0=λ0, τfwhm=τ, energy=energy, w0=w0, propz=-L/2
    )
```

Starting the propagation is now straightforward:

```
Luna.run(Eω, grid, linop, transform, FT, output, max_dz=1e-3, init_dz=1e-4)
ω = grid.ω
t = grid.t
zout = output.data["z"]
Eout = output.data["Eω"]
```

The stepsize is automatically adjusted. Only an initial value, init_dz, and a maximum value, max_dz, are given. To extract the VUV part of the output field, a filter in Fourier space is applied.

A.3. Mathematica noteboook for dispersion in the 4f setup

In Chaper 4.3, the simulation of the spectral phase using the optical design package *Optica EM* is described. As mentioned before, the code was originally developed by Armin Azima. Only minor adjustments are made to implement the retro-reflector and adjust the dimensions and angles accordingly. In the following, parts of the *Wolfram Mathematica* notebook containing the calculations are presented.

First, the wavelength range, the light source, the transmission grating, and the cylindrical lens are defined:

```
In[705]:=
λmin = 0.370;
λ0 = 0.400;
λmax = 0.430;

In[708]:= nrOfRays = 20;

In[709]:= SourceOfLight = RainbowOfRays[{λmin, λmax}, NumberOfRays → nrOfRays];

In[710]:= TransmissionGrating =
  Grating[1400, {50, 20}, 6, {DiffractedOrders → {{0, 0}, {0, 0}, {1, 1}},
    ComponentMedium → QuartzE, GratingMedium → QuartzE, VacuumFrequency → False}];

In[711]:= CylindricalLensQuartz = PlanoConvexCylindricalLens[
   {f, 300}, {{a, 50.8}, {b, 50.8}}, {t, 5}, ComponentMedium → QuartzE];
```

Then, the system is virtually assembled and analyzed:

```
In[718]:= Gratingandlens =
            {Move[Rotate[Rotate[SourceOfLight, -33.85, {0, 0, 1}], -3, {0, 1, 0}], {0, 60, -4}],
             Resonate[{Move[Rotate[Rotate[TransmissionGrating, 0, {0, 1, 0}], -0, {0, 0, 1}],
                offset], Move[Rotate[CylindricalLensQuartz, -1], (xlens + offset)],
               Move[Rotate[Mirror[50.8, 6, ComponentMedium → QuartzE], -46.3, {0, 1, 0}],
                {(xmirr + xlens + offset), 0, 20}],
               Move[Rotate[Mirror[50.8, 6, ComponentMedium → QuartzE], 46.3, {0, 1, 0}],
                {(xmirr + xlens + offset), 0, -20}]}],
             (*Move[Screen[100],{400,0,0}],*) Move[Screen[200], {0, 0, 0}]};
          AnalyzeSystem[Gratingandlens, PlotType → Surface, ColorView1
           → RaySourceNumber];
```

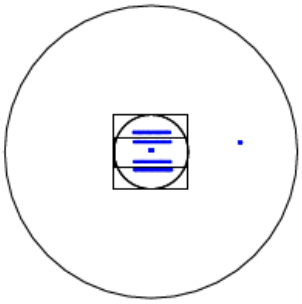

```
In[720]:= screensys = AnalyzeSystem[Gratingandlens, PlotType → RealTime3D];
```

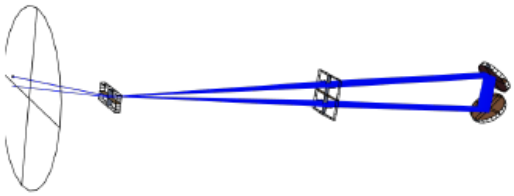

From the path differences, the phase is calculated:

```
In[731]:= ϕi = Interpolation[λiϕi[λmin, λmax, nrOfRays], InterpolationOrder → 9];

In[732]:= ϕi[λmax]
Out[732]= -1239.23

In[733]:= Plot[N[ϕi[λ] / (2 * π)], {λ, λmin, λmax}, AxesLabel → {"λ [μm]", "ϕ [2π]"}]
```

Out[733]=

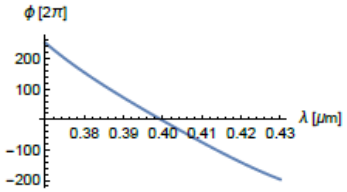

From this phase, the derivatives are extracted and the group delay, GDD and TOD are calculated, as shown in Figure 4.17.

Acknowledgments

Completing this PhD thesis has been a long journey marked by many failures, damaged components, and laser issues. Thus, I am thankful that I could always rely on the DynamiX group for their support, advice, and encouragement.

First, I would like to express my gratitude to Prof. Markus Drescher for the opportunity to work on this project, for his valuable advice, and for coming up with creative solutions to any problem - usually involving glue and/or homemade electronic devices.
I owe special thanks to Marek Wieland for his support in the lab, for sharing his expertise in countless discussions, for reading this thesis, and for his motivating postdoc optimism.
In addition, I would like to thank Mark Prandolini for many helpful discussions regarding my project, the simulations, and ultrafast optics in general, as well as for reading this thesis.
I would like to thank Oliver Becker for technical support, for designing the vacuum chamber and many other components of the experiment, and for always providing replacement parts when needed - sometimes even on the same day.
Further thanks go to Hannes Bein for great teamwork with the laser system and for emotional support during times of frustration in the lab.
Moreover, I would like to thank Mohamed Abdelrasoul, Mehrdad Kheyrollahi, Hamid Rashtabadi, Morteza Asghari, and everyone else who is or was part of the DynamiX group during my work for creating such a supportive and pleasant atmosphere.

Finally, I want to thank Armin Azima for the unfortunately limited time we worked together on this project and for his major contributions to the design of the experiment.